DEVELOPMENT OF POLYMERIC SYSTEMS FOR CABAZITAXEL RELEASE

KABAZİTAKSEL SALINIMI İÇİN POLİMERİK SİSTEMLERİN GELİŞTİRİLMESİ

NADA OMAR ABDULKAREEM ABDULKAREEM

PROF. DR ADİL DENİZLİ
Supervisor

Submitted to
Graduate School of Science and Engineering
of Hacettepe University
as a Partial Fulfillment of the Requirements for the Degree of
Master of Science
in Chemistry

2022

ABSTRACT

DEVELOPMENT OF POLYMERIC SYSTEMS FOR CABAZİTAXEL RELEASE

NADA OMAR ABDULKAREEM ABDULKAREEM

Master of Science, Department of Chemistry

Supervisor: Prof. Dr. Adil DENİZLİ

September 2022, 82 Pages

Cabazitaxel (CTZ) is a chemotherapy drug used to treat mCRPC patients. Bacterial cellulose (BC) has been combined with molecularly imprinted polymer (MIP) for anticancer drug delivery with controlled release. On surface-modified bacterial cellulose nanofibers, composite molecularly imprinted nanofibers were prepared by in-situ graft polymerization of methacrylic acid as the monomer, N, N'-Methylenebisacrylamide as the crosslinker, and Cabazitaxel as the template molecule. Cabazitaxel-imprinted polymers were fabricated onto bacterial cellulose nanofibers, resulting in the formation of composite BC nanofibers. Consequently, the composite nanofibers incorporated with cabazitaxel imprinted polymers were attained and fabricated. The in-vitro drug release tests were conducted to evaluate the release performance of the resultant composite nanofibers at varying temperatures of 25, 37, and 40 °C, concentrations of 0.5, 1, 2, 3, and 4 mg/mL, and different pH values (5.5, 6, 7, 7.4, and 8). The application of MIP-BC in medicine and pharmaceutics may be of great interest due to the simplicity of preparing the drug delivery system without synthetic MIP.

Keywords: Cabazitaxel, bacterial cellulose nanofibers, drug delivery system, drug release, molecular imprinting.

ÖZET

KABAZİTAKSEL SALINIMI İÇİN POLİMERİK SİSTEMLERİN GELİŞTİRİLMESİ

NADA OMAR ABDULKAREEM ABDULKAREEM

Yüksek Lisans, KİMYA BÖLÜMÜ

Tez Danışmanı: Prof. Dr. Adil DENİZLİ

Eylül 2022, 82 sayfa

Kabazitaksel (CTX), mCRPC hastalarını tedavi etmek için kullanılan bir kemoterapi ilacıdır. Bu tez çalışmasında, kontrollü salım ile antikanser ilaç dağıtımı için moleküler baskılanmış polimerler (MIP) temelli bakteriyel selüloz (BC) biyopolimerler hazırlanmıştır. Yüzeyi modifiye edilmiş bakteriyel selüloz nanoliflerinde, monomer olarak metakrilik asit, çapraz bağlayıcı olarak N, N'-Metilenbisakrilamid ve kalıp molekül olarak Kabazitaksel kullanılarak yığın polimerizasyonu ile kompozit moleküler baskılanmış nanolifler hazırlanmıştır. Kabazitaksel baskılanmış polimer kaplı kompozit BC nanoliflerinin oluşumuyla sonuçlanmıştır. Sonuç olarak, kabazitaksel baskılanmış polimer birleştirilmiş kompozit nanolifler elde edildi ve üretildi. Elde edilen kompozit nanoliflerin 25, 37 ve 40 °C değişen sıcaklıklarda, 0.5, 1, 2, 3 ve 4 mg/mL derişimlerde ve farklı pH değerlerinde salım performansını değerlendirmek için in vitro ilaç salım testleri gerçekleştirilmiştir. (5.5, 6, 7, 7.4 ve 8). MIP-BC'nin tıpta ve eczacılıkta uygulanması, sentetik MIP kullanılmadan ilaç taşıma sisteminin hazırlanmasının basitliği nedeniyle büyük ilgi çekebilir.

Anahtar Kelimeler: Kabazitaksel, bakteriyel selüloz nanolifleri, ilaç taşıyıcı sistem, ilaç salımı, moleküler baskılama.

ACKNOWLEDGMENTS

In the name of Allah, the most gracious and the most merciful. First and foremost, I am thankful to Almighty ALLAH for giving me the strength, knowledge, ability, and opportunity to undertake this study and complete it satisfactorily.

I would like to thank the following people, without whom I would not have been able to complete this thesis and without whom I would not have made it through my master’s degree!

Especially to my supervisor, Prof. Dr. Adil Denizli., Department of Chemistry, University of Hacettepe, whose insight and knowledge of the subject matter steered me through this thesis; more than a supervisor, he helped me a lot with his constant support. “Thank you for everything.”

Besides my supervisor, I would like to thank the rest of my thesis committee: Prof. Dr. Handan Yavuz Alagöz, Prof. Dr. Nilay Bereli, Assoc. Prof. Dr. Deniz Türkmen, and Assoc. Prof. Dr. Fatma Yılmaz for their time to review my thesis, insightful comments, and unlimited guidance.

I could not have undertaken this journey without Lect. Ph.D. Semra Akgönüllü for her treasured support, which was influential in shaping my experiment methods, Patience, guidance, and expertise that she shared with me, “thank you from deep of my heart.”

I am also thankful to Assoc. Prof. Deniz Türkmen, Department of Chemistry, University of Hacettepe, for all his help and advice with this thesis.

I need to express my deep gratitude to Prof. Dr. Abdulmajeed Alsamarrai. Department of Applied Chemistry, University of Samarra, for his support whenever I needed it.

And my biggest thanks to my family for all the support you have shown me through this journey, especially to my sister samara for all the entertainment and emotional support.

CONTENTS

FIGURE LEGENDS

TABLE LEGENDS

SYMBOLS AND ABBREVIATIONS

Symbols

^{1}H	Proton
λ	Wavelength
K_2HPO_4	Dipotassium Hydrogen Phosphate
KH_2PO_4	Potassium Dihydrogen Phosphate

Abbreviations

CTX	Cabazitaxel
Tween-80	Polysorbate 80
BC	Bacterial Cellulose
H-S	Hestrin–Schramm
MIP	Molecularly Imprinted Polymer
NIP	Non-Imprinted Polymer
DMAP	4-dimethyl aminopyridine (DMAP)
CH_2Cl_2	Dichloromethane
$CDCl_3$	Chloroform-d
3-MPS	3-(Methacryloyloxy) propyl] trimethoxysilane
MBAAm	N, N-methylenebis acrylamide
MAA	Methacrylic acid
AIBN	2,2′-Azobis(2-methylpropionitrile)
PBS	Phosphate Buffered Saline
UV	Ultraviolet
FTIR	Fourier Transform Infrared
HNMR	Proton Nuclear Magnetic Resonance
FIB-SEM	Focused Ion Beam Scanning Electron Microscope
DLS	Dynamic Light Scattering
PDI	Polydispersity Index
TGA	Thermogravimetric Analysis

1. INTRODUCTION

Prostate cancer (PC) is the most frequent type of recently diagnosed malignancy in men worldwide; it is also one of the most frequent among all the leading cancer-related death causes [1–3]. Even though androgen deprivation therapy is effective in treating localized tumors in most patients, one-third of patients experience the development of metastatic castration-resistant adenocarcinoma (mCRPC), which may be a molecularly heterogeneous condition [4]. Cabazitaxel is recommended for patients with rapidly progressing disease, inadequate response to initial androgen deprivation therapy (ADT), or the presence of visceral metastases [5].

Cabazitaxel (CTX) is a chemotherapy drug used to treat mCRPC patients [6,7]. CTX, the first drug to show an overall survival advantage in mCRPC after docetaxel (DTX) [8], is a microtubule-stabilizing agent that promotes the polymerization of βIII-tubulin. This interferes with mitosis and causes apoptosis. In vivo, CTX outperforms docetaxel in anticancer efficacy and antiproliferative activity against chemotherapy-resistant tumor cell lines [9]. Similar to other taxanes (DTX and paclitaxel (PTX)), CTX is a lipophilic, water-insoluble, chemically unstable drug [10,11] because of its bulky polycyclic structure, which has limited its usefulness as a therapeutic agent. Jevtana®, the commercially available formulation of CTX, was developed by Sanofi-Aventis [12]. For the metastatic castration-resistant prostate cancer medication in the patients formerly treated with a regimcastratien containing DTX [13]. It is the fourth taxane licensed for use in cancer treatment. Since CTX is water-insoluble, the liquid surfactant polysorbate 80 (Tween-80) is used in its clinical formulation (Jevtana®) and ethanol as solvents due to the use of Tween-80 as an enhancer of solubility [14], which unfortunately may cause neutropenia, neurotoxicity, hypersensitivity reactions, gastrointestinal disturbances, and renal failure, and other severe side effects [15]. Consequently, it is imperative to use innovative strategies to enhance its therapeutic efficacy moreover, its target and minimize its side effects [16].

Even though CTX has significant anticancer therapeutic potential; however, its high toxicity and limited solubility in water limit its applications. On the other hand, the utilization of prodrugs is a promising method for overcoming these constraints [17]. Through treatment with succinic anhydride, the further reactive 2′-(OH) group of CTX was first effectively converted to a (COOH) group [18]. Tao Liu et al. synthesized two mightily water-solvable, acid-sensitive PEGylated acyclic-ketal-linked CTX prodrugs (PKCs) with increased anticancer activity. PKCs were quickly analyzed in an acidic tumor microhabitat, which allowed the native drug to be released [17].

Additionally, Nano-drug delivery systems (NDDSs) as a nano-carrier system (NCS) can lengthen the half-life of anticancer drugs in vivo, improve tumor targeting, and reduce toxicity. NDDSs use biodegradable and synthetic polymers. This reduces the system's initial burst effect and drug degradation rate, the sustained release of the drug. Natural biodegradable polymers (biopolymers) nano-carriers are the most popular choice because of their biodegradability, biocompatibility, and low toxicity. One of the natural biodegradable nano-carrier is polysaccharides [19]. CellaxTM is an innovative drug delivery system based on nanoparticle polymer created to solubilize hydrophobic drugs and target them to solid tumors. Yang Yang et al. utilized the CellaxTM platform to improve the safety and efficacy of podophyllotoxin (Cellax-PPT) and CTX (Cellax-CTX) against multidrug-resistant tumors [20].

Bacterial cellulose (BC) is a natural biopolymer [21,22] that has enormous potential in the field of biomedicine [23,24] owing to its exceptional physical features, including its flexibility, perfect water-holding capacity, high porosity; its chemical features, including its high crystallinity, high-level purity, foldability [25], elevated polymerization degree (DP), and simple of modification; and its biological characteristics, including its biodegradability, good affinity, non-biotoxicity, and highly biocompatible material [26], and non-allergenic [27]. BC comprises glucose monomer units polymerized into β-1-4 glucan chains by cellulose synthase, forming nano-fibrillar bundles with a uniaxial orientation [28,29]. Several different genera of bacteria are capable of producing cellulose [30,31]. Still, only strains of the genus Gluconacetobacter, with some strains renamed Komagataeibacter [32], have been discovered to produce cellulose in promising quantities [33]. BC production primarily depends on the availability of the nutritional components of the production medium, mainly carbon. Numerous carbon sources and cultivated media have been evaluated and reported; however, Hestrin-Schramm (HS) medium continues to be the most popular medium for BC fabrication. The expensive cost of production attributable to the medium (30 % of the total cost) poses a formidable obstacle to meeting commercial manufacturing requirements [34–36].

Because of their structural similarity to the extracellular matrix, BC-based composite materials have been commonly studied for various clinical applications; [37]. However, relatively few efforts have been reported in cancer treatment [38]. Multiple composite scaffolds based on BC have been developed and applied directly to cancer treatment. Various BC-based composite materials are designed. Shunsuke Akagi et al. developed innovative PTX formulations for bleomycin administration by combining PTX with either carboxymethylcellulose (CM)-Nano-fibrillated bacterial cellulose (NFBC) or hydroxypropyl cellulose (HP)-NFBC, and evaluated their efficiency against peritoneally disseminated stomach tumor in a xenograft nude mouse model [39].

Additionally, In vitro experiments on release also showed that the release rate was highest under neutral conditions, followed by alkaline conditions, and then acidic conditions [40]. This phenomenon was attributed to the pH dependence of the fibres' swelling and the drug's lower solubility under acidic conditions. Growing BC has prepared hybrid membranes in the presence of a hydroxyethyl cellulose (HEC) matrix. The BC-HEC bio-composite membrane exhibited higher tensile strength than the pure BC membrane and can be used for controlled drug delivery [41]. Paracetamol tablets coated with BC powder through spray drying have prolonged drug release [42].

Molecular Imprinting Polymers (MIPs) is a technique that relies primarily on the polymerization of specific functional monomers and crosslinkers in the existence of a template/analyte. This technique for modifying the surface of bacterial cellulose nanofibers is one of the most crucial surface modification methods [43,44]. In the first step of this procedure, a pre-arrangement of template molecules and functional monomers is utilized to create the pre-complex. The polymerization is completed after the crosslinker and pre-complex interactions that maintain the positions of functional groups to link the template molecule and produce the molecular recognition sites [45,46]. In the final stage of polymerization, the template molecules are extracted from the polymer, leaving recognition sites that are structurally and functionally complementary to the print molecules. The polymer can rebound the print molecules [47–49]. MIPs exhibited distinctive features, including high selectivity, sensitivity, excellent stability, reusability, ease of preparation, cheapness, and the capacity to be stored at room temperature [50]. Due to their high-level drug loading capacity and extreme-affinity binding sites, MIPs have important potential, particularly for drug release applications. In It is possible to modify the strength of interactions among the drug and imprinted sites to maintain drug release. In this drug release technology, MIPs are employed as an excipient to control drug release rate and/or timing.

Since Nicholls, Andersson, and Norell first published that MIPs could serve as sustained drug delivery devices for theophylline release, it has been proposed that MIPs can be used as excipients to improve the accuracy of drug release, thus dropping side effects reactions or enhancing bioavailability [51].

This study combined bacterial cellulose (BC) and molecularly imprinted polymer (MIPs) for anticancer prodrug delivery with controlled release. Cabazitaxel-imprinted microparticles were prepared onto BC nanofibers. In-vitro drug release assessments were conducted to assess the drug release performing from resulting composite nanofibers at varying temperatures of 25, 37, and 40 °C, concentrations of 0.5, 1, 2, 3, and 4 mg/mL, and different pH values (5.5, 6, 7, 7.4, and 8).

2. GENERAL INFORMATION

2.1. Cabazitaxel

Cabazitaxel (CTX) is a semisynthetic derivative of 10-Deacetylbaccatin III (10-DAB) extracted from yew needles in Europe. CTX is the 7,10-dimethoxy analogue of docetaxel [52] (Figure 2.1). Despite the similarity in alchemical structure among CTX, PTX, and DTX, CTX is more active, especially against resistant tumors, due to minor structural differences [53]. This benefit prompts new studies on the development of CTX formulations to replace the first generation of taxanes [54]. CTX is one of the tubulin in-inhibitors with similar properties and mechanisms of action to paclitaxel and docetaxel [55]. CTX inhibits the microtubular network in cells. CTX links to tubulin, promoting the assemblage of tubulin in microtubules while simultaneously dampening their disassembly [56], which leads to the inhibition of meiosis and interphase cellular functions (the cell is non-dividing). Subsequently, the cell loses its ability to proceed further into the cell-division cycle, which causes programmed cell death to be triggered in the cancer cells [57]. In mice that had human xenografts implanted in their bodies, CTX demonstrated a broad antitumor activity spectrum [58]. Nevertheless, CTX is characterized by very low water solubility [59].

JEVTANA (Sanofi-Aventis, Paris, France) certified marketing authorization via the European Commission on March 17, 2011, for the medication of patients with mCRPC formerly treated using a docetaxel-containing schedule [60]. The formulation of CTX injection known as JEVTANA, which is currently available for purchase, is solubilized with polysorbate 80. This formulation includes CTX with 60 mg per 1.5 mL of polysorbate 80. Because CTX has low solubility in water (hydrophobic anticancer drug) [61], in CTX formulations, the drug is solubilized using surfactants and polysorbate 80. Unfortunately, patients who received CTX were more likely to experience febrile neutropenia, neutropenic infection, haematuria, and diarrhea [62,63], which limits its clinical application. Several approaches have been studied to minimize the use of toxic surface-active agents and support targeted delivery of taxanes to tumor tissue [11]. One of these methods is the chemical conjugation of taxanes to suitable dissoluble high polymer carriers, for instance polysaccharides. This approach would enhance taxanes' pharmacokinetic and solubility profiles [64].

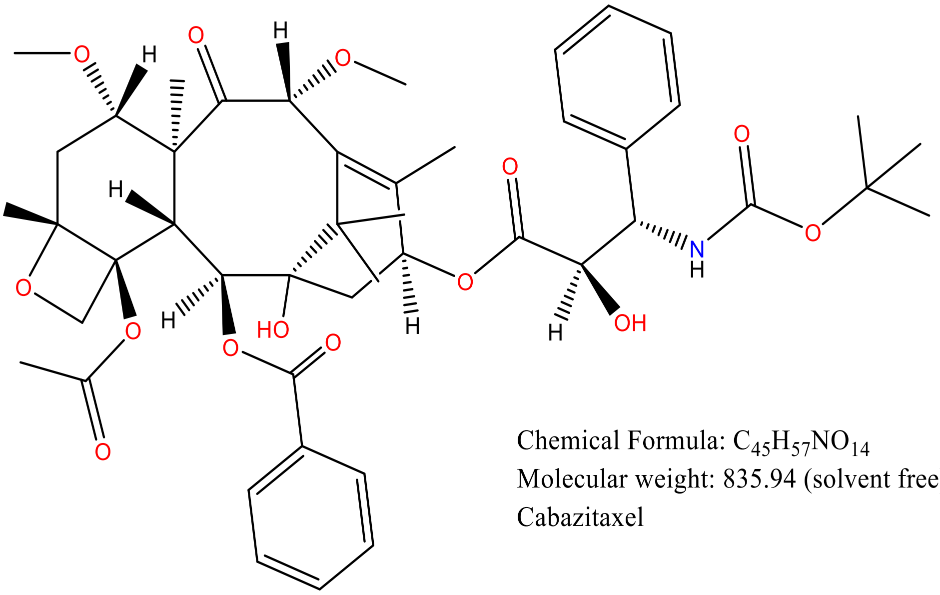

Chemical Formula: $C_{45}H_{57}NO_{14}$
Molecular weight: 835.94 (solvent free)
Cabazitaxel

(2a*R*,4*S*,4a*S*,6*R*,9*S*,11*S*,12*S*,12a*R*,12b*S*)-12b-acetoxy-9-(((2*R*,3*S*)-3-((*tert*-butoxycarbonyl)amino)-2-hydroxy-3-phenylpropanoyl)oxy)-11-hydroxy-4,6-dimethoxy-4a,8,13,13-tetramethyl-5-oxo-2a,3,4,4a,5,6,9,10,11,12,12a,12b-dodecahydro-1*H*-7,11-methanocyclodeca[3,4]benzo[1,2-*b*]oxet-12-yl benzoate

Figure 2.1. Chemical structure of CTX [59].

In addition, nanocarriers are another approach for increasing the solubility of CTX but also for extending the blood circulation time, which results in enhanced biological activity [65]. To improve the therapeutic ratio and efficacy, intensive research is currently being conducted on applying nanotechnology to the delivery of chemotherapy drugs [66]. Nanoparticles are believed to improve the accumulation of the practical component in tumors owing to the increased permeability and retention effect, which results from a leaking and highly abnormal vascular system of the tumor through improving retention results from the disordered lymphoid system that is characteristic of malignant tumors [67].

2.2. Bacterial Cellulose (BC)

Bacterial cellulose BC is called microbial cellulose, nanocellulose, and biocellulose [68]. BC is a form produced by various bacterial species [69]. It comprises D-glucose units coupled by β-(1-4)-glycosidic bonds, creating glucan chains with the formula [$(C_6H_{10}O_5)n$] [70], (Figure 2.2) demonstrates the molecular structure.

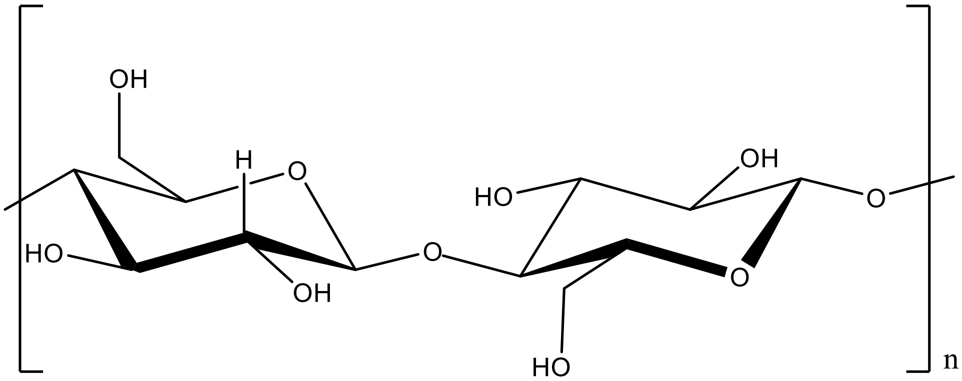

Figure 2.2. Chemical structure of bacterial cellulose [29].

First reported in 1988 by Brown [71]. Unlike Cellulose nanocrystals (CNC) and cellulose nanofibrils (CNF), BC is produced by bacteria from low molecular weight sugar to form nanofibers (top-up process). Consequently, cellulose is free of impurities and contaminants such as wax, lignin, pectin, and hemicellulose, commonly found in CNC and CNF products [68].

BC is produced primarily from glucose, but it has also been reported to be manufactured from several other sugar sources, involving fructose, galactose, and sucrose [72]. BC is synthesized via a sequence of basically bacterial enzymatic reactions that occur inside the bacterium, in which carbohydrates are transformed into glucose and subsequently polymerized into cellulose chains [73]. In static or even dynamic conditions, with different yields depending on the culture media's species and substrate. The resultant BC consists primarily of water (> 99%) and a network of nanofibers with a fibre diameter of 20–100 nm [74]. Consequently, bacterial nanocellulose is much thinner than cellulose extracted from plants [75].

BC is insoluble in water due to its molecular structure but partially soluble in organic solvents. It has a high capacity to hold water and unique mechanical properties due to the BC nano fibrillar three-dimensional (3D) structure composed of randomly orientated nanofibers [76,77].

By comparison to other types of cellulose BC has several advantages, including its ultrafine particles (UFPs) network purity, high water-swelling capacity, crystallinity, degree of polymerization (xn), biodegradability, biocompatibility, and effective mechanical properties [78,79]. On the other side, the high-cost production of BC currently poses a significant obstacle to its widespread commercial adoption. Summary of the characteristics of bacterial cellulose (Table 2.1.)

Table 2.1. The characteristics of bacterial cellulose nanofibers [68].

Size		Shape	Nanocellulose structure	Production process	Impurity
Length	Diameter				
More than 1 μm	20–100 nm	A fine fibre network (nanofiber)	high crystallinity	Bottom-up	No hemicellulose, pectin, and lignin

2.2.1. BC-Based Composites with Various Materials and Their Applications in Cancer Therapeutics

Cellulose is particularly attractive polymer for combination of composite materials by means of hydrogen bonding through the hydroxyl groups (OH), which promote steric entanglement in nanocomposite retention. This makes it possible to retain composite materials, such as layered double hydroxide (LDH), that interact strongly with (OH) groups [80,81].

Marina de Lima Fontes et al. synthesized biocomposites of bacterial cellulose/carboxymethylcellulose (BC/CMC). Then, biocomposites were loaded with the immunosuppressant and anticancer drug methotrexate (MTX), which offered an alternative topical treatment for Psoriasis Vulgaris [82]. They hypothesized that changing the ratio of CMC to BC would influence the scaffold's properties and drug release kinetics. Moreover, BC/algin composites simulate tumor microenvironments by forming complex polymeric networks with enhanced Adriamycin affinity and surface area. BC-Algin composites with Adriamycin decreased the cell capability of HT-29 human colon adenocarcinoma cell lines from 95% to 63% and 37% after 24 and 48 hours, respectively, respectively [83].

Freeze drying has been utilized in yet another investigation into the process of producing multiple BC scaffolds. This time, the BC scaffolds' macropores were the investigation's focus. After cultivating the MDA-MB-231 cell line, the scaffolds' integrity was evaluated. The investigation revealed that microporous BC scaffolds supported cell feasibility, cohesion, and propagation, making them an excellent model for studying the tumor microenvironment [84].

2.3. Molecular Imprinting Polymers

Molecularly imprinted polymers (MIP) are polymeric matrices capable of selectively binding specific molecules. The technique of molecular imprinting involves the polymerization of monomers in the existence of a target molecule, which serves as a template during polymer synthesis. The affinity of the resulting products is comparable to that of the affinity antibody-antigen [85–89].

In 1931, Polyakov presented the idea of molecular imprinting for the first time, describing it in his paper as "unusual adsorption properties of silica particles prepared using a novel synthesis procedure." This was the first time that this idea had been publicly reported. The aforementioned "unusual adsorption properties" have been reported with the use of a variety of polymers, which are now known as molecularly imprinted polymers [90].

Imprinting techniques used today started in Europe in the 1970-1980s by German scientist Günter Wulff and Swedish scientist Klaus Mosbach, respectively [91,92]. (Table 2.2.) provides a comparison of natural biomolecules with MIPs.

Table 2.2. The comparison of MIPs and natural biomolecules.

MIPs	Natural biomolecules
- MIPs are characterized by their stable spatial structure.	- poor stability [98].
- Lengthy shelf life can be up to several years, even when stored at room temperature [93].	- short-lasting shelf life.
- Possess exceptional physical toughness and stability in harsh conditions, such as highly acidic and basic pH, organic solvents, fluctuating temperature, and mechanical and thermal pressures[94–96].	- Not stable in the same conditions [99].
- Reusable.	- Non-reusable.
- low cost [97].	- Expensive.

2.3.1. Types of Molecular Imprinting Methods

Numerous methods for preparing MIPs have been developed. According to Ndunda et al.'s article, these can be roughly categorized into covalent, noncovalent, semi-covalent, and metal-ion exchange imprinting methods [100].

2.3.1.1. The Covalent Imprinting Method

Introduced by Wulff in 1995 [101]. The covalent imprinting method (CPM) forms a covalent bond among the template molecule and the suitable monomer. The covalent bond is then severed during polymerization, followed by the removal of the template. The same covalent linkage reappears upon rebinding the previously removed template. The primary advantage of this method is that it produces a polymer with a very uniform distribution of binding sites [102]. Figure 2.3 shows the schematic illustration of covalent imprinting mechanisms.

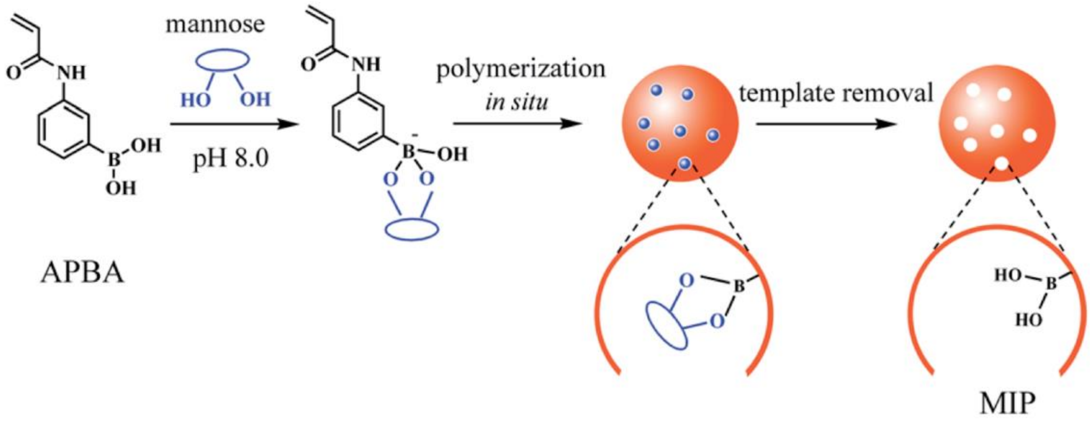

Figure 2.3. Schematic illustration of the covalent imprinting mechanisms of the molecular imprinting process [103].

2.3.1.2. The Non-Covalent Imprinting Method

Mosbach and his team in Sweden developed in the late 1980s, the non-covalent imprinting method (NCPM), also known as self-assembly [104]. NCPM is the most common type of interaction and depends primarily on the formation of secondary interactions between functional monomers and the related target molecule in a pre-polymerized mixture. Hydrophobic interaction, dipole-dipole forces, H-bonding, Van der

Waals forces, ionic interactions, and electrostatic interactions are examples of these interactions [105]. (Figure 2.4) shows the Schematic illustration of non-covalent imprinting mechanisms.

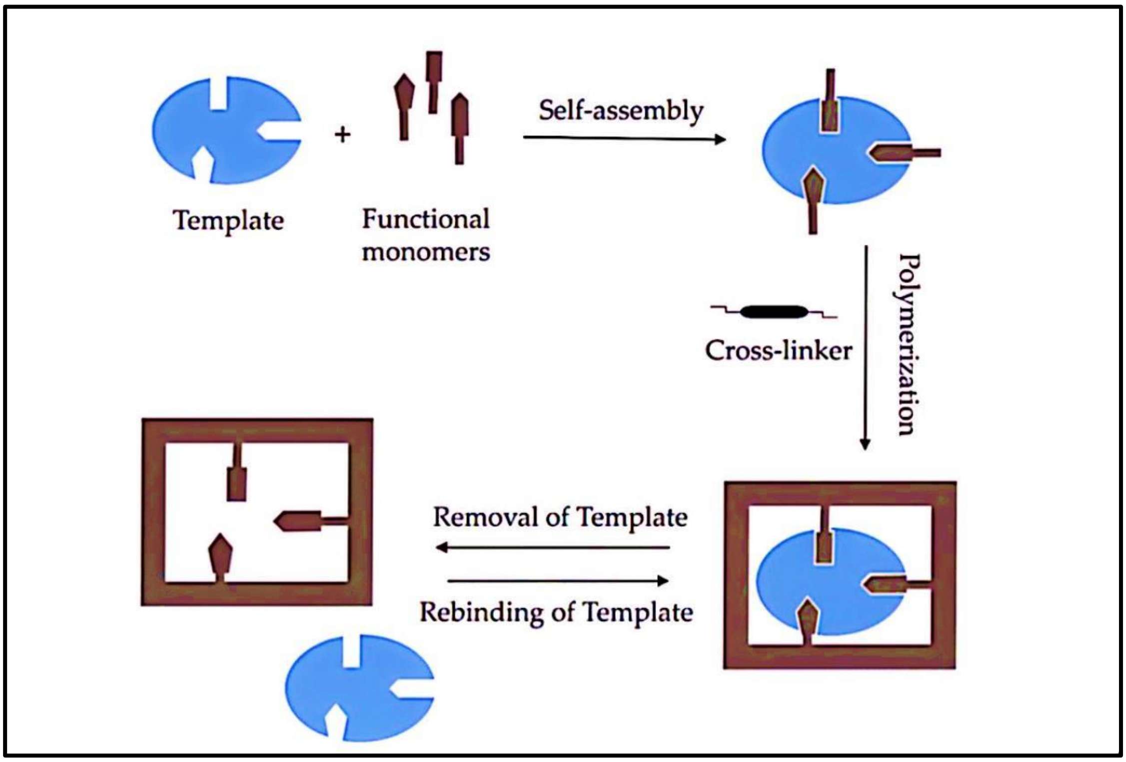

Figure 2.4. Schematic illustration of the non-covalent imprinting mechanisms of the molecular imprinting process [106].

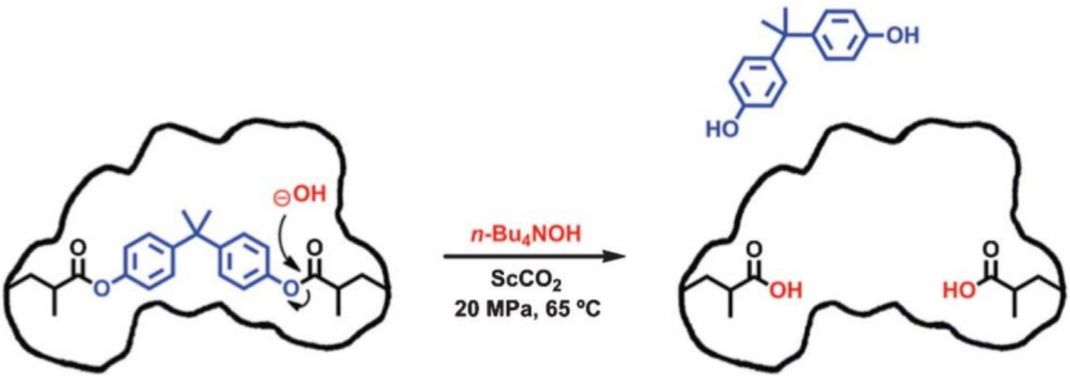

Figure 2.5. Schematic illustration of the semi-covalent imprinting mechanisms of the molecular imprinting process [107].

2.3.1.3. The Semi-Covalent Imprinting Method

In their study, Whitcombe et al. first reported the semi-covalent method [108]. Semi-covalent imprinting method incorporates both CPM and NCPM processes, enabling subsequent rebinding by a non-covalent bond following the removal of a covalently-bound template [109–111]. (Figure 2.5) shows the Schematic illustration of semi-covalent imprinting mechanisms.

2.3.1.4. The Metal-Ion Exchange Method

Metal ions can serve as template molecules or as components of interaction among analyte and functional monomer [112,113]. In metal-mediated interactions, the metal ion is complexed with a polymerizable ligand (or ligands) and a template. The interaction can be as strong as a covalent bond, depending on the oxidation condition of the metal and the ligand characteristics [114]. (Figure 2.6) shows the Schematic illustration of metal-ion imprinting mechanisms.

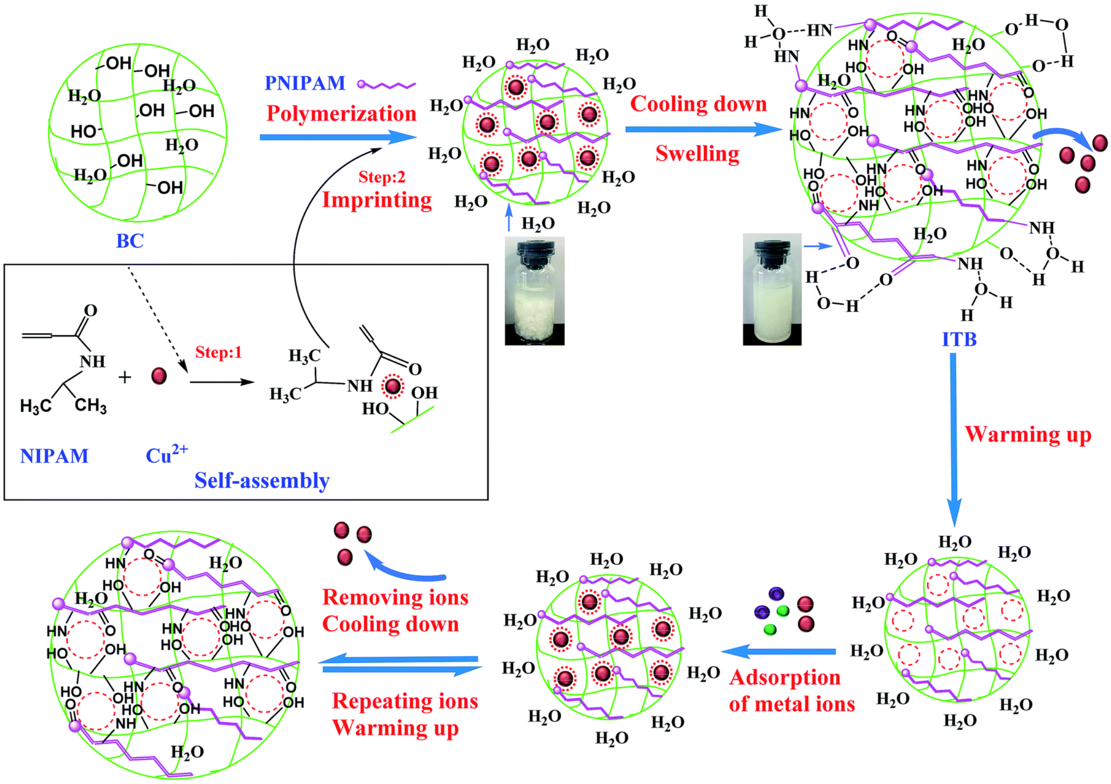

Figure 2.6. Schematic illustration of the metal-ion exchange imprinting mechanisms of the molecular imprinting process [115].

2.3.2. Synthesis Process of Molecular Imprinting Polymers

The process of MIPs synthesis shown in (Figure 2.7) can be divided into 3 main steps, which are as follows:

- The first step, known as pre-polymerization, refers to the process that involves the formation of a complex of functional monomer and template in a solution [116];
- The second step, known as polymerization, is the existence of a cross-linker.
- The final step is removing the template (drug) [117].

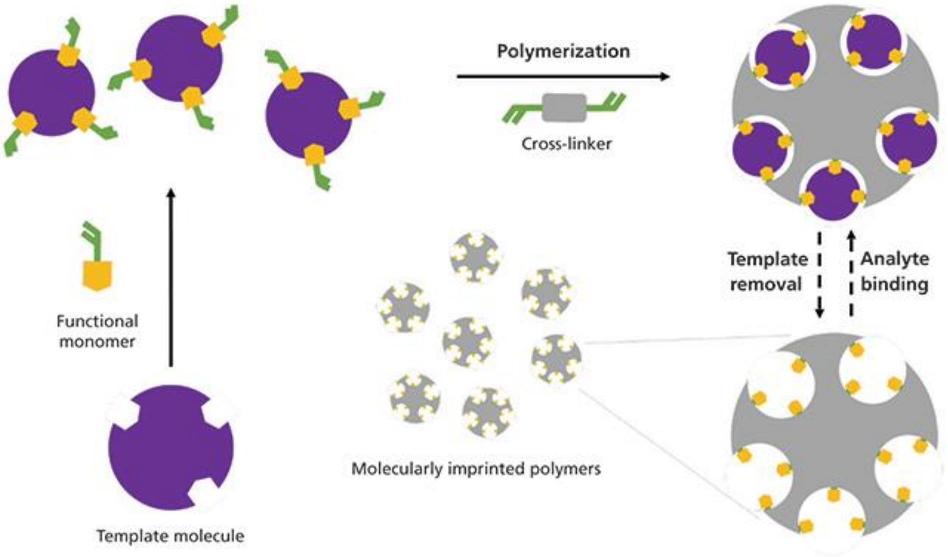

Figure 2.7. Schematic illustration of the molecularly imprinted process [118].

2.3.3. The Essential Components of The Molecular Imprinting Process

The highly significant considerations in the molecular imprinting process are the selection of the most suitable monomer, cross-linker, initiator, and solvent for the template molecule, as well as the ratio between reagents, polymerization technique, and imprinting method (Table 2.3.) [119].

Table 2.3. The most important functional monomers, crosslinkers, solvents, and initiators are used in the synthesis MIPs.

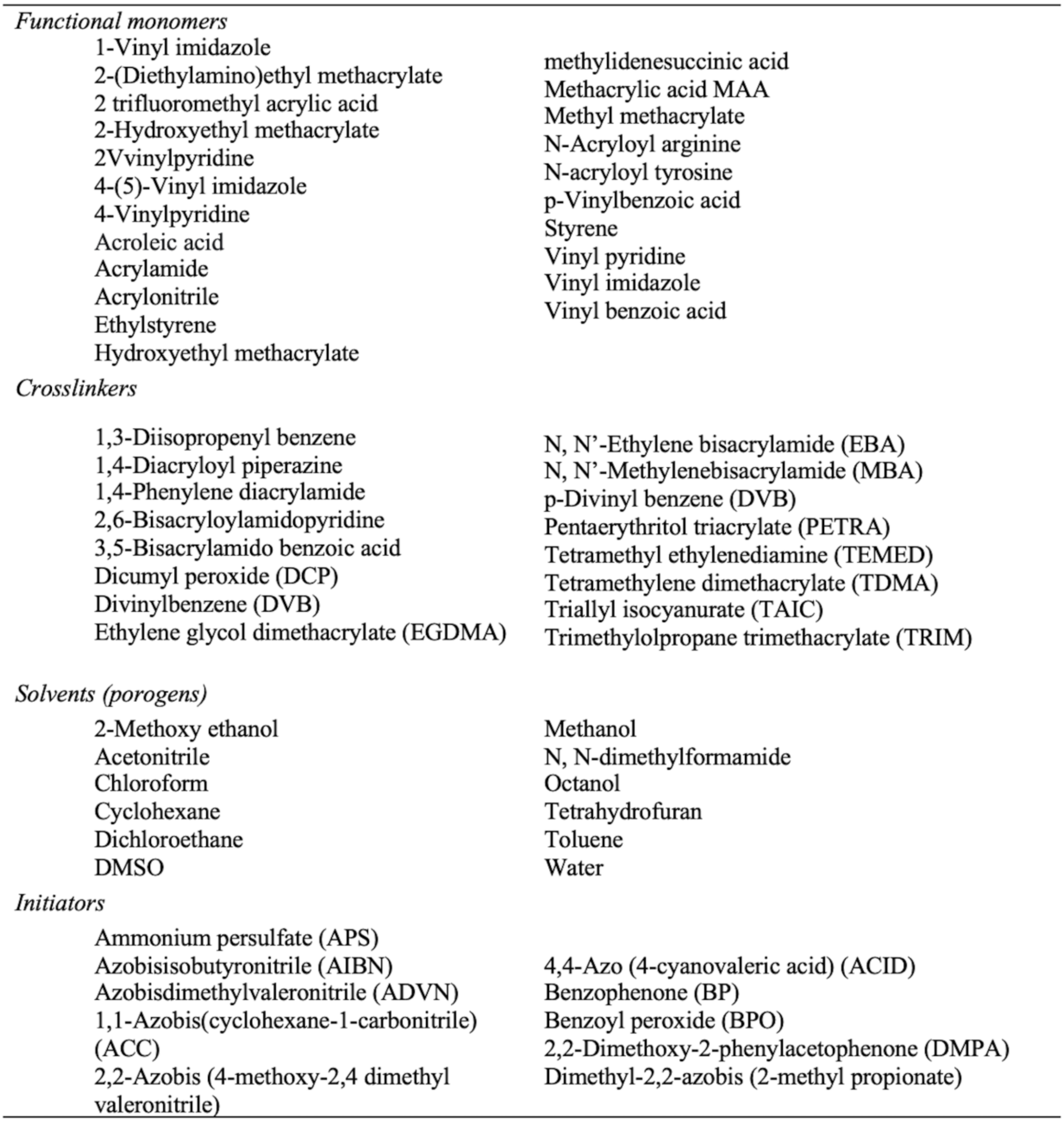

Functional monomers

1-Vinyl imidazole
2-(Diethylamino)ethyl methacrylate
2 trifluoromethyl acrylic acid
2-Hydroxyethyl methacrylate
2Vvinylpyridine
4-(5)-Vinyl imidazole
4-Vinylpyridine
Acroleic acid
Acrylamide
Acrylonitrile
Ethylstyrene
Hydroxyethyl methacrylate
methylidenesuccinic acid
Methacrylic acid MAA
Methyl methacrylate
N-Acryloyl arginine
N-acryloyl tyrosine
p-Vinylbenzoic acid
Styrene
Vinyl pyridine
Vinyl imidazole
Vinyl benzoic acid

Crosslinkers

1,3-Diisopropenyl benzene
1,4-Diacryloyl piperazine
1,4-Phenylene diacrylamide
2,6-Bisacryloylamidopyridine
3,5-Bisacrylamido benzoic acid
Dicumyl peroxide (DCP)
Divinylbenzene (DVB)
Ethylene glycol dimethacrylate (EGDMA)
N, N'-Ethylene bisacrylamide (EBA)
N, N'-Methylenebisacrylamide (MBA)
p-Divinyl benzene (DVB)
Pentaerythritol triacrylate (PETRA)
Tetramethyl ethylenediamine (TEMED)
Tetramethylene dimethacrylate (TDMA)
Triallyl isocyanurate (TAIC)
Trimethylolpropane trimethacrylate (TRIM)

Solvents (porogens)

2-Methoxy ethanol
Acetonitrile
Chloroform
Cyclohexane
Dichloroethane
DMSO
Methanol
N, N-dimethylformamide
Octanol
Tetrahydrofuran
Toluene
Water

Initiators

Ammonium persulfate (APS)
Azobisisobutyronitrile (AIBN)
Azobisdimethylvaleronitrile (ADVN)
1,1-Azobis(cyclohexane-1-carbonitrile) (ACC)
2,2-Azobis (4-methoxy-2,4 dimethyl valeronitrile)
4,4-Azo (4-cyanovaleric acid) (ACID)
Benzophenone (BP)
Benzoyl peroxide (BPO)
2,2-Dimethoxy-2-phenylacetophenone (DMPA)
Dimethyl-2,2-azobis (2-methyl propionate)

2.3.3.1. Templates

The target compounds the researchers are interested in or aim to separate, detect or load for delivery are templates. These target compounds include small molecule organic matter, DNA, protein, nucleic acid [120], viruses, micro-organisms, or nanoparticles [121,122]. In general, a perfect template molecule should fulfill the 3 conditions listed below: Firstly, the template molecule should not include groups engaged in or forbidding polymerization. Secondly, it must be chemically stable during the polymerization process. Lastly, the template must be sufficiently active to create a pre-polymerization complex with monomer [123].

2.3.3.2. Functional monomers

As a result of the functional groups that monomers possess, they can interact with the template molecule. This interaction results in creating a pre-polymerization complex, an essential step in MIP production. It can be seen that its structure contains two distinct kinds of elements: those that can identify and interact with the template and those capable of polymerization [118,124]. (Figure 2.8) shows the widely used functional monomers.

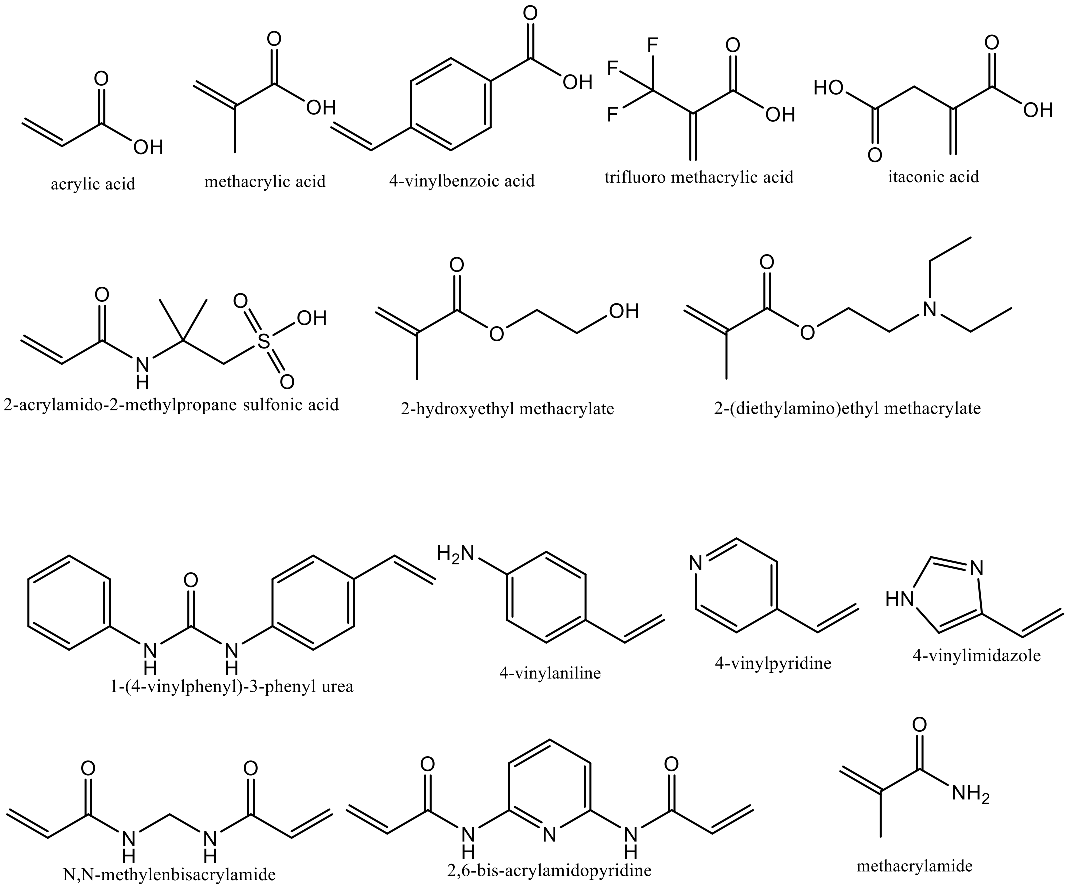

Figure 2.8. Scheme of commonly used monomers [125].

2.3.3.3. Cross-linkers

A cross-linker is an organic (or, in rare cases, inorganic) compound that is together with the polymerization mixture to fix the monomer molecules to the template molecules. The cross-linker employed during polymerization is a significant element in determining the properties of MIPs. When cross-linker quantity is too low, mechanical properties become unstable. In the construction of MIPs, cross-linker has three primary purposes.: Firstly, dominating the morphology of the matrix of the polymer. Secondly, it helps the imprinted binding sites to stabilize. Lastly, it provides the polymer matrix with mechanical stability [126,127]. (Figure 2.9) presents widely used cross-linking agents.

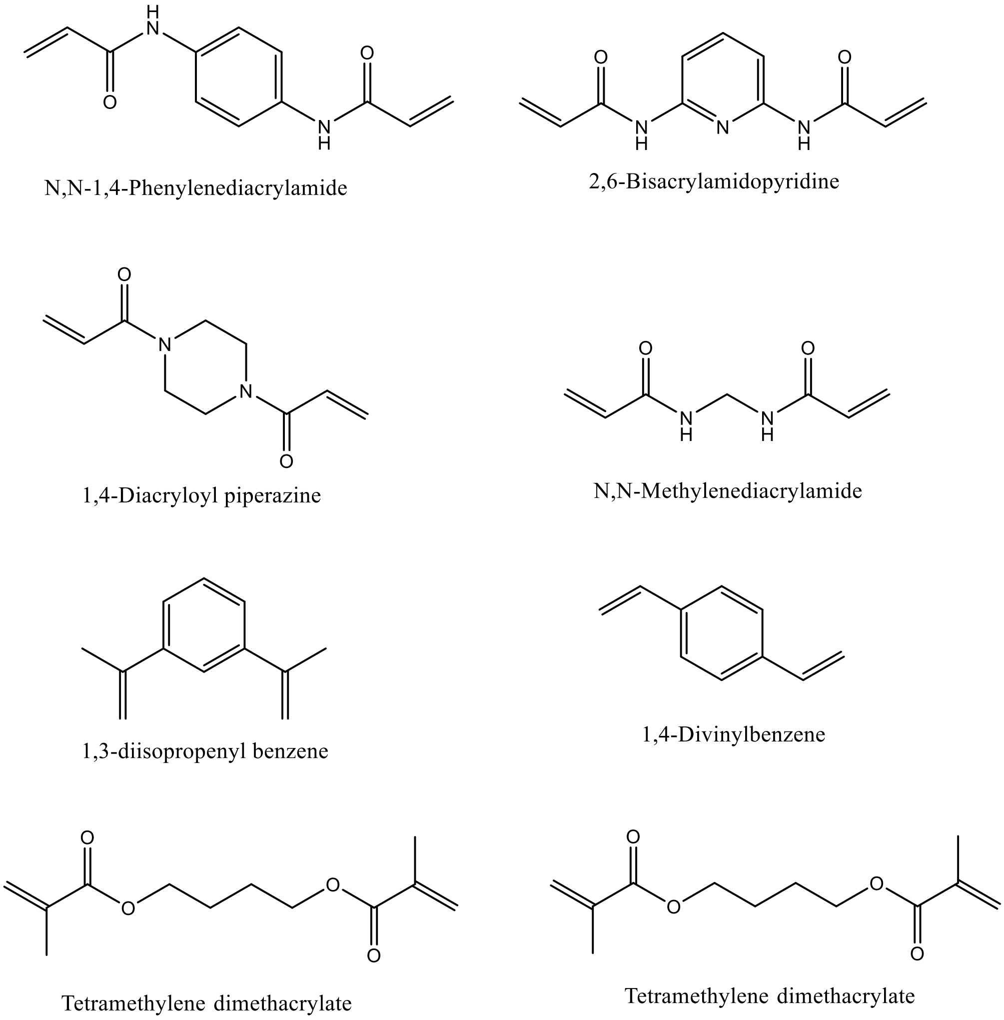

N,N-1,4-Phenylenediacrylamide

2,6-Bisacrylamidopyridine

1,4-Diacryloyl piperazine

N,N-Methylenediacrylamide

1,3-diisopropenyl benzene

1,4-Divinylbenzene

Tetramethylene dimethacrylate

Tetramethylene dimethacrylate

Figure 2.9. Scheme of the most common cross-linking agents [118].

2.3.3.4. Initiators

An initiator in the polymerization mixture is responsible for the reactive species' initiation. There are three main categories of initiators: thermal, redox, and photo. The most popular thermal initiators are benzoyl peroxide and azobisisobutyronitrile [128]. (Figure 2.10) presents widely used initiators.

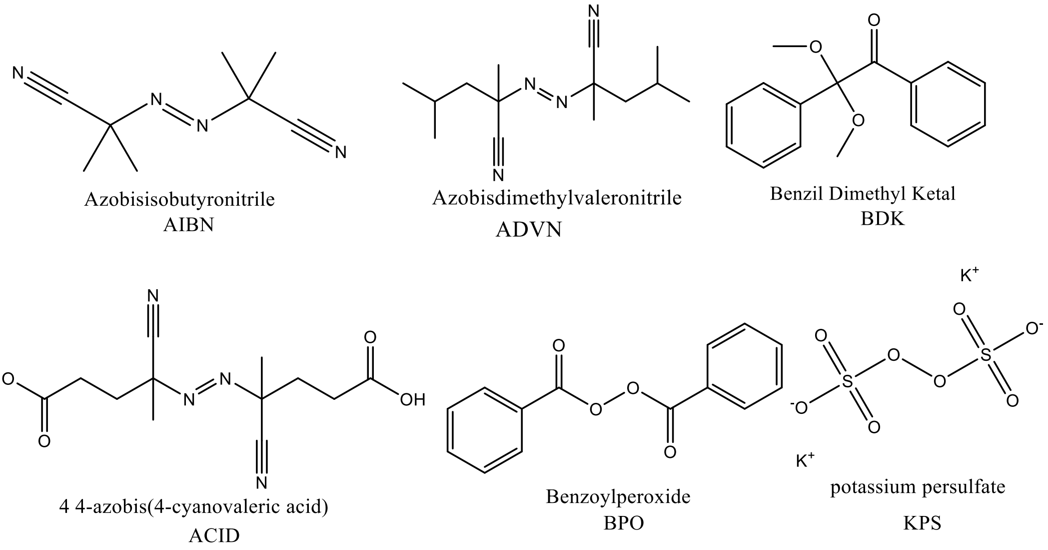

Azobisisobutyronitrile
AIBN

Azobisdimethylvaleronitrile
ADVN

Benzil Dimethyl Ketal
BDK

4 4-azobis(4-cyanovaleric acid)
ACID

Benzoylperoxide
BPO

potassium persulfate
KPS

Figure 2.10. Scheme of the most common initiators [129].

2.3.3.5. Solvents/Porogens

The final component of the chemical system that has a sizeable effect on forming MIPs is the solvent/porogenic. In most cases, it plays an essential role during polymerization by acting as a dispersion medium and pore-forming agent. The most common solvents are ethylene glycol monomethyl ether acetate, methanol, oxolane, 2-propanol (iPrOH), acetonitrile (ACN), trichloromethane [130], and dichloromethane [18]. A porogenic ought to own the following characteristics: Firstly, all the used chemical additives must be solvable in the selected solvent. Secondly, porogenic ought to create big pores to guarantee the flow-through properties of the polymer. Lastly, it ought to have low polarity to keep away from interferences for the duration of the formation of complexes in the MIPs process [8].

2.3.4. Molecular Imprinting Polymers Synthesis Methods

There are multiple MIP production methods, but all of the methods follow the same basic outline. Table 2.4 shows various MIPs synthesis methods.

Table 2.4. Various MIPs synthesis methods. Modified and extracted from (ref. [131–136]).

Synthesis Methods	**Advantage**	**Disadvantage**
Bulk: A small amount of solvent is used to polymerize the template molecule, functional monomers, and initiator.	- No additional solvent is needed - The easy control over the size of the MIP particles - Low cost - Easy in preparation	- The obtained MIP requires grinding - Some irregularities in the shape of the particles - Requires a high amount of porogen agent
Suspension: polymerization takes place inside the droplets, in the presence of surfactants, droplets of the pre-polymerization mixture are suspended in an immiscible phase (eg, water).	- Regular shape MIP microspheres are obtained - A MIP film with high porosity is obtained	- A reaction mixture that contains both aqueous and organic phases is required - The presence of a stabilizer and a surfactant is mandatory - The monomer and the initiators are hydrophobic
Seed: A porous particle (seed) is used as a scaffold structure upon which the polymerization takes place.	- Sub-micron-sized particles are used - The polymerization takes place at the surface of the particles - The thickness of the polymeric layer can be easily controlled - Largely, equal in size and shape particles are obtained	- Involves time-consuming procedure - Requires the use of an aqueous suspension that potentially interferes with imprinting.
Emulsion: The monomer phase is suspended in an immiscible phase (eg, water). The polymerization takes place inside a monomer droplet, which are enclosed in micelles and stabilized by surfactants.	- It is not necessary to add any stabilizer or surfactant to produce monodisperse MIP beads by using this technique	- A hydrophilic initiator, a hydrophobic monomer and an emulsifier agent needed
Core-shell: obtaining core-shell MIP nanoparticles require two stages. The first stage is the formation of a solid nanocore (Seed particle), and the second is the grafting of an imprinted shell.	- Allows the formation of recognition sites at the surface of MIP beads	- Not effective for bulky templates
Precipitation: Similar procedure to bulk imprinting, but with a higher amount of solvent used. The polymeric chains do not overlap to create a network, but continue to grow individually, until they reach a critical mass and precipitate.	- Regular shape MIP beads are obtained in good yields - The polymeric chains are growing individually to microspheres - The presence of porogen agents in the reaction mixture is not necessary - Easy procedure and less time consuming	- Precipitation only takes place when the polymeric chains are large enough to be insoluble in the reaction mixture
Solid-phase: involves three main steps: preparation of the glass beads by activation and silanization; immobilization of the template on silanized glass beads; and finally, polymerization and purification.	- The possibility of re-using templates attached to the solid phase - More homogeneous distribution of recognition sites - The 'inbuilt' affinity purification yields high-affinity nanoMIPs -	- Low yield - Ineffective for bulky and thermosensitive templates
Sol-gel: in this process, a colloidal solution is poly-condensed into a solid phase.	- Easy controllable pores size - High mechanical stability - High thermal stability	- Low sensitivity - Slow kinetics - Low response time

2.4. Non-Imprinted Polymers (NIPs)

In developing any MIPs technique, non-imprinted polymer (NIP), also known as a control polymer, is produced (under the same conditions as the corresponding MIP, but without a template molecule) and evaluated in parallel with the MIP. This is done to compare the results of the two polymers. This is done so that imprinted sites in the MIPs can be demonstrated [137] (Figure 2.11). NIPs serve as a "control" to assess the electricity of interactions between synthesized MIPs and the template that are specific for MIPs but non-specific for NIPs [138]. To conduct binding tests, the exact amounts of MIPs and NIPs are added to solutions containing a pre-agreed concentration of the template molecule, measuring the bound concentration [139].

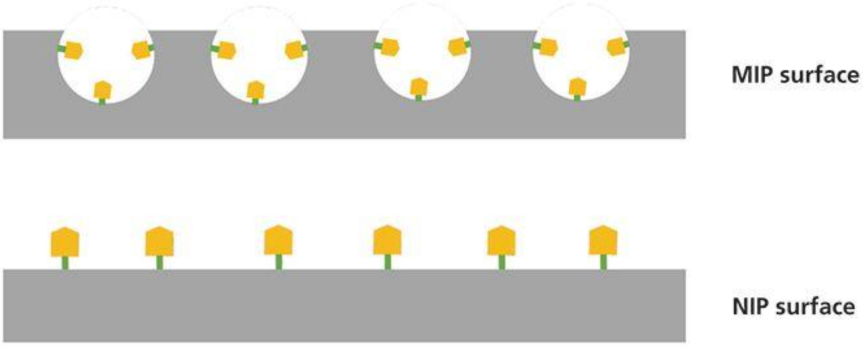

Figure 2.11. Schematic illustration of Comparison of MIP and NIP surface. Imprinted cavities on the MIP surface interact specifically with the templates, whereas the NIP surface interacts non-specifically.

3. EXPERIMENTAL PART

3.1. Materials

Item No.	Materials	Company
1	JEVTANA® (Cabazitaxel) ($C_{45}H_{57}NO_{14}$)	Sanofi S.A.
2	Succinic Anhydride ($C_4H_4O_3$)	Sigma-Aldrich
3	4-Dimethylaminopyridine ($C_7H_{10}N_2$) (DMAP)	Sigma-Aldrich
4	Anhydrous Pyridine (C_5H_5N)	Fluka
5	Dichloromethane (CH_2Cl_2) ≥99.8%	Sigma-Aldrich
6	Hydrochloric Acid (HCl)	Sigma-Aldrich
7	Saturated Sodium Bicarbonate ($NaHCO_3$)	Sigma-Aldrich
8	Anhydrous Sodium Sulfate (Na_2SO_4)	Sigma-Aldrich
9	*Komagataeibacter intermedius*	Hacettepe University-Biotechnology Department-Culture Collection Laboratory
10	Glucose ($C_6H_{12}O_6$)	Sigma-Aldrich
11	Peptone ($C_{13}H_{24}O_4$)	Sigma-Aldrich
12	Yeast Extract ($C_{19}H_{14}O_2$)	Sigma-Aldrich
13	Disodium Hydrogen Phosphate (Na_2HPO_4)	Sigma-Aldrich
14	Citric Acid	Sigma-Aldrich
15	NaOH	Merck
16	[3-(Methacryloyloxy) Propyl] Trimethoxysilane ($C_{10}H_{20}O_5Si$) (3-MPS)	Sigma-Aldrich
17	Toluene (C_7H_8) 99.9%	Sigma-Aldrich
18	N, N-Methylenebis Acrylamide (MBAAm, M7279)	Sigma-Aldrich
19	Methacrylic Acid ($C_4H_6O_2$) (MAA)	Sigma-Aldrich
20	2,2′-Azobis(2-Methylpropionitrile) 98% ($C_8H_{12}N_4$) (AIBN)	Sigma-Aldrich
21	Sodium Chloride Extra Pure (NaCl)	Merck
22	Phosphate Buffered Saline ($C_{l2}H_3K_2Na_3O_8P_2$) (PBS)	
23	Dipotassium Hydrogen Phosphate (K_2HPO_4, 60356)	Sigma-Aldrich
24	Potassium Dihydrogen Phosphate (KH_2PO_4, 04243)	Sigma-Aldrich
25	Plasma	Tokra Medikal

3.2. Methods

3.2.1. Synthesis of Carboxyl-Activated CTX

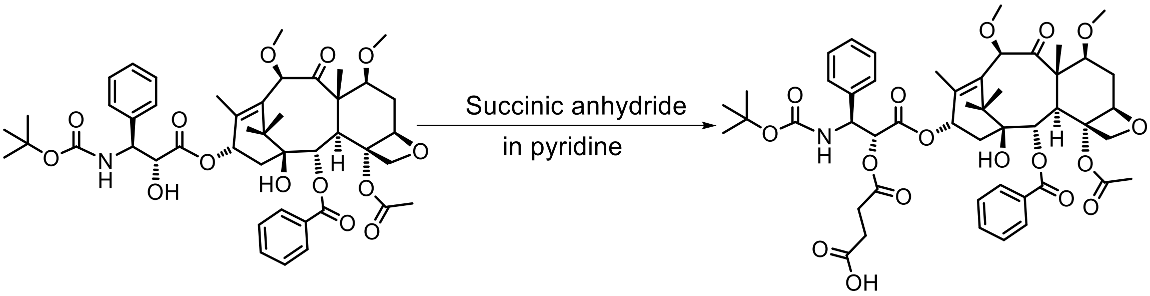

Figure 3.1. Synthetic scheme of carboxyl-activated CTX.

Based on the previously published work, CTX prodrug synthesis was confirmed (Figure 3.1) [64]. Cabazitaxel (180 mg, 0.215 mmol) was mixed with succinic anhydride (64,952 mg, 0.645 mmol) in anhydrous pyridine (0.5 mL) containing 4-dimethyl aminopyridine (DMAP) (2,631 mg, 0.0215 mmol), and the combination was stirred at 40°C for 4 hours. After the anhydrous pyridine was eliminated, dichloromethane was added, and the organic solvent was washed with 0.1 M hydrochloric acid, a saturated sodium bicarbonate solution, and brine (Figure 3.2). To produce carboxyl-activated CTX, the organic layer was dried over sodium sulphate anhydrous, filtered, and then concentrated under a vacuum. (137.6 mg, 68.27% yield).

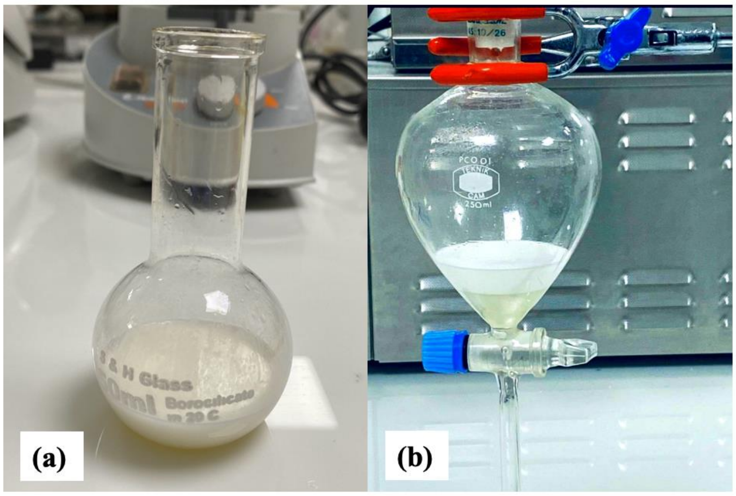

Figure 3.2. Cabazitaxel (a) The reaction mixture; (b) formation of two layers.

The general procedure that must be followed to prepare a calibration standard curve by UV-VIS spectrophotometer (UV):

UV: A stock solution of carboxyl-activated CTX (3 mg/ml) was produced using a Phosphate buffered saline (PBS) pH of 7.4. Later the same solution was utilized for required subsequent dilutions. A series of 1 ml vials containing various standard solutions were made up using a Phosphate-buffered saline (PBS) with a pH of 7.4. The absorbance of these solutions was measured using a quartz cuvette and a UV-VIS spectrophotometer at a wavelength of maximum absorbance of 296 nm. To create a standard calibration curve, absorbance values were plotted against concentration [140].

3.2.2. Production of Bacterial Cellulose

Based on the previously published work [141], bacterial cellulose was synthesized. This study utilized the Hacettepe University, Biotechnology Department, Culture Collection Laboratory *Komagataeibacter intermedius* strain. For a primary culture, the bacterial strain was introduced into standard Hestrin-Schramm (HS) medium broth (containing, in g/L: 20 glucose, 5 peptone, 5 yeast extract, 2.7 disodium phosphate, and 1.15 citric acid). The cultures were incubated statically at 30°C for seven days (MCI 120; Mipro, Ankara, Turkey).

3.2.2.1. Separation and Purification of Bacterial Cellulose

After incubation, the BC nanofiber membranes were removed from the culture medium and centrifuged for 15 minutes at 2993 x g. (Eppendorf 5417R Refrigerated Centrifuge, Hamburg, Germany). To rid of adherent cells, BC nanofiber membranes were washed with ultrapure water and treated for 1 hour with a 1M NaOH solution at 80°C. BC was then washed with ultrapure water to remove culture medium components and other residues until they reached a pH of 7.0 and turned white [142].

3.2.3. Production of Bacterial Cellulose Composites

Firstly, 10 mm diameter BC nanofibers membranes were fabricated using a locally-made disc fabricator and reacted at 80°C for 6 hours with 3-MPS (10 percent by weight) in toluene [143]. Following this step, the resulting modified bacterial cellulose nanofibers (M-BC) were washed three times with CH_3OH and ultrapure water. Second, MAA as a functional monomer was treated for 1 h at 25°C with carboxyl-activated CTX molecules, which served as template molecules, to shape a pre-polymerization complex. M-BC nanofibers and carboxyl-activated CTX-monomer complex were combined in glass Petri plates with MBAAm serving as the crosslinking monomer and AIBN serving as the polymerization initiator. The petri dish was exposed to a 100 W, 365 nm UV light source for 1 h. MIPs composites, namely MIP1, MIP2, and MIP3 were prepared by varying the carboxyl-activated CTX /MAA ratio while maintaining the crosslinker, and the initiator amounts constantly. The preparation compositions utilized can be found in (Table 3.1.). The same procedure was followed to prepare Blank NIP in the absence of carboxyl-activated CTX.

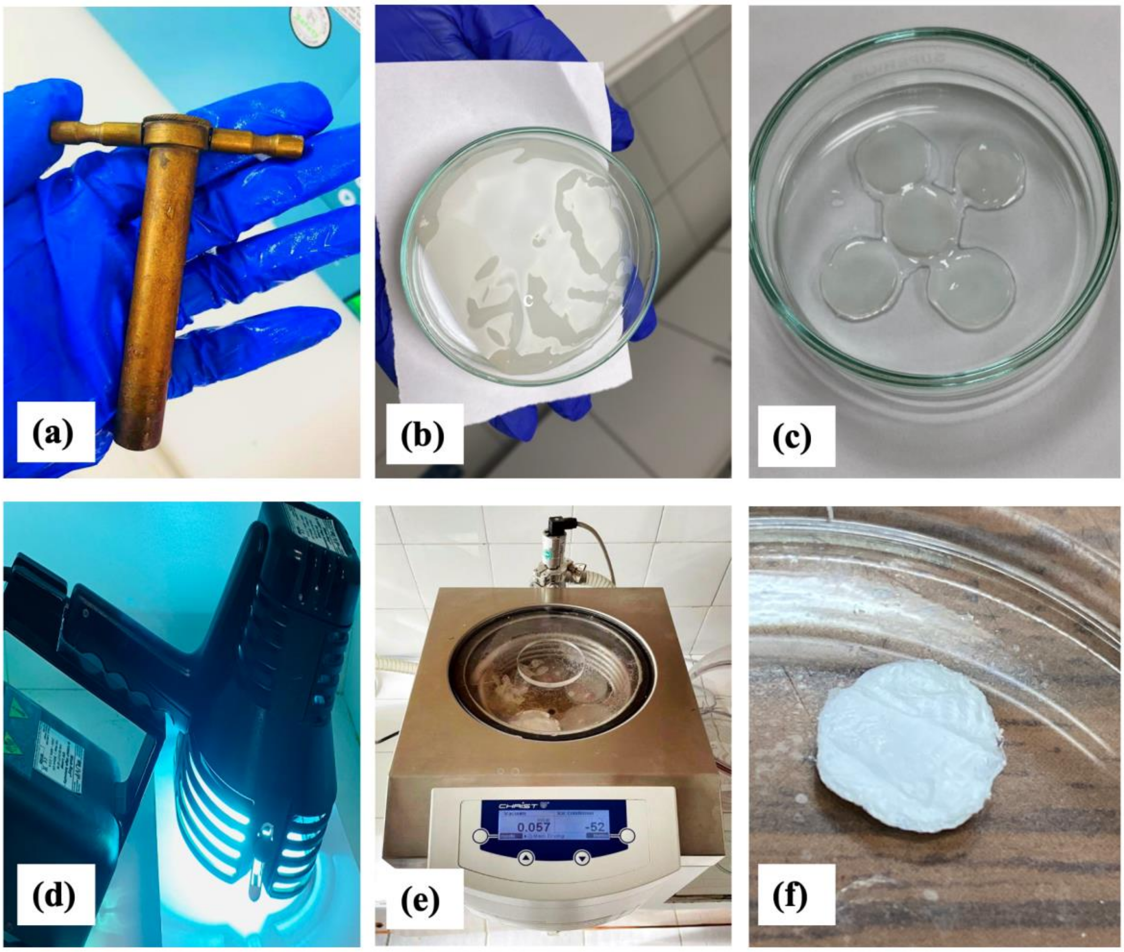

Figure 3.3. (a) Disc fabricator; (b) & (c) images of BC nanofibers before and after cutting; (d) ultraviolet light systems; Christ ALPHA 2-8 LD Plus Freeze dryer (e) and freeze-dried BC nanofibers (f).

To remove impurities and unreacted chemicals, the matrices were washed three times with 15 mL of ultrapure water at the end of the polymerization. The template was then eliminated with 0.5 M sodium chloride for 3 hours at 25°C and freeze-dried for 8 hours at -52°C and 0.057 mBar (Figure 3.3). The formulation method was illustrated schematically in (Figure 3.4).

Table 3.1. The recipe for the synthesis method of composite BC nanofibers.

Composite BC nanofibers	MAA (mmol)	Carboxyl-activated CTX, (mmol)	Carboxyl-activated CTX /MAA	MBAAm (mmol)
MIP1	1 (86) mg	0.013(12.5) mg	1:05	0.097(15) mg
MIP2	1 (86) mg	0.027(25) mg	1:10	0.097(15) mg
MIP3	1 (86) mg	0.05(50) mg	1:20	0.097(15) mg
NIP	1 (86) mg	-	-	0.097(15) mg

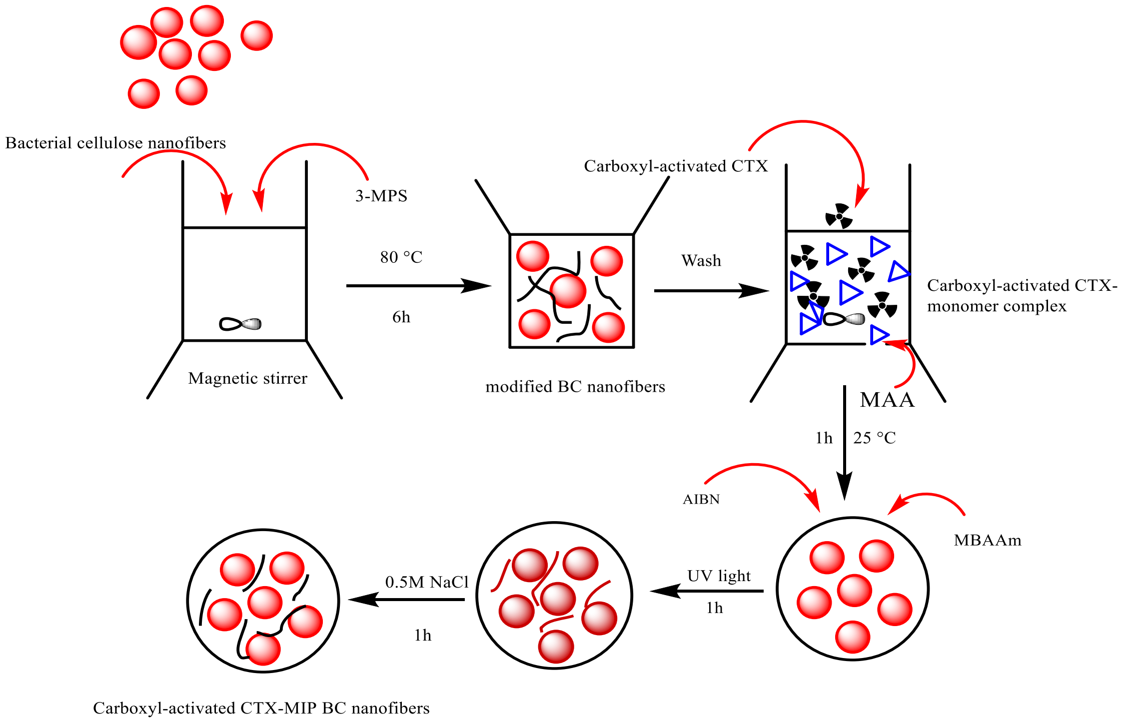

Figure 3.4. Schematic illustration of the carboxyl-activated CTX-MIPs/BC nanofibers' synthesis.

3.2.4. Physicochemical and Morphological Characterization of BC Nanofibers, M-BC nanofibers, NIP, MIP1, MIP2, MIP3.

The following methods were used to characterize BC nanofibers, M-BC nanofibers, NIP, MIP1, MIP2, and MIP3 in terms of their membrane and functional groups, as well as their interactions, morphology, and thermal stability:

Fourier Transform Infrared Spectroscopy (FTIR) spectrum was performed on Thermo Fisher Nicolet IS50 Spectrophotometer (USA); BC Nanofibers, M-BC nanofibers, NIP, MIP1, MIP2, MIP3 were scanned from 400 to 4000 cm^{-1}, with 4 cm^{-1} resolution and 16 scans.

Focused Ion Beam-Scanning Electron Microscope (FIB-SEM GAIA3+Oxford X Xmax 150 EDS, Tescan), operating at 5 to 7 kV FIB-SEM and 50kx and 75kx magnification.

Thermogravimetric analyzer (TGA)/DTG, SDT Q 600, and TA Instruments (USA) were used to record the thermogram of the samples. Over the temperature between 25–800°C, the thermogram was acquired in 10°C/min increments.

Dynamic light scattering (DLS) was utilized to evaluate the size, polydispersity index (PDI), and zeta potential of NPs (Nano-ZS, Malvern Instruments, Malvern, UK). To achieve this, approximately 1 mg of the produced BC nanofibers, MIPs, and NIP were suspended in 1.5 ml PBS. The solutions were then sonicated for 3 hours to form a homogeneous suspension, 200 µl was taken from the result suspension, and 600 µl of ultrapure water was added, followed by the injection of the suspension into the measurement cell. The particles' electrophoretic mobility was then determined. RI and AI were set to 1.59 and 0.010 for the sample, respectively. The dielectric constant has been determined to be 78.5%. Each sample was analyzed in triplicate, and each replicate was measured 12 times to determine the average particle size; the data were analyzed using the mean standard deviation (SD) (n = 3).

3.2.5. A Comparison of the Swelling Index in Media with Different pH

To evaluate swelling index of BC nanofibers, MIPs, and NIP, weighted freeze-dried samples were put in plastic test tubes with caps containing 2 mL of CH_3COOH pH 5.5

and phosphate-buffered saline (PBS) pH 7.4 for 12, 24 hours at 25°C. After collecting samples, the water on the samples' surfaces was eliminated using filter paper. The samples were then weigh up in a wet state.

The swelling ratio for each sample was computed utilizing the following formula:

$$\% \text{ Swelling ratio} = (W_s - W_d)/W_d \times 100\% \qquad (1)$$

where W_s and W_d represent the weights of swollen and dry samples, respectively [143,144].

3.2.6. Loading and In-Vitro Carboxyl-Activated CTX Release Studies.

A stock solution of 3 mg/mL of carboxyl-activated CTX was prepared in the beginning (PBS, pH 7.4). All samples of equal weight and initial thickness were freeze-dried and soaked for 12 hours at 37°C in 2 mL of a carboxyl-activated CTX stock solution. After that, the samples were isolated from the stock and then freeze-dried. Finally, the quantity of loaded prodrug by imprinted and non-imprinted matrices was measured before (B0h) and after loading (A12h) by UV-VIS Spectrophotometer at 296 nm for carboxyl-activated CTX. The amount of the prodrug was determined from the difference between the two measurements.

In-vitro Carboxyl-Activated CTX release tests were carried out in plastic test tubes with caps utilizing buffer solutions (pH 5.5, 6, 7, 7.4, and 8) (2 mL) at 37°C, different temperatures of 25, 37, and 40°C and different concentrations of (0.5, 1, 2, 3, and 4 mg/mL) while the tubes were shaking at a rate of 120 rpm. Aliquots of 0.6 mL of the release medium were withdrawn at predetermined periods: 0.5, 1, 2, 4, 6, 8, and 36 hours, and then replaced with the same volumes of release medium to maintain the tube's condition. For carboxyl-activated CTX, measurements of prodrug release at a wavelength of 296 nm using a UV-VIS spectrophotometer (Shimadzu UVmini-1240, Tokyo, Japan) were determined, and the total release values were calculated. The results were described as cumulative drug release (%) as a function of time.

3.2.7. In-Vitro Release in Plasma

After incubating MIP1, MIP2, MIP3, and NIP-carboxyl-activated CTX in artificial plasma at 37°C for 72 hours, the amount of released carboxyl-activated CTX was measured with a UV-VIS spectroscopy at selected time points.

4. RESULT AND DISCUSSION

4.1. Characterization of Carboxyl-Activated CTX

4.1.1. UV-VIS Spectrophotometry

The formation of carboxyl-activated CTX has been diagnosed depending on the UV-VIS spectrum observed in (Figure 4.1), which showed absorption at UV (λmax (nm))= 296. It's not shown absorption like absorption of CTX that shows absorption usually at UV (λmax (nm))= 231 [140], and it's shown the formation of a new product.

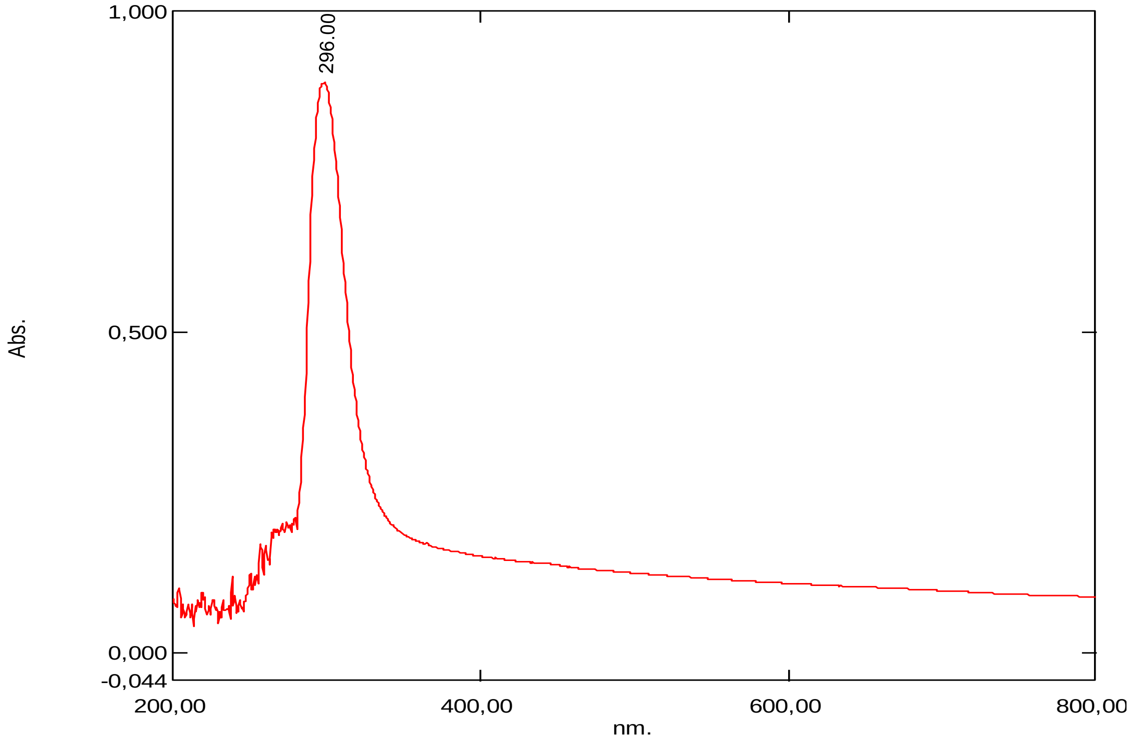

Figure 4.1. The UV-VIS absorption spectrum of Carboxyl-activated CTX.

4.1.2. Fourier Transform-Infrared Spectroscopy (FTIR)

As for the FTIR spectrum (KBr) observed in (Figure 4.2) Esterification was confirmed by the (C=O), (C-O) stretching vibrations observed at 1720.84, 1231 cm^{-1}, respectively, a band observed at approximately 3421.08 cm^{-1} refer to (O-H) stretching vibrations, a band at 3010 cm^{-1} are assigned to (C-H) aromatic stretching vibrations, The presence of (C-H) aliphatic was indicated by the band at 2957-2856 cm^{-1}, whereas the presence of

(C=C) aromatic was designated by the band at 1608.43-1587 cm^{-1}, a band at 1411 cm^{-1} corresponds (C-O-H). A band at 1094 cm^{-1} indicated the presence of (C-O-C). The band at 869-723 cm^{-1} relates to the (Ar-H) aromatic group. It's believed that the conduct of the interaction of the preparation of carboxyl-activated CTX according to the mechanism proposed [99] in (Figure 4.3)

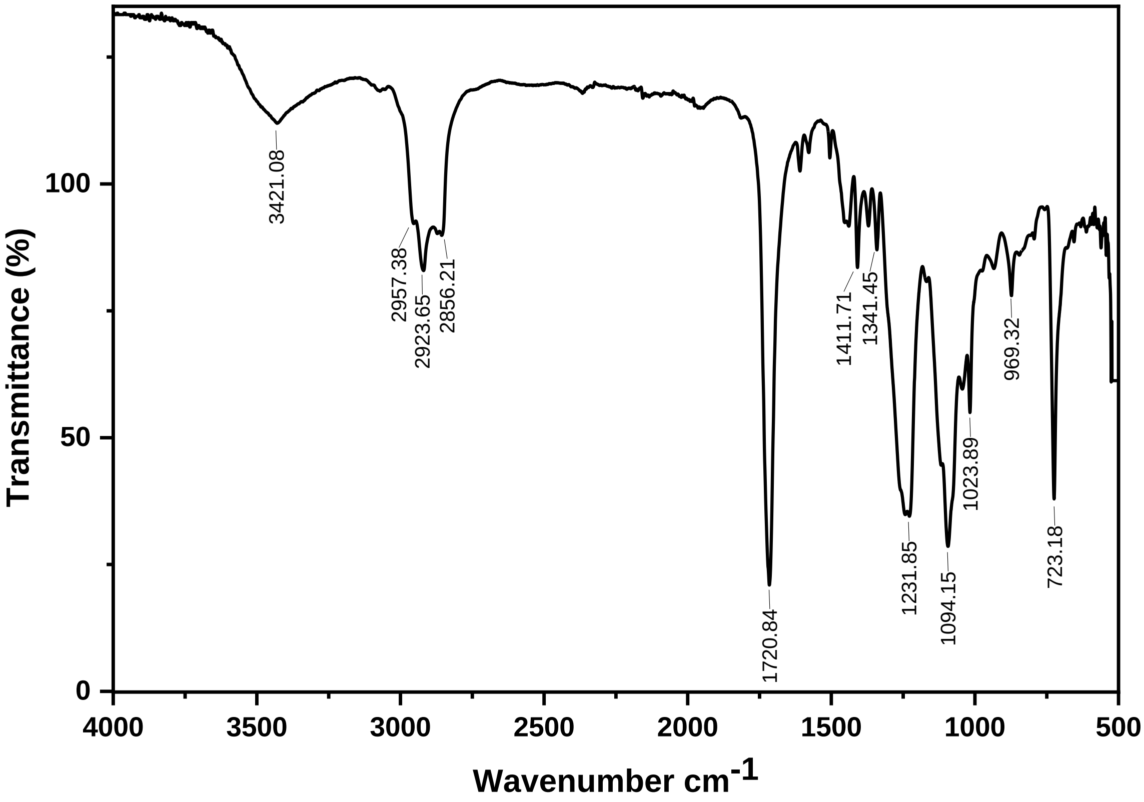

Figure 4.2. FTIR analysis of carboxyl-activated CTX.

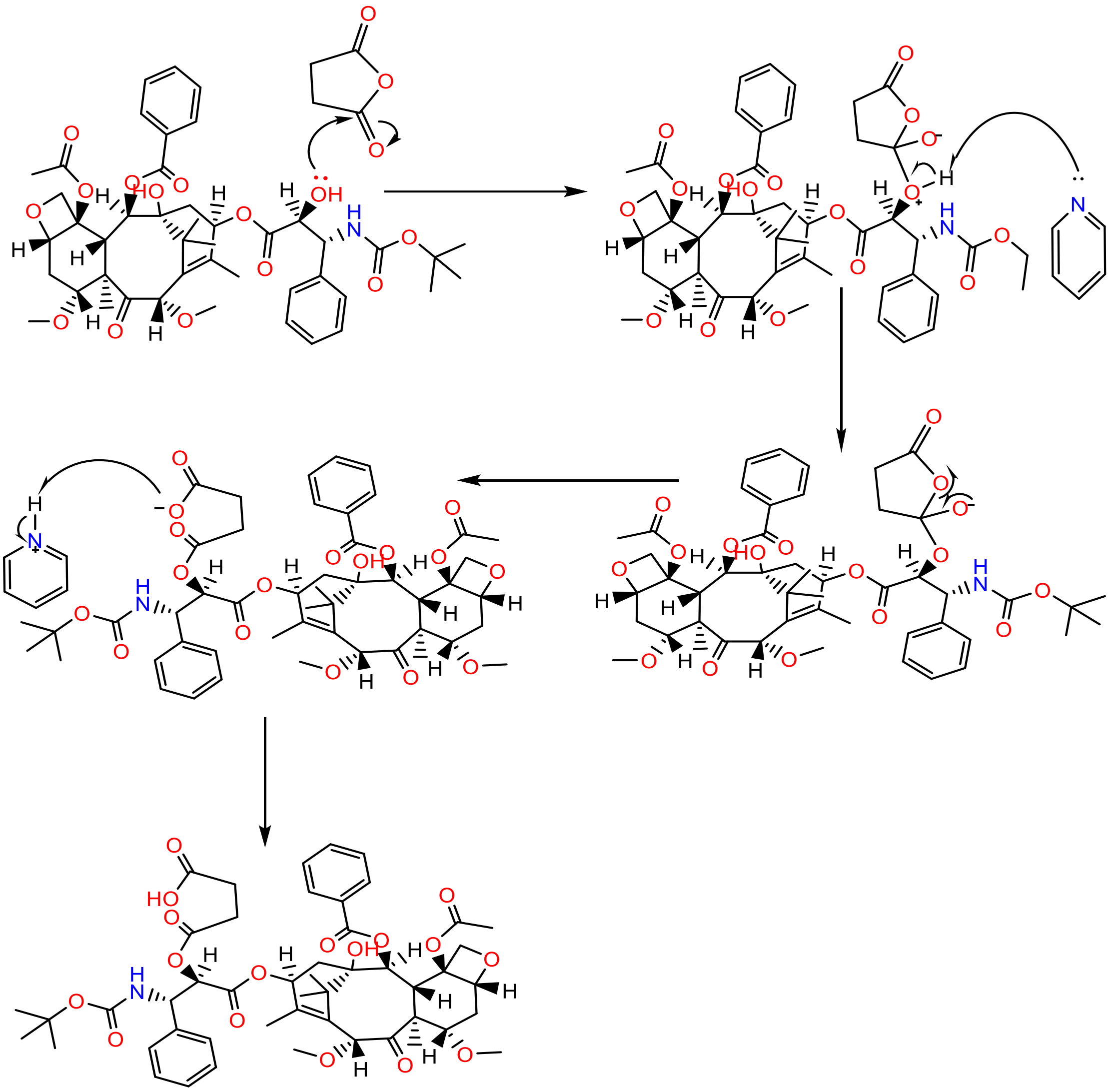

Figure 4.3. The mechanism proposed for the preparation of carboxyl-activated CTX.

4.1.3. Proton Nuclear Magnetic Resonance ^{1}HNMR

^{1}H NMR confirmed the chemical structure of succinic anhydride-cabazitaxel conjugate (Figure 4.4). ^{1}H-NMR was used to characterize the spectra of succinic anhydride-cabazitaxel conjugate (CDCl3). The peak at 5.37 ppm indicated that succinic anhydride was successfully conjugated to CTX via an ester bond. The -CH_2-CH_2- bonds in the carboxyl-activated CTX were represented by a second peak between 2.71 and 2.61 ppm**.**

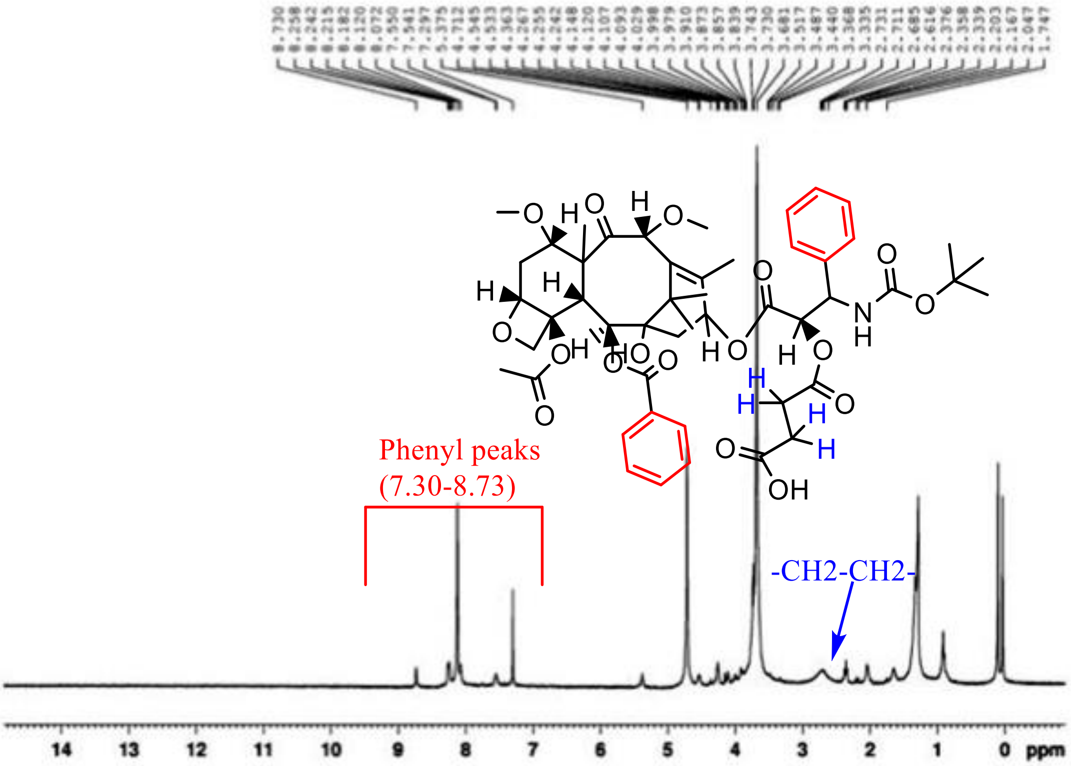

Figure 4.4. H-NMR analysis of carboxyl-activated CTX.

^{1}H NMR (200 MHz, CDCl3): δ8.12 (d, 2H), 7.550 (t, 1H), 7.54 (t, 2H), 7.29 (d, 3H), 5.37 (s, 1H), 4.71 (s, 1H), 4.36 (d, 1H), 4.14 (d, 1H), 3.87 (dd, 1H), 3.83 (s, 1H), 3.44 (s, 3H), 3.33 (s, 3H), 2.73–2.61 (m, 4H), 2.37 (s, 3H), 2.33 (s, 1H), 2.20 (s, 2H), 2.04 (s, 1H) 1.97 (s, 3H), 1.82–1.75 (m, 1H), 1.74 (s, 3H), 1.33 (s, 9H), 1.28 (s, 1H), 1.17 (s, 6H).

4.2. Preparation of MIPs-BC/NIP-BC Nanofibers Composites

MIPs composites were produced by reactively filling the pores of bacterial cellulose membranes with MIPs containing carboxyl-activated CTX recognition sites. To obtain a second anchor for the MIPs, in-situ graft polymerization of MAA functional monomer with MBAAm as a cross-linker in carboxyl-activated CTX was used to produce thin-layer MIPs. This process was carried out in the presence of a carboxyl-activated CTX (as a template molecule). At first, functional monomers in solution interact with target molecules to form a pre-polymerization complex (carboxyl-activated CTX-MAA). After this step, in the presence of MBAAm and AIBN, the carboxyl-activated CTX-MAA complex was combined with M-BC nanofibers. Next step was the subsequent extraction of the template molecule (Figure 4.5). Methacrylic acid was selected as the functional monomer due to its (COOH) group. It can produce weak electrostatic attractions and/or function as an H-donor for H-bond acceptor drugs. Both properties contributed to MAA's selection as the functional monomer. The crosslinker MBAAm was chosen for the MIPs synthesis because of the expected rigidity and denseness it might confer. NIP was prepared following the procedure mentioned above without carboxyl-activated CTX.

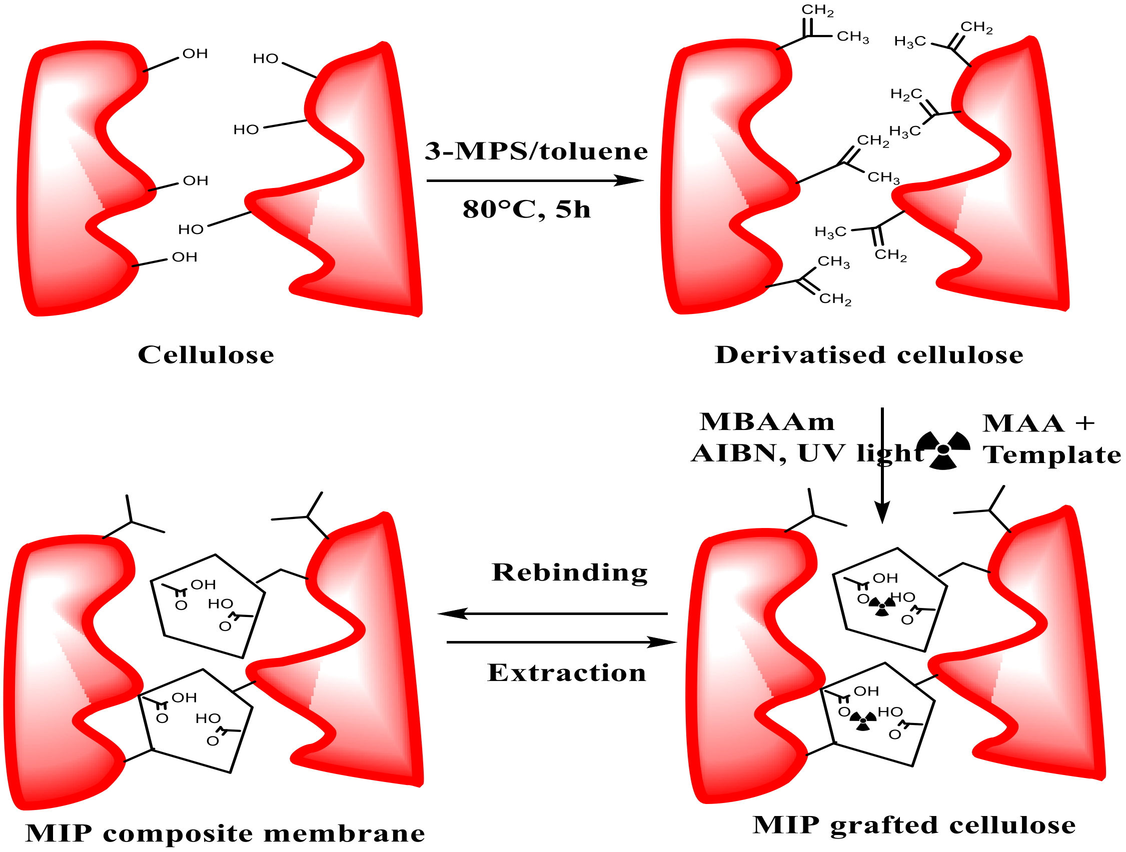

Figure 4.5. Schematic illustration of MIPs-BC nanofibers composites.

4.2.1. Characterization of Pre-Polymerization Complex

The formation of carboxyl-activated CTX-MAA has been diagnosed depending on the UV spectrum observes in (Figure 4.6-8) which showed absorption at UV (λmax (nm)) = 301,294, and 295 for a pre-polymerization complex (12.5,25,50 mg) of the prodrug, respectively. and It's don't show absorption like absorption of a prodrug that shows absorption usually at UV (λmax (nm)) = 296 (due to π-π transition of MAA) and it's shown the formation of new products.

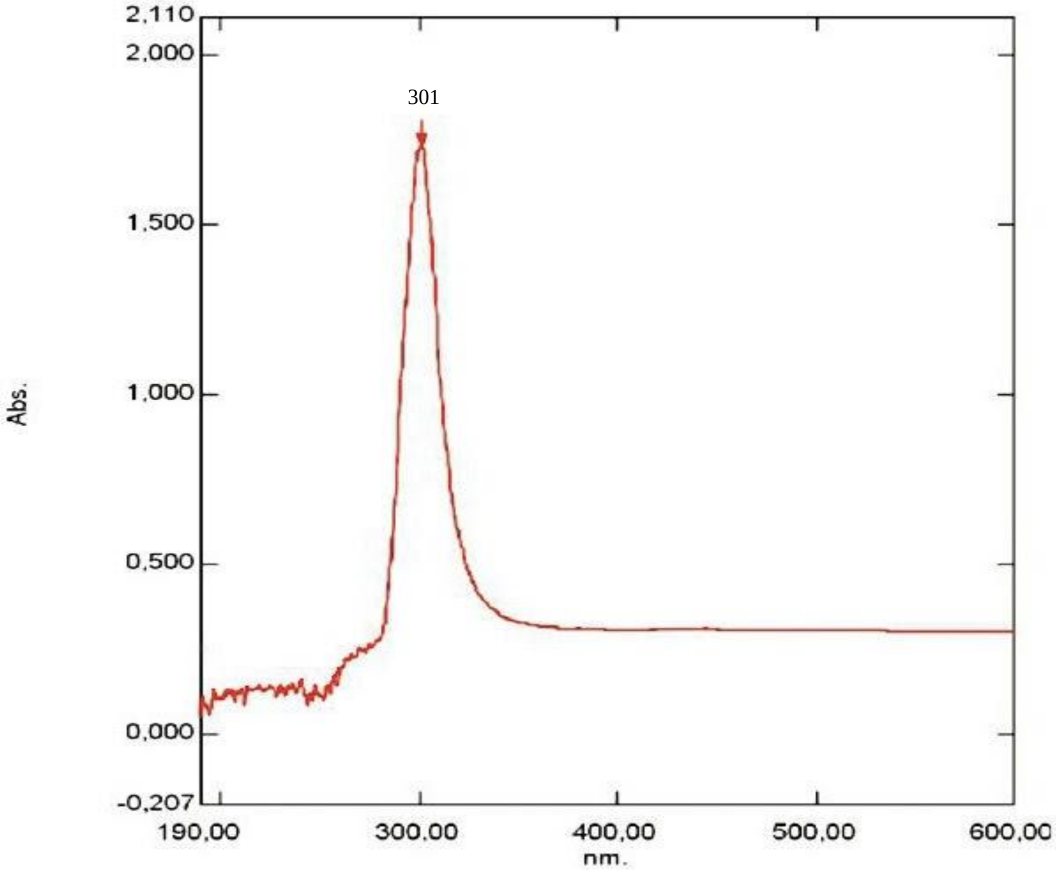

Figure 4.6. The UV-VIS spectrum of a pre-polymerization complex: Carboxyl-activated CTX (12.5, mg) and (430 mg) MAA.

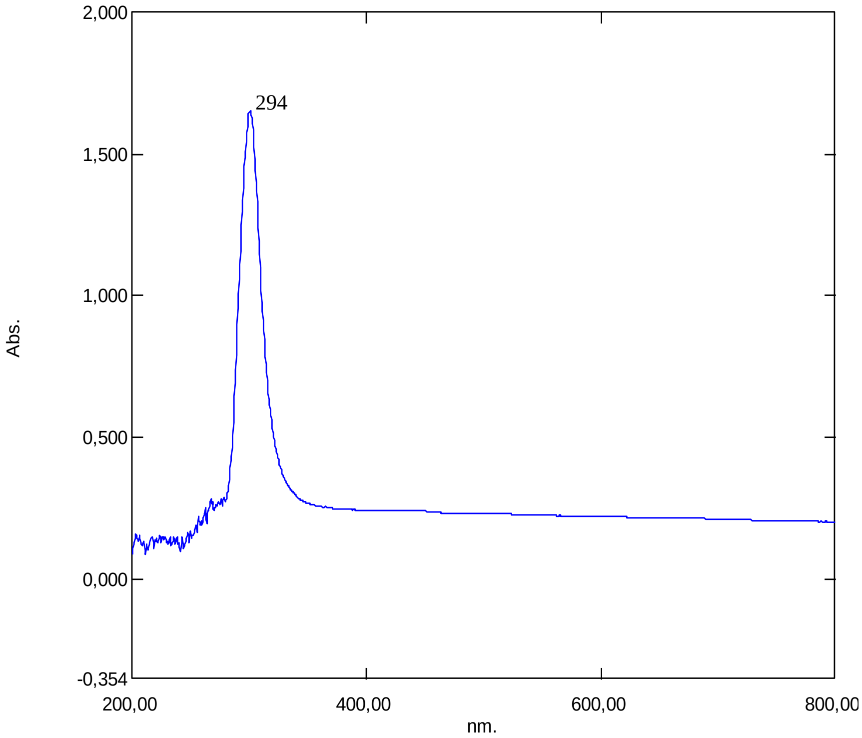

Figure 4.7. The UV-VIS spectrum of a pre-polymerization complex: Carboxyl-activated CTX (25 mg) and (860 mg) MAA.

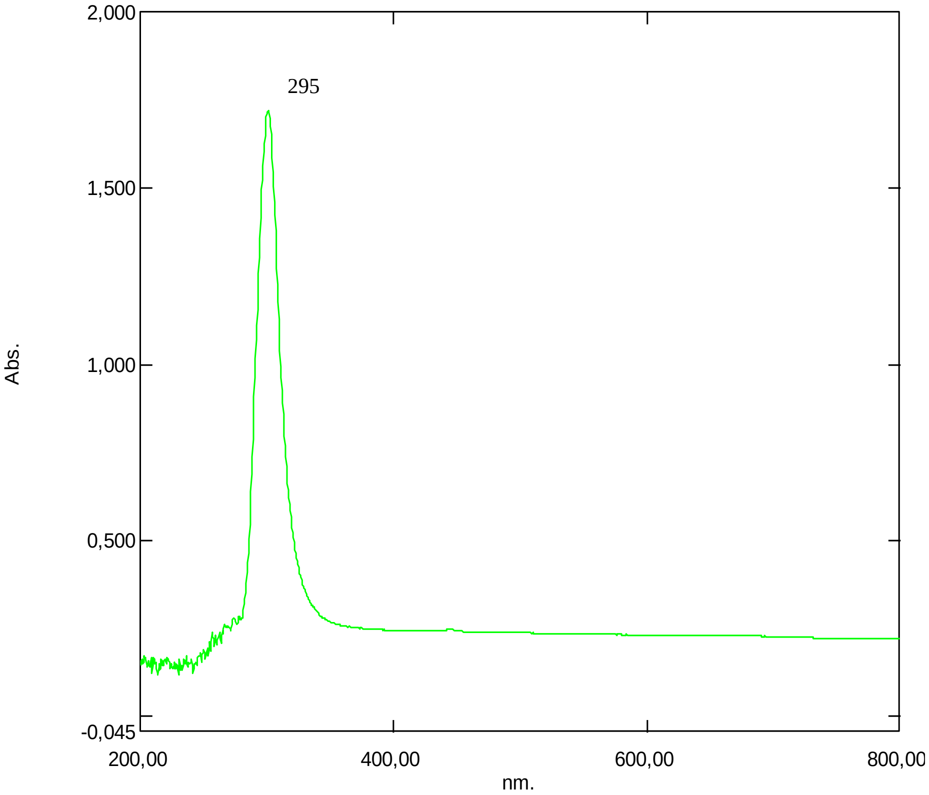

Figure 4.8. The UV-VIS spectrum of a pre-polymerization complex: Carboxyl-activated CTX (50 mg) and (1720 mg) MAA.

4.2.2. Characterization of BC nanofibers, M-BC nanofibers, NIP, MIP1, MIP2, MIP3

4.2.2.1. Fourier Transformed Infrared spectroscopy (FTIR)

(Figure 4.9-15) depicts the FTIR spectra of BC nanofibers, M-BC nanofibers, MIPs, and NIP. The characteristic bands of BC nanofibers were identified in approximately 3343-3355 cm^{-1} and 1100 cm^{-1}, which correspond to (OH) stretching vibrations, which are engaged in intramolecular and intermolecular hydrogen bonds, and (C-H) aliphatic stretching vibrations, respectively [145,146]. Due to the incorporation of MIPs and NIP into the BC nanofiber, the intensity of the (OH) stretching band in BC nanofibers increased, while the intensity of the (C-H) stretching band decreased. This was due to the sharpening of the band of (O-H) stretching in BC nanofibers. Changes in the bands indicate the formation of MIPs and NIP in the matrix of BC nanofibers. Bands at 2800-2900 cm^{-1} correspond to (-CH_2), (-CH_3) sp3 carbon asymmetric stretching vibrations, respectively [147,148]. The absorption band at 1620-1640cm^{-1} corresponds to carbonyl groups (C=O) [149] of the composite nanofibers, indicating that the MIPs and NIP were fabricated onto the BC nanofibers.

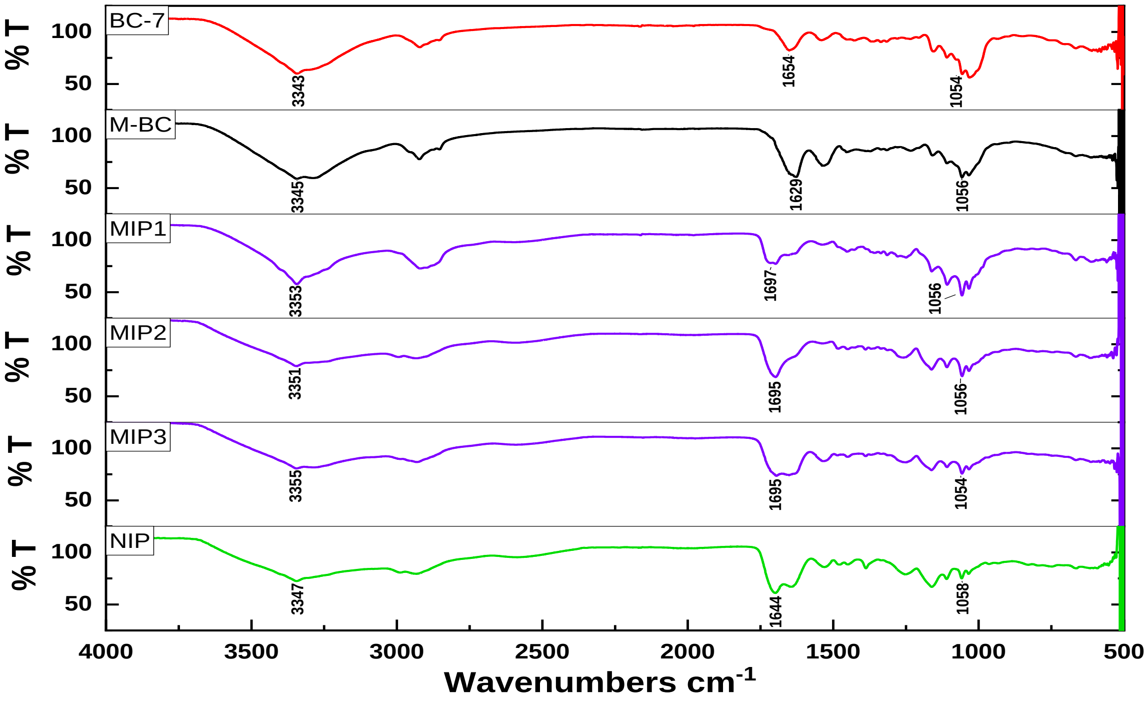

Figure 4.9. FTIR analysis of BC nanofibers, M-BC nanofibers, NIP, MIP1, MIP2, MIP3.

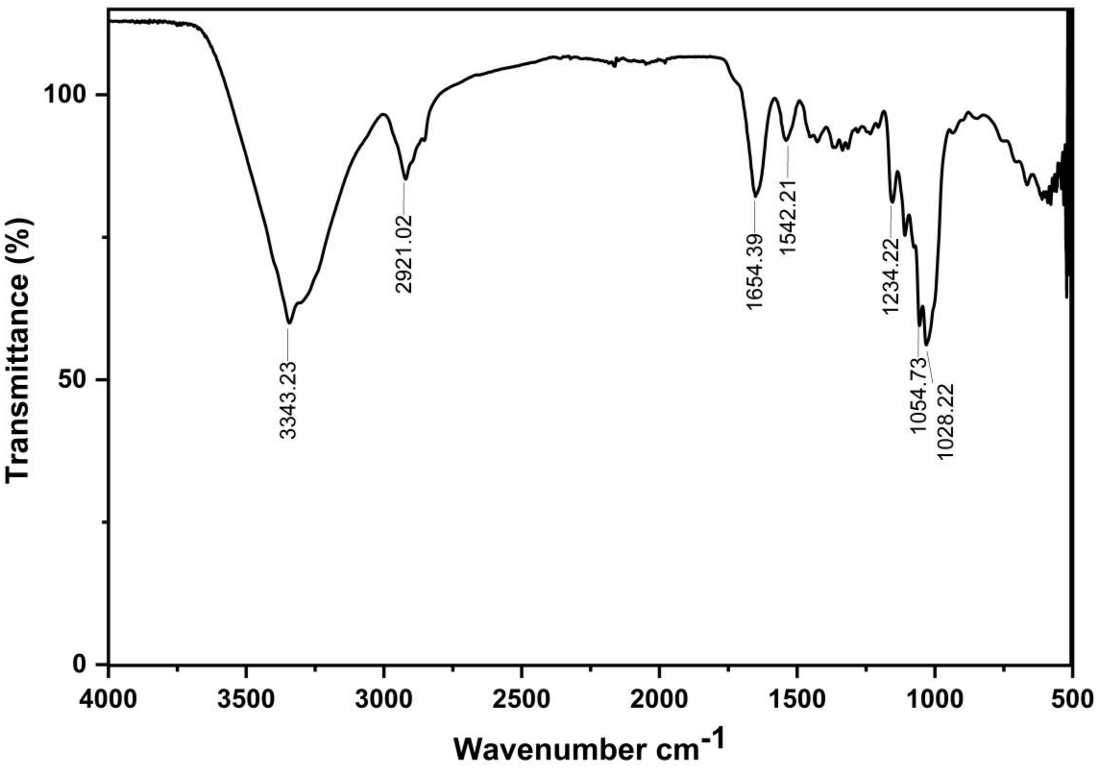

Figure 4.10. FTIR analysis of BC nanofibers.

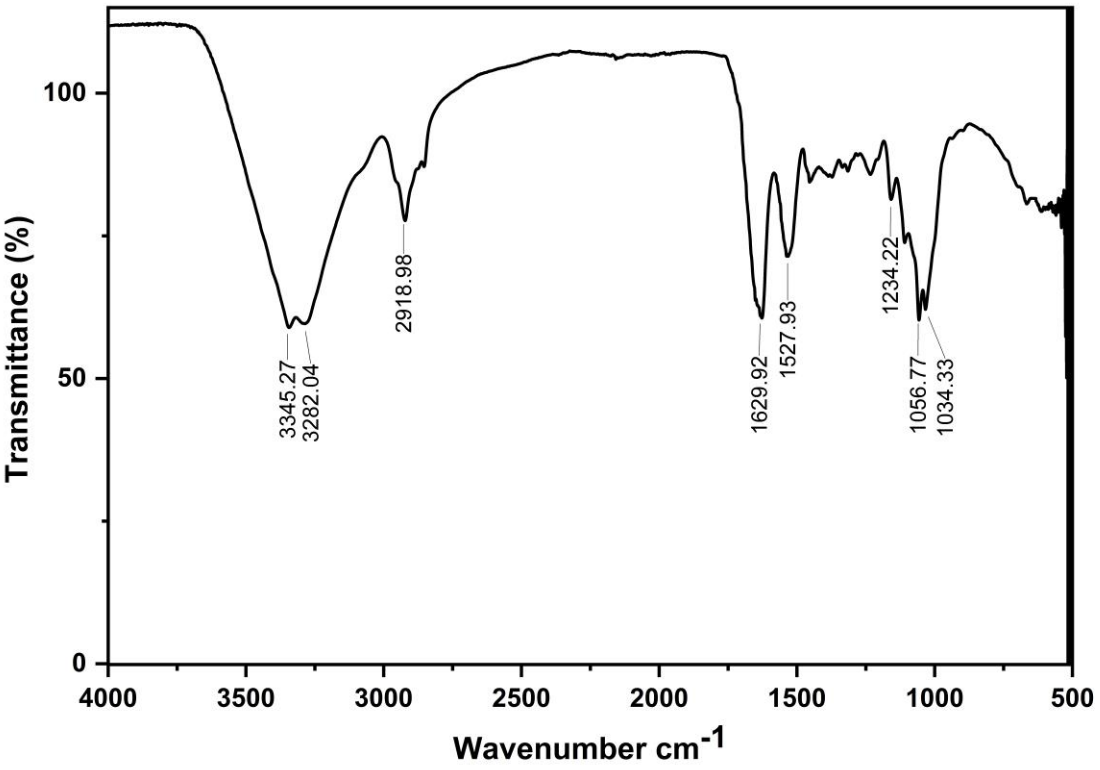

Figure 4.11. FTIR analysis of M-BC nanofibers.

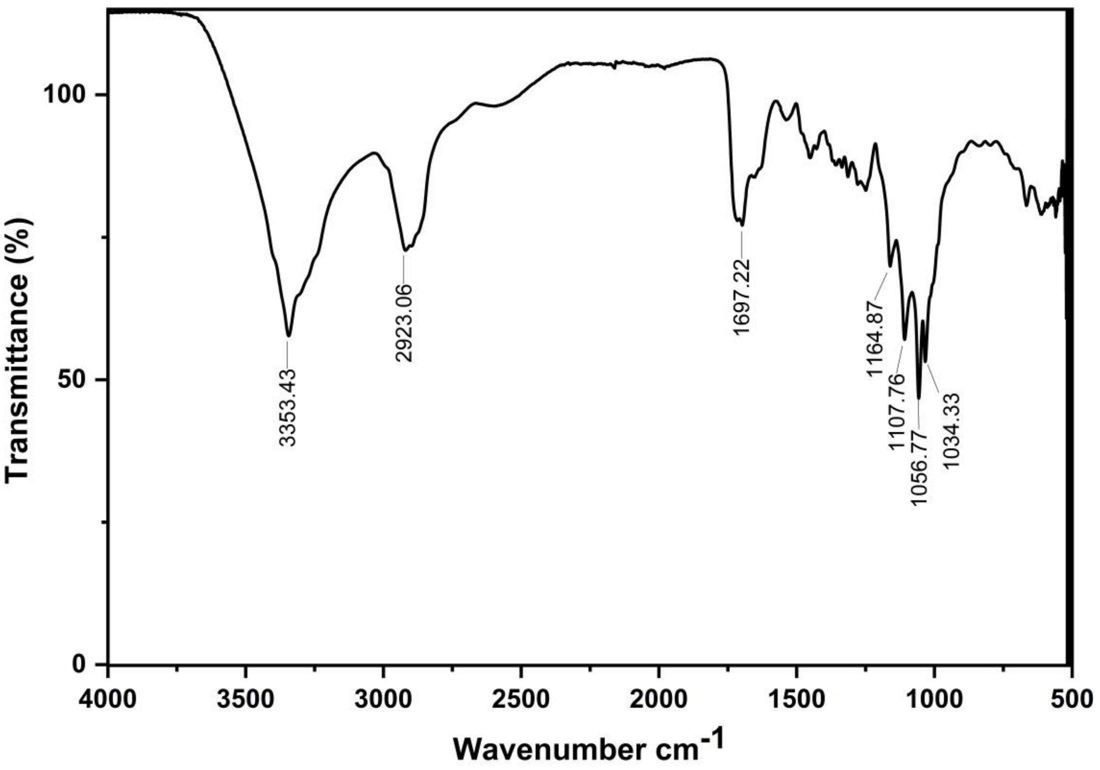

Figure 4.12. FTIR analysis of MIP1.

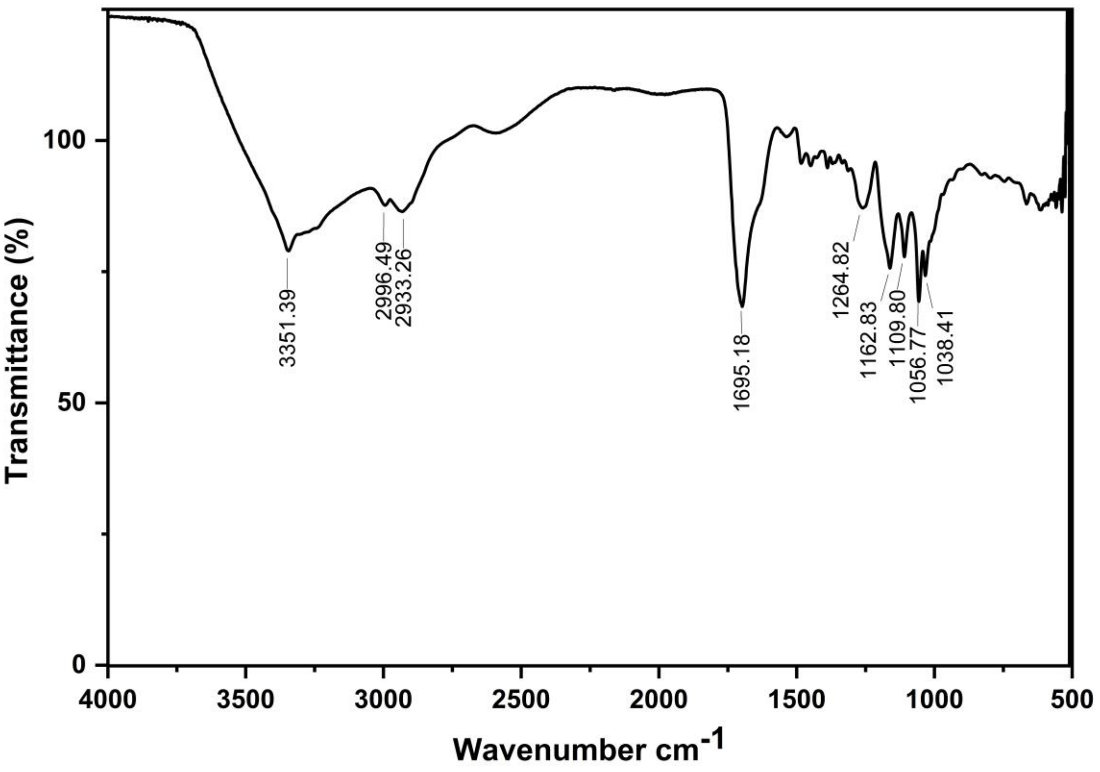

Figure 4.13. FTIR analysis of MIP2.

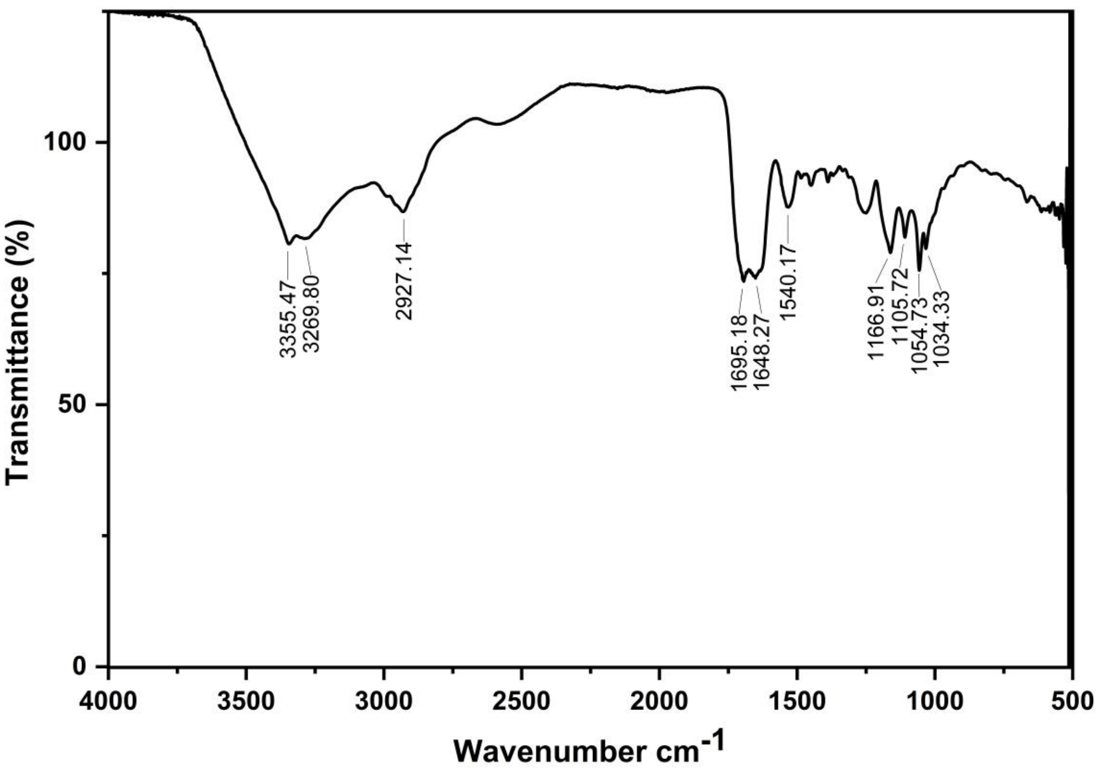

Figure 4.14. FTIR analysis of MIP3.

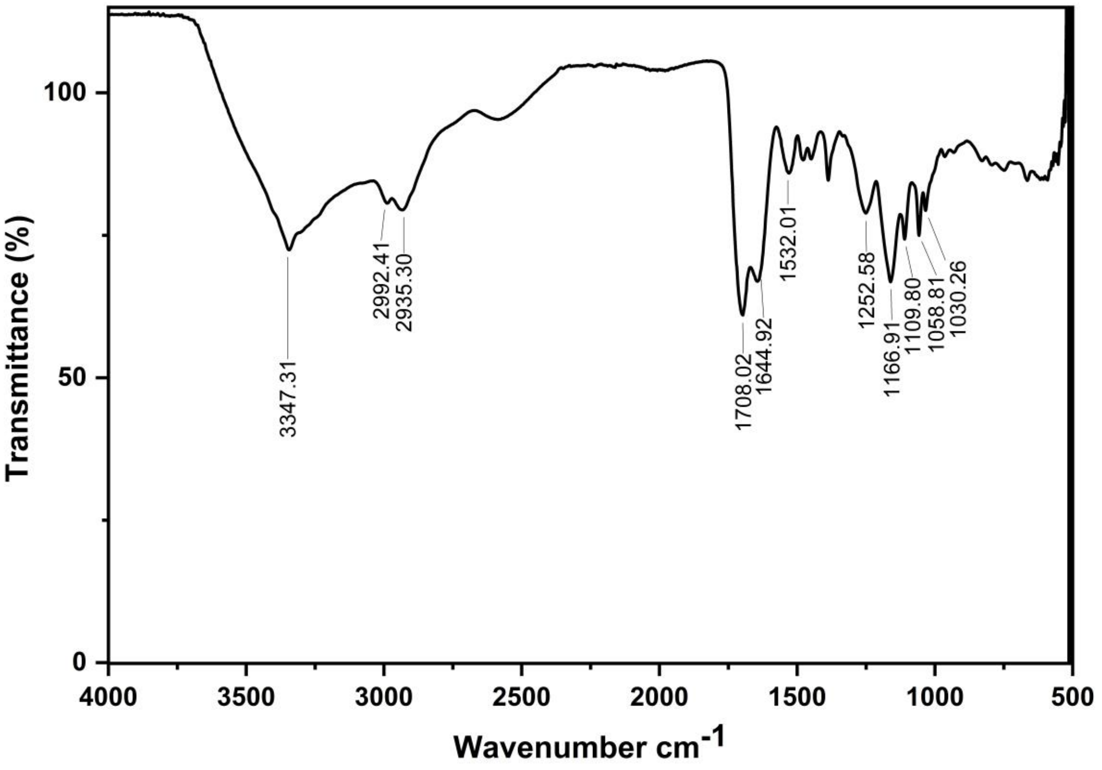

Figure 4.15. FTIR analysis of NIP.

Finally, absorption bands corresponding to (C-O-C) and (C-O) stretching vibrations bonds in polysaccharides are observed at 1300–1400 cm^{-1} and 1040–1068 cm^{-1} [150]. The BC nanofibers spectra attributed bands at 797 cm^{-1} and 712 cm-1 to cellulose Iα and Iβ, respectively [151]. In conclusion, each band identified by FT-IR analysis for BC nanofibers is distinct for BC nanofibers, and the obtained results are consistent with those described in the scientific literature.

4.2.2.2. Focused Ion Beam-Scanning Electron Microscopy (FIB-SEM) Analysis

Representative SEM (Figure 4.16-19) images were employed to observe the morphological features of BC nanofibers, M-BC nanofibers, MIPs, and NIP. A homogeneous three-dimensional network and porous structure were observed. The bacterial cellulose membranes (nanofibrils) were randomly arranged in all the samples and displayed the standard nanofibril structure. BC nanofibers are an effective alternative that has the potential to act as a support biomaterial for a wide range of different biomedical applications, including drug-delivery systems [25]. It was conclusively demonstrated that MIPs and NIP could be produced on the surface of M-BC by in-situ polymerization [152]. The resulting MIPs and NIP had diameters of 42-59 nm, 31–38 nm, 45–49 nm, and 143–166 nm, respectively. These results are close to the previous studies. SEM results demonstrated that BC nanofibers produced from *Komagataeibacter intermedius* strain are similar to cellulose in morphology.

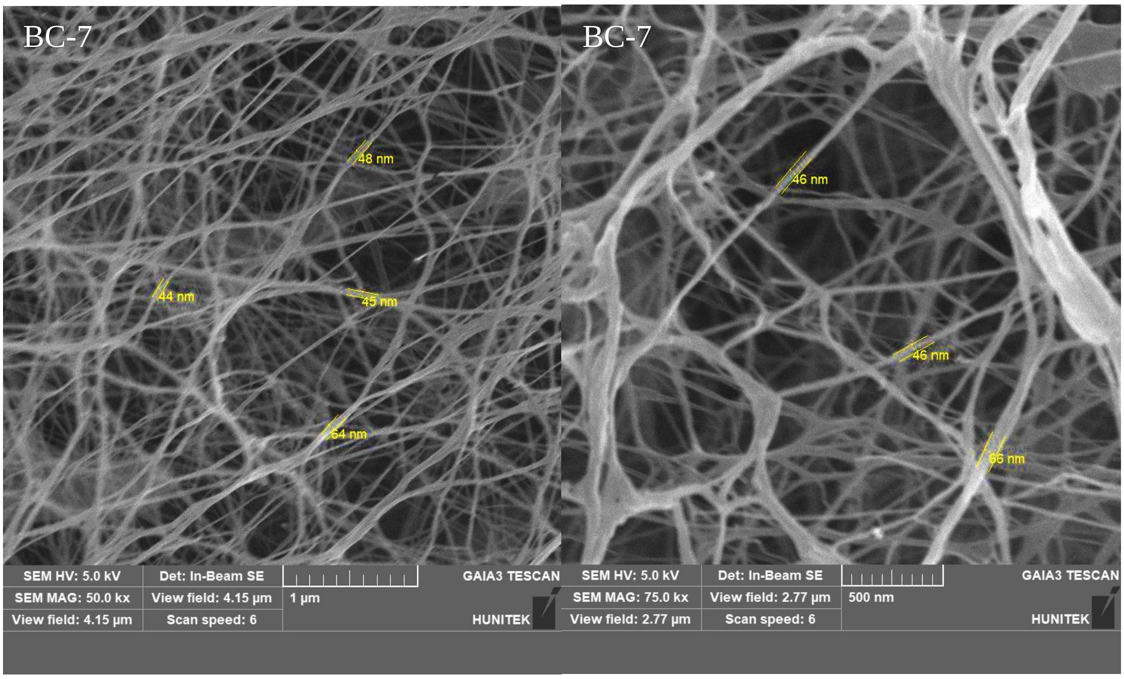

Figure 4.16. FIB-SEM images of BC nanofibers -7.

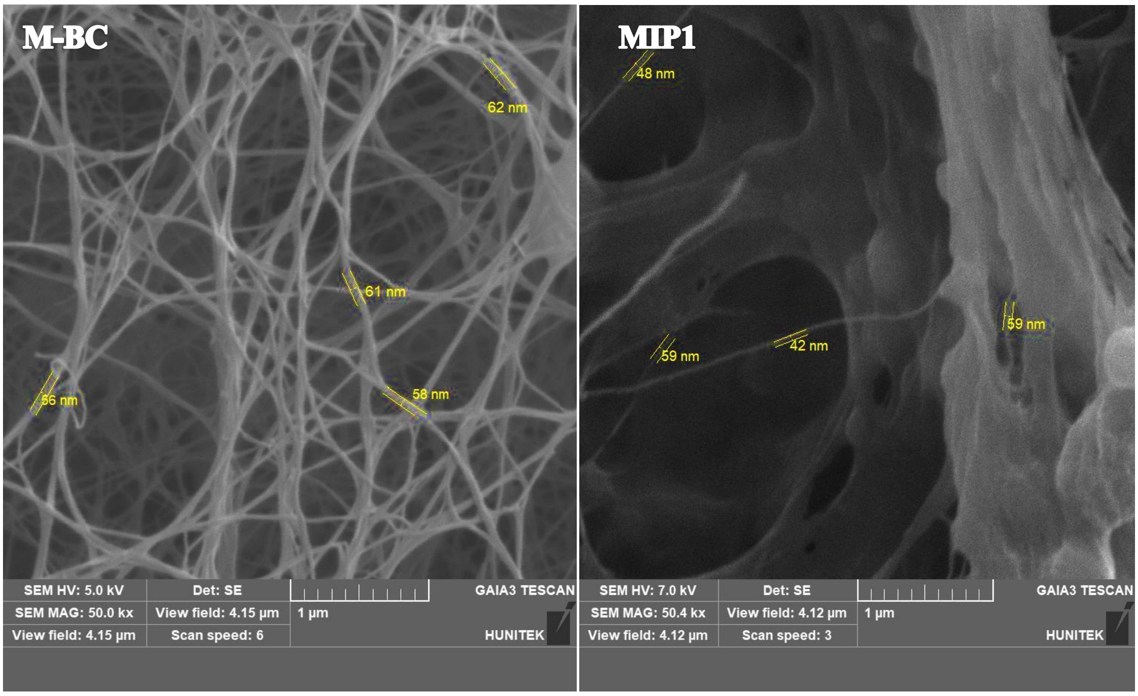

Figure 4.17. FIB-SEM images of M-BC nanofibers and MIP1.

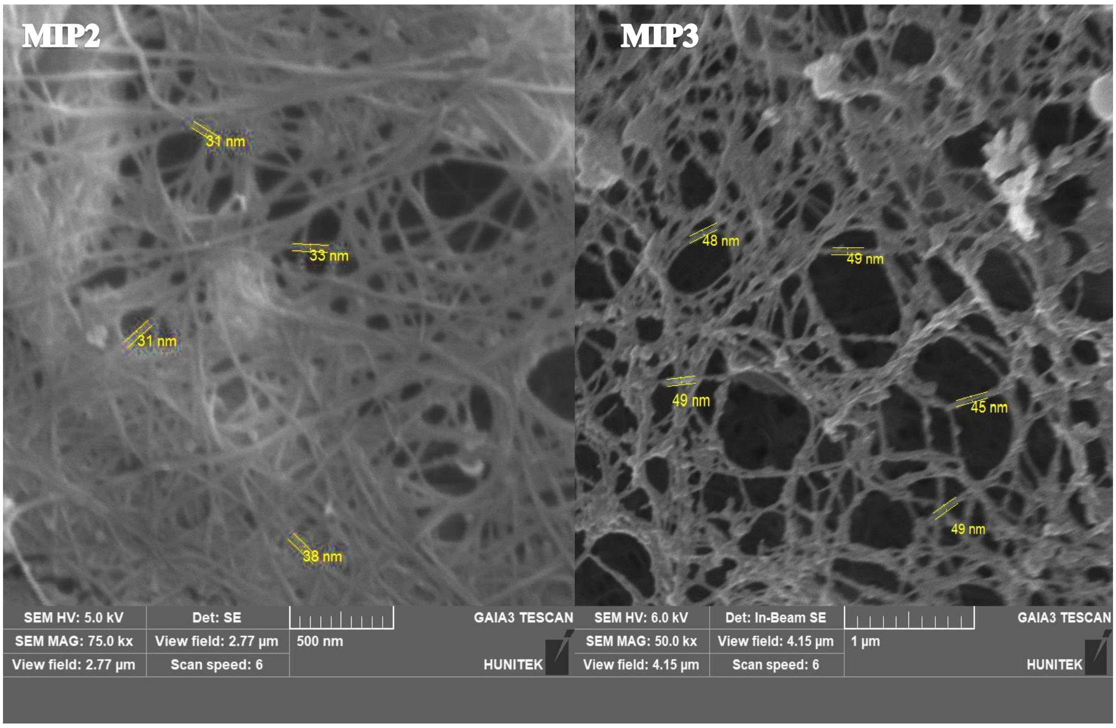

Figure 4.18. FIB-SEM images of MIP2, and MIP3.

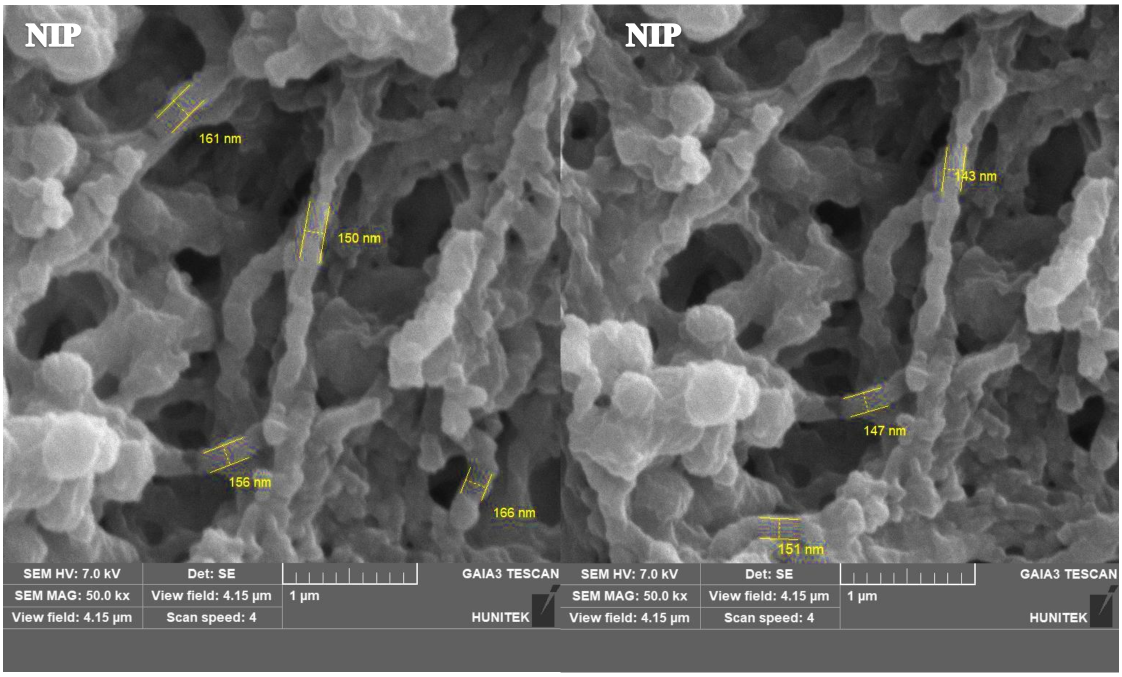

Figure 4.19. FIB-SEM images of NIP.

4.2.2.3. Thermogravimetric Analysis (TGA)/DTG

The thermal gravimetric analysis (TGA)/ derivative thermograms (DTG) for BC, M-BC, MIPs, and NIP are shown in (Figure 4.20). The thermogravimetric and thermogravimetric derivative curves of BC revealed three major thermal events. The first event happened at approximately 30°C–240°C (6.49% weight loss) and was caused by a small amount of moisture. The second event, considered to be a rapid loss in weight within a small temperature range, began at approximately 240°C-340°C (55.12% weight loss) and was correlated to cellulose degradation (depolymerization, dehydration, decomposition of glucose linkages, reorganization, and formation of carbonyl and carboxyl groups) [153–155]. Maximum weight loss is observed at 320°C. The third event, which continued between 360°C-800°C (11.62%), was associated with the oxidation and decomposition of carbonaceous residues [156,157].

On the one hand, surface-modified BC (Figure 4.21.b) lost approximately 6.71% of its weight at 30°C-250°C because of evaporation of adsorbed water, followed by a continuing loss of dry matter at 220°C-350°C. This accounts for 55.62 % of the total weight loss, indicating that acetylation has indicating modifications in surface properties. Similarly, weight loss of 19.01% was observed at 350°C–650°C.

On the other hand, (Figure 4.21.c, d,e, and f) demonstrates that the first slight weight loss up to 275, 220, 200, and 100°C to MIP1, MIP2, MIP3, and NIP, respectively, is attributed to the physical desorption of surface-adsorbed water. The second event of rapid weight loss occurs at the temperature between 275-400°C, 220-355°C, 200-340 °C, and 100-345°C, respectively. In contrast, the DTG peak was 329°C, 398°C for MIP1, 325°C, 385°C for MIP2, 308°C, 400°C for MIP3, and 320°C, 396°C for NIP, which originated from the loss of the polymer layer [158]. Together, the third event of weight loss occurs at temperature between 400-575°C, 355-580°C, 340-520°C, and 345-500°C, respectively, which are associated with the de- polymerization of cellulose and the decomposition of glucose units [159]. The total mass loss of MIP1, MIP2, MIP3, and NIP were approximately 54.30%, 57.70%, 64.29%, and 57.42%, respectively.

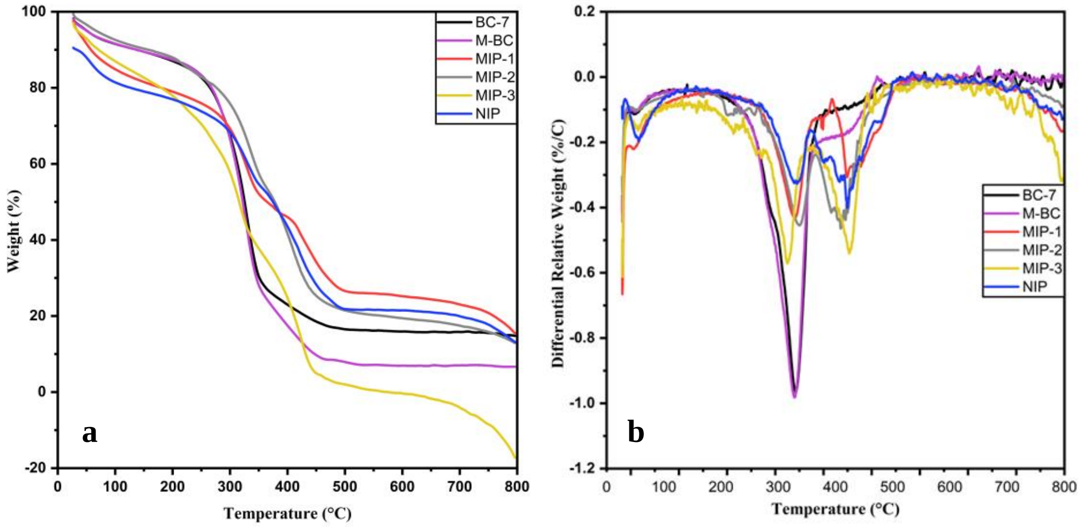

Figure 4.20. a: TGA/b: DTG curve of BC, M-BC, MIPs, and NIP.

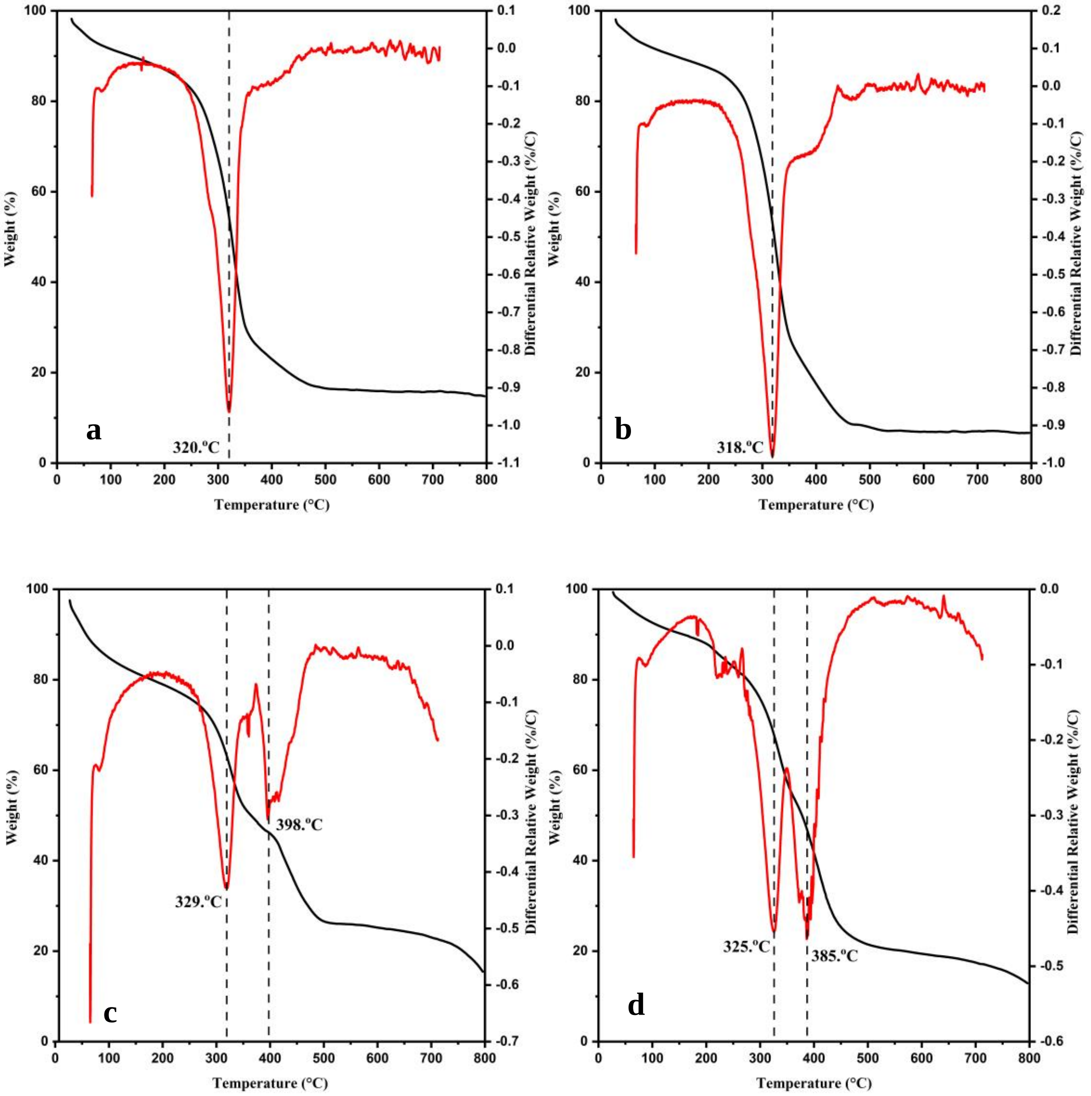

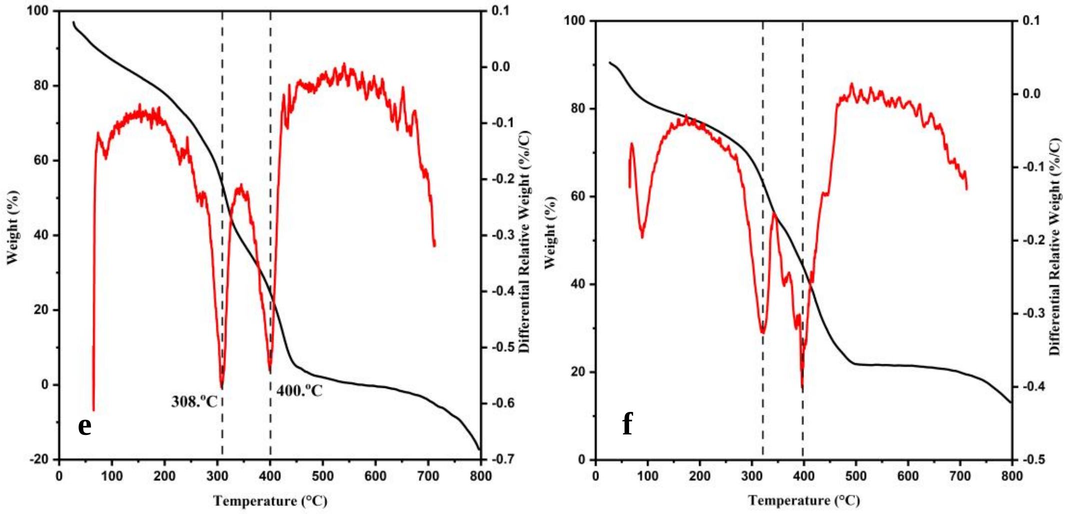

Figure 4.21. a: TGA/DTG curve of BC, b: TGA/ DTG curve of M-BC, c: TGA/ DTG curve of MIP1, d: TGA/ DTG curve of MIP2, e: TGA/ DTG curve of MIP3, f: TGA/ DTG curve of NIP.

4.2.2.4. DLS Analysis Dynamic

Hydrodynamic particle size (diameter), polydispersity index (PDI), and zeta potential of BC nanofibers, MIPs, and NIP were measured with a Zetasizer (Figure 4.22-33). The results are presented in (Table 4.1.) as the mean (n=3). The BC nanofibers displayed a size distribution with an average hydrodynamic diameter of 79.08±10.70 nm (PDI = 0.55±0.16), which implied that, in the ultrasonic hydrolysis of BC nanofibers, it was easy to obtain fiber of small size. The size of membranes increased when adding the drug carboxyl-activated CTX (Table 4.1.).

Zeta potential measurement permits the prediction of the storage stability of colloidal particles, as charged particles will exhibit less particle aggregation. For the prepared BC nanofibers, M-BC nanofibers, MIPs, and NIP, the Zeta potential (mV) were tabulated in (Table 4.1.). The value of zeta potential of BC nanofibers, M-BC nanofibers, MIPs1,2,3, and NIP were -22.7±2.12, -14.2±1.80, -23.00±0.52, -18.76±1.88, -17.40±0.96, -22.83±3.06 mV respectively. According to the known electronegativity of cellulose, the zeta potential showed a tendency toward more negative values, which suggests that mechanical disruption has caused an increase in negatively charged fragments (the sonication of cells) [160], which can be accounted for by the dissolution of numerous hydrogen bonds and the formation of fresh nano-cellulosic fragments with more free negative potential. It was common for stabilized nanoparticles to have a zeta potential scale of -15 to -30 mV [161].

Table 4.1. Particle size, Poydispersity index, and Zeta potential of BC nanofibers, M-BC nanofibers, MIPs, and NIP formulations (mean ± SD, n=3).

Formulation code	No	Size (nm)	St Dev (nm)	PDI	Zeta potential (mV)	Mean size (n=3)	Mean PDI (n=3)	Mean Zeta potential (n=3)
BC	1	68.15	0.98	0.75	-20.80	79.08±10.70	0.55±0.16	-22.7±2.12
	2	79.55	1.24	0.44	-22.30			
	3	89.54	3.20	0.47	-25.00			
M-BC	1	146.40	8.68	0.23	-12.40	105.38±36.81	0.34±0.15	-14.2±1.80
	2	94.55	9.40	0.27	-14.20			
	3	75.19	4.80	0.52	-16.00			
MIP1	1	150.50	14.20	0.31	-23.20	131.80±16.21	0.43±0.10	-23.00±0.52
	2	121.60	15.34	0.49	-22.40			
	3	123.30	14.00	0.50	-23.40			
MIP2	1	113.80	13.86	0.29	-20.40	106.6±6.17	0.38±0.07	-18.76±1.88
	2	103.00	14.00	0.44	-16.70			
	3	103.20	12.13	0.41	-19.20			
MIP3	1	172.10	3.40	0.27	-18.10	142.32±43.20	0.26±0.01	-17.40±0.96
	2	162.10	0.93	0.25	-17.80			
	3	92.77	3.32	0.27	-16.30			
NIP	1	164.50	9.20	0.30	-19.40	140.86±20.46	0.35±0.04	-22.83±3.06
	2	129.00	8.58	0.38	-23.80			
	3	129.10	6.31	0.39	-25.30			

Since most cellular membranes have a negative charge, which would favor stability for intravenous injection, Zeta potential can affect a nanoparticle's propensity to penetrate membranes, with cationic nanoparticles typically exhibiting more significant toxicity related to cell wall disruption [162]. Negative zeta potentials were significant for efficient cancer treatment and may reduce systemic toxicity [163]. To treat prostate cancer, Yan et al. developed nanoparticles with a negative charge that were co-loaded with docetaxel and curcumin [164].

They disputed that the negative surface charge of NPs could reduce the risk of systematic toxicity and was significant for successful cancer treatment. Additionally, If the material is negatively charged, the material will be repellent to the bacteria [165]. This confirms the purity of the bacterial cellulose produced in this study.

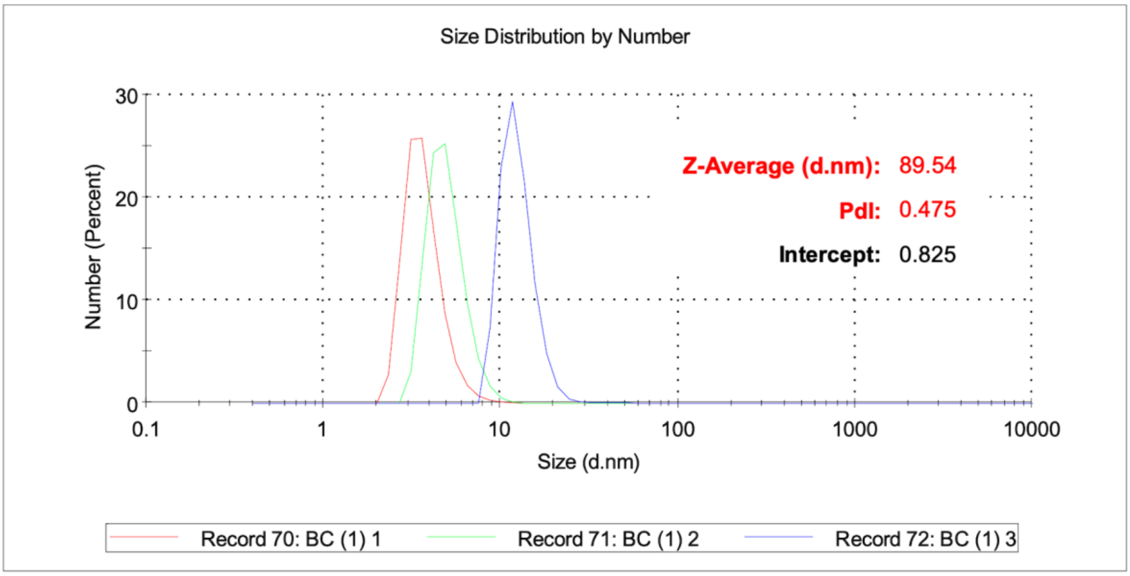

Figure 4.22. The hydrodynamic particle size and polydispersity index (PDI) for BC.

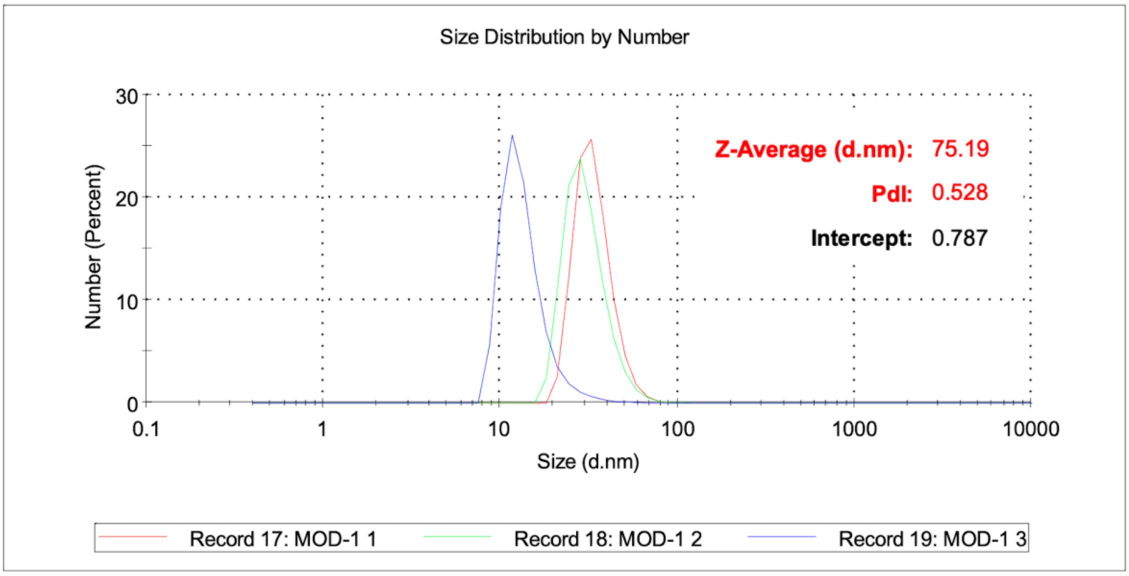

Figure 4.23. The hydrodynamic particle size and polydispersity index (PDI) for M-BC.

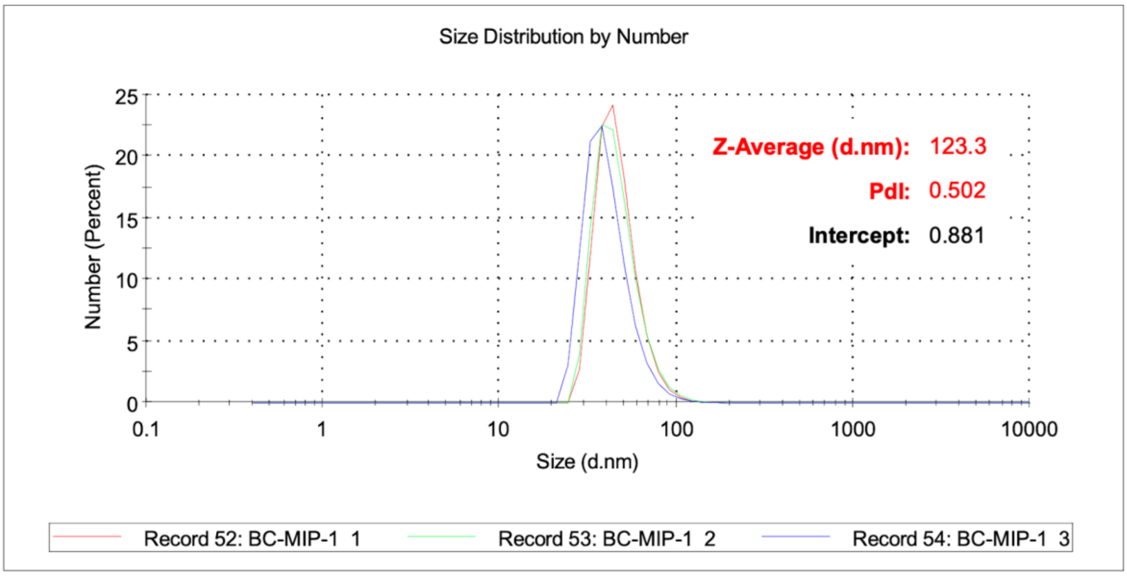

Figure 4.24. The hydrodynamic particle size and polydispersity index (PDI) for MIP1.

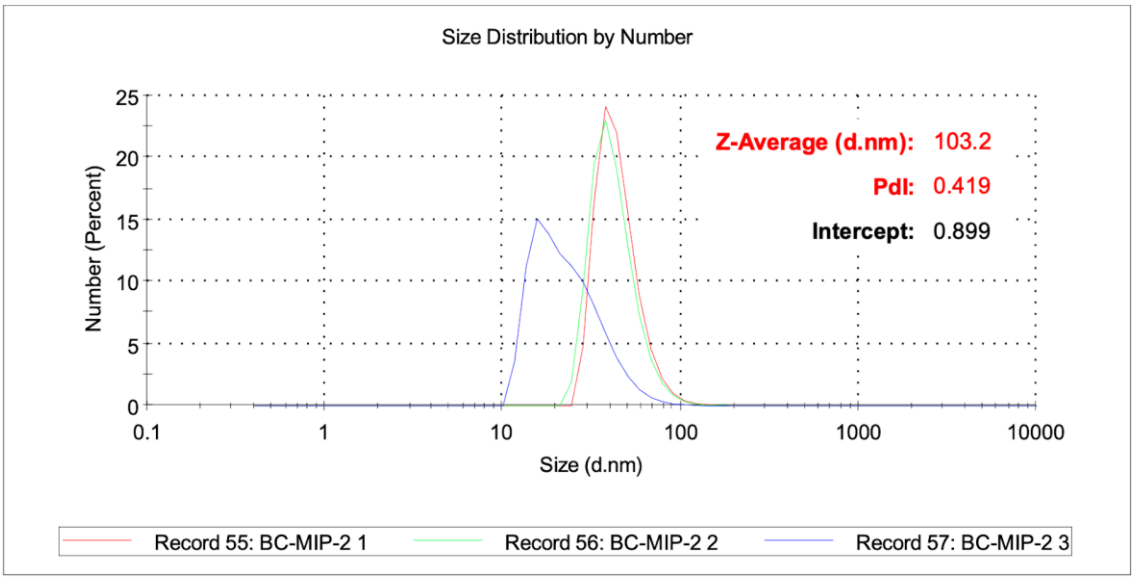

Figure 4.25. The hydrodynamic particle size and polydispersty index (PDI) for MIP2.

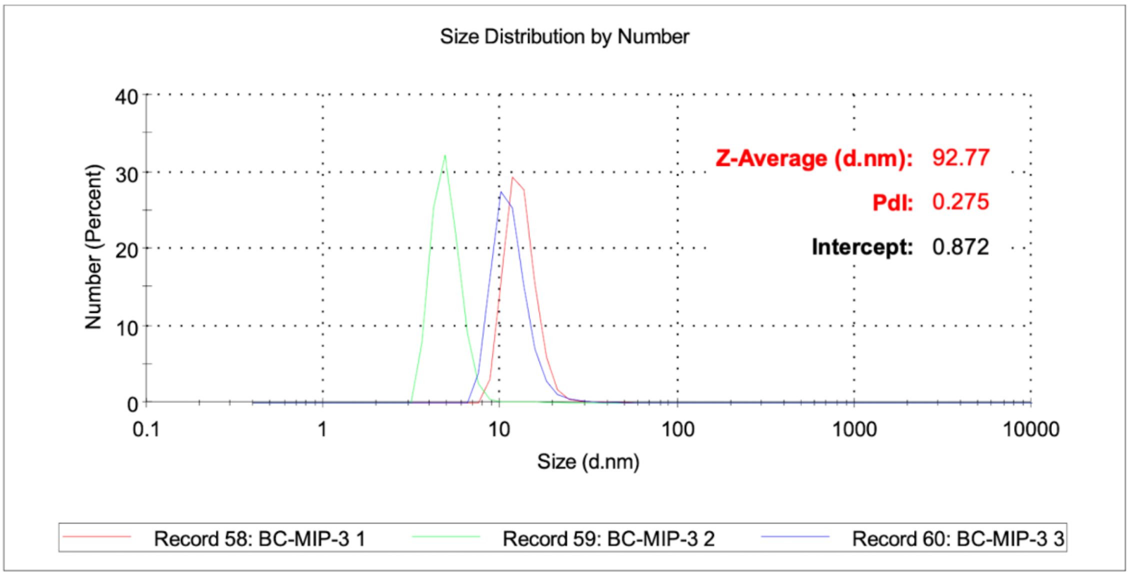

Figure 4.26. The hydrodynamic particle size and polydispersity index (PDI) for MIP3.

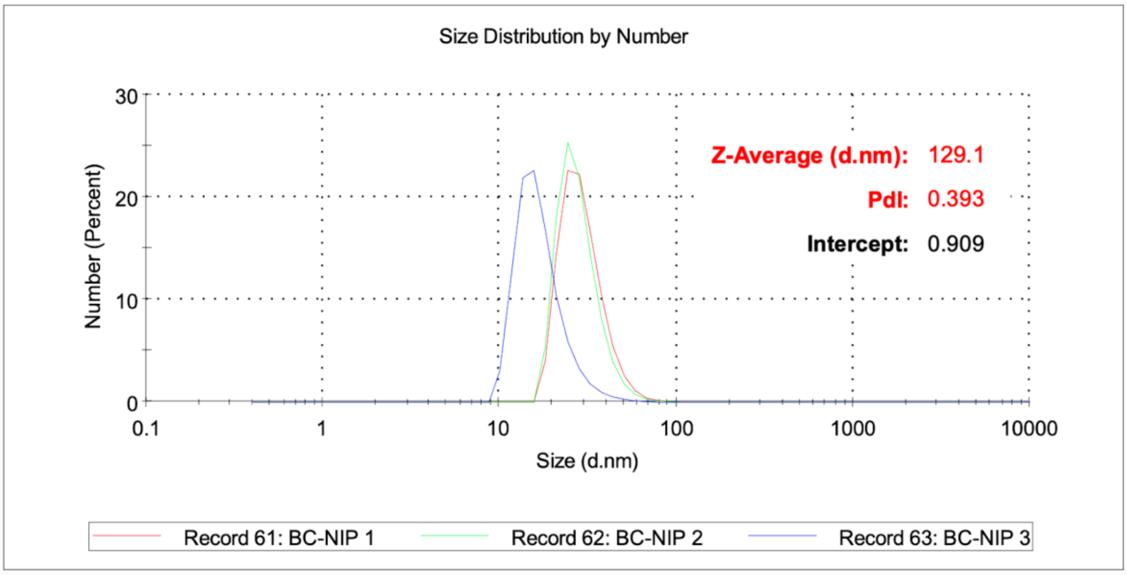

Figure 4.27. The hydrodynamic particle size and polydispersity index (PDI) for NIP.

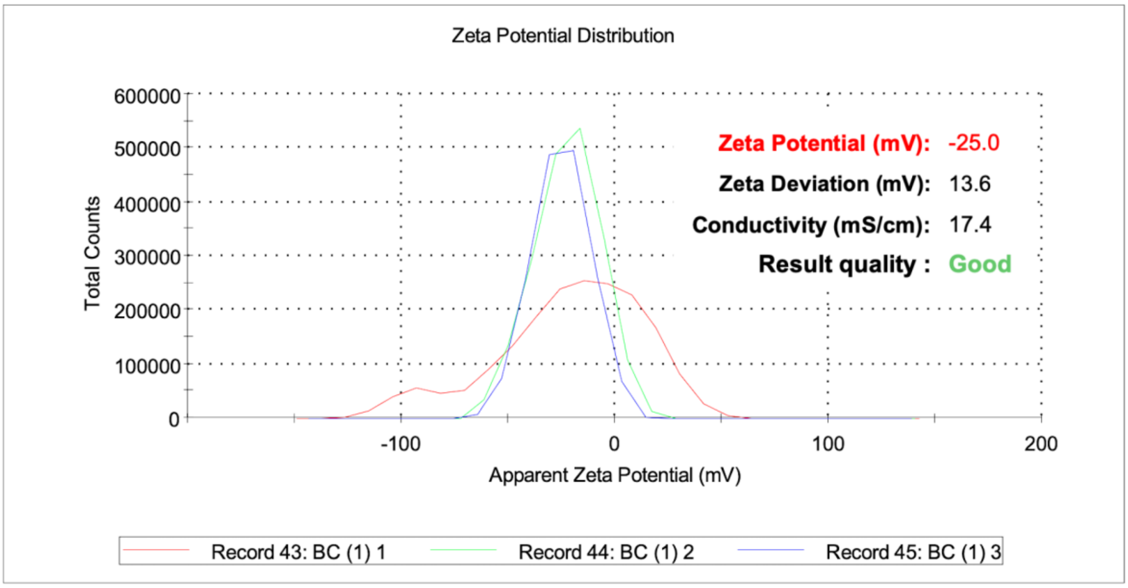

Figure 4.28. The zeta potential (ZP) for BC.

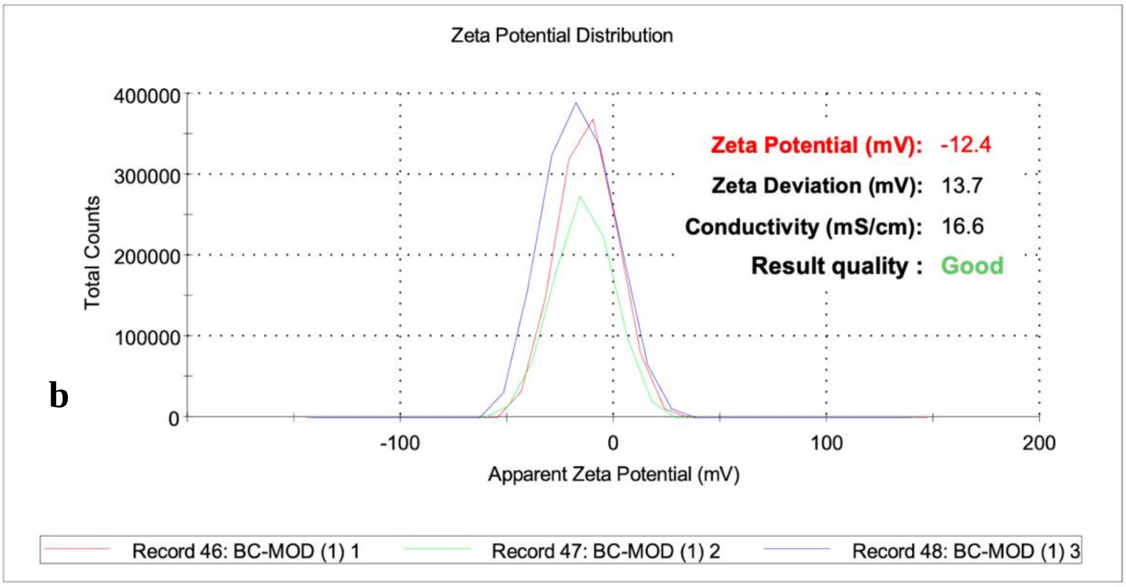

Figure 4.29. The zeta potential (ZP) for M-BC.

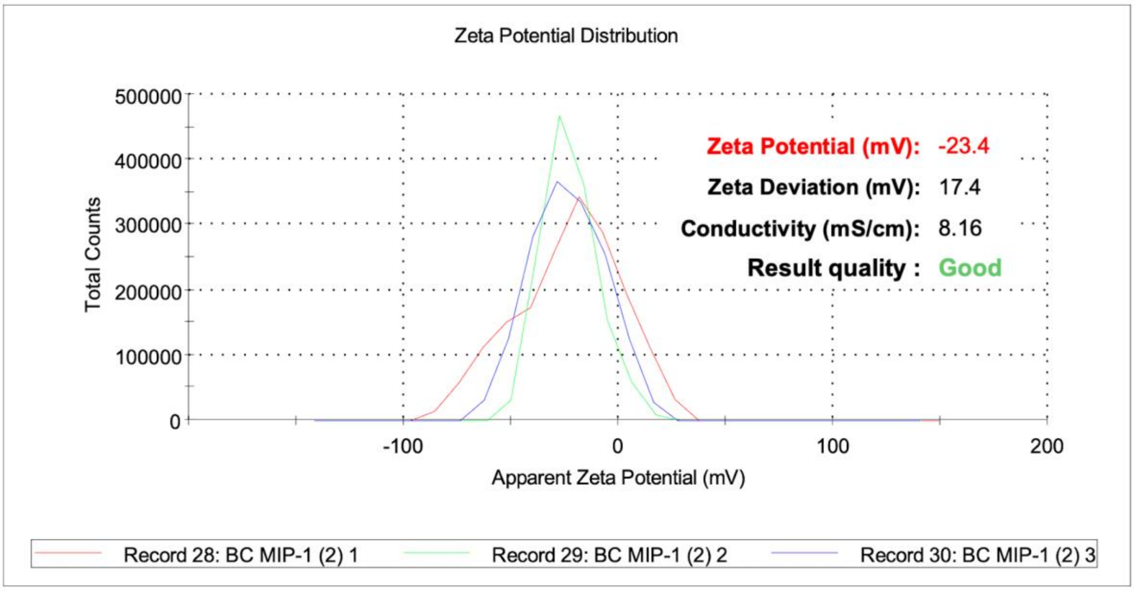

Figure 4.30. The zeta potential (ZP) for MIP1.

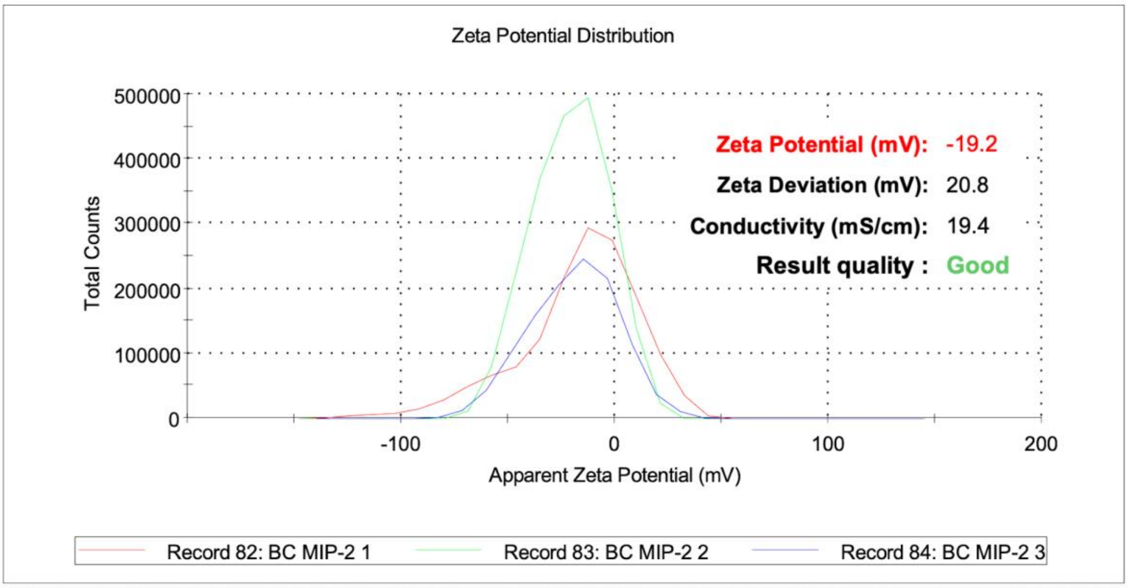

Figure 4.31. The zeta potential (ZP) for MIP2.

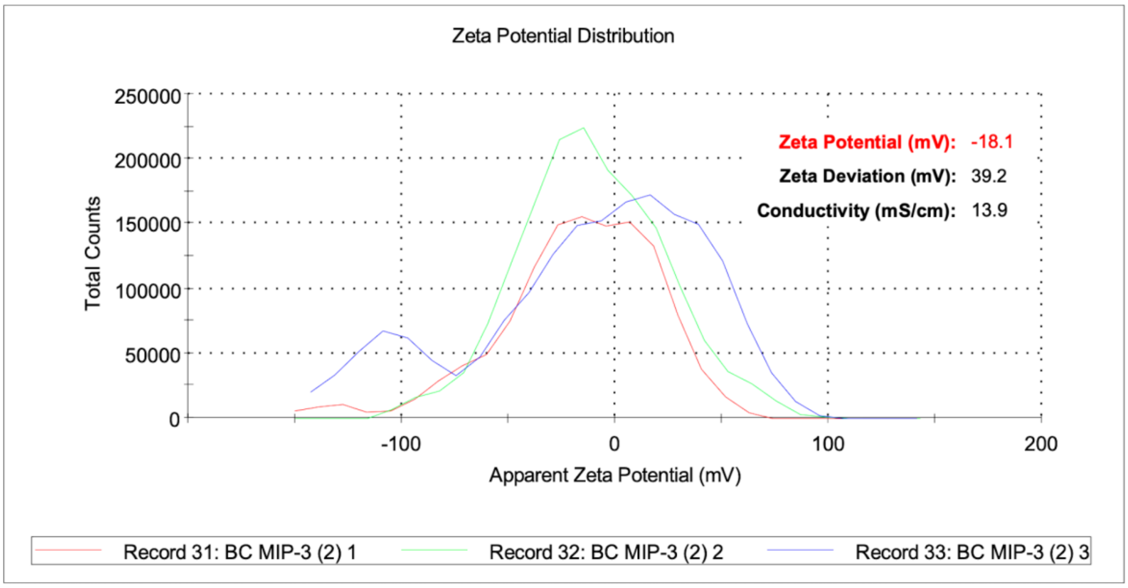

Figure 4.32. The zeta potential (ZP) for MIP3.

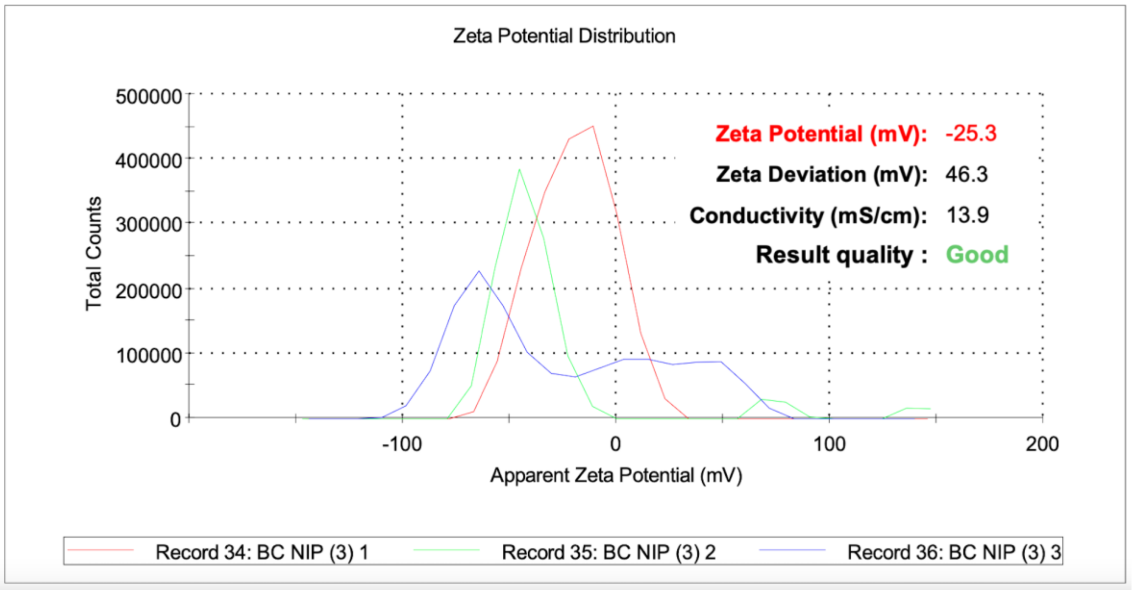

Figure 4.33. The zeta potential (ZP) for NIP.

4.3. A Comparison of The Swelling Index in Media with Different pH

Swelling index of BC, MIPs, and NIP in different pH values (5.5, 7.4) was investigated (12, 24 hours). Different swelling tendencies were noted, and the results are displayed in (Figure 4.34). Highest swelling appeared at 24 hours, with swelling indexes of 1100%, 700%, 816.66%, 572.72%, and 360% for the BC, MIP1, MIP2, MIP3, and NIP, respectively, at pH 7.4; and 740.00%, 600.00%, 666.66, 471.42%, and 328.57%, respectively, at pH 5.5. These results indicate that the surface imprinted polymer layer was successfully synthesized on BC nanofibers. The difference in swelling behavior under different pH values results from the cellulose's properties. The results are strongly supported by the results of Silvestre et al. [166]. The authors informed that the swelling index for BC is lower at pH values of 5, then increases until pH 7, and then decreases slightly until pH 10. The difference between the swelling indexes of BC and MIPs is due to a decrease in the number and availability of hydrophilic sites in MIPs because of their occupation by hydrophobic drugs.

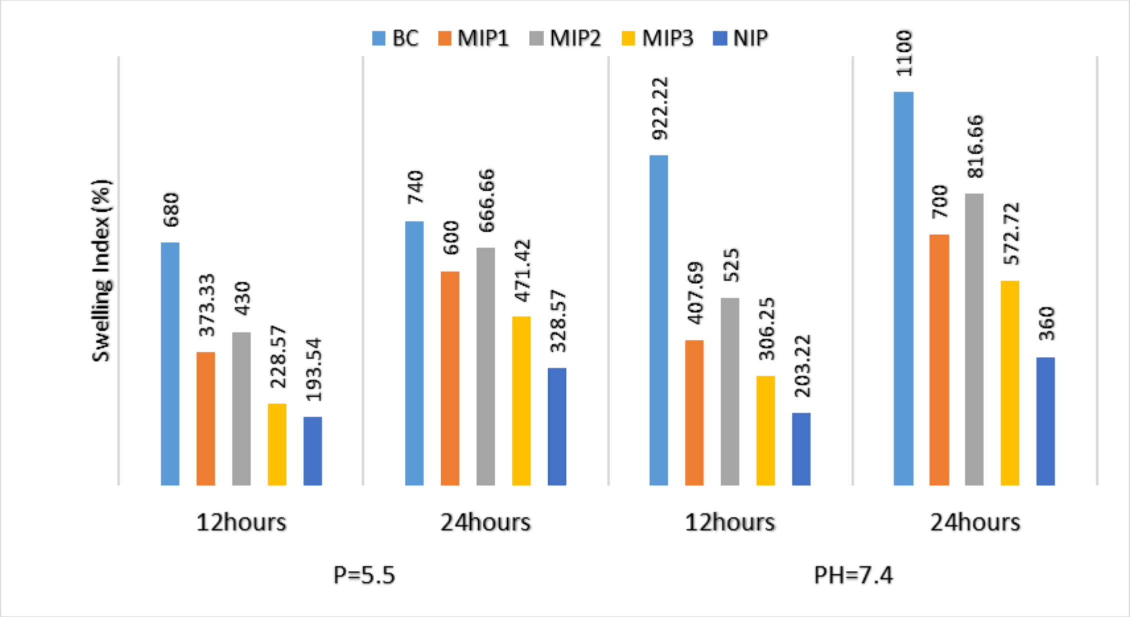

Figure 4.34. Variation in Swelling index (%) with time (12 and 24 hours) for BC, MIPs, and NIP.

4.4. Drug Loading Capacity

To determine the amount of carboxyl-activated CTX loaded, the concentration of the carboxyl-activated CTX solution before and after loading was measured at 296 nm utilizing a UV-VIS spectrophotometer. The prodrug loading capacity was calculated by determining the amount of carboxyl-activated CTX added at the beginning 3 mg/ml, and the amount of carboxyl-activated CTX loaded after incubation. Carboxyl-activated CTX loading capacities were calculated as 80.93%, 93.16%, 93.92%, and 54.84% for MIP1, MIP2, MIP3, and NIP, respectively. The highest loading amount of carboxyl-activated CTX was for MIP3, and the lowest was for MIP1. The drug loading capacity was increased from 80.93% to 93.92%, as the template amount utilized during polymerization increased from 12.5 mg to 50 mg. The fact that the loading amounts of MIPs were greater than those of NIP suggests that the imprinting process successfully prepared selective recognition sites corresponding to CTX molecules throughout MIPs.

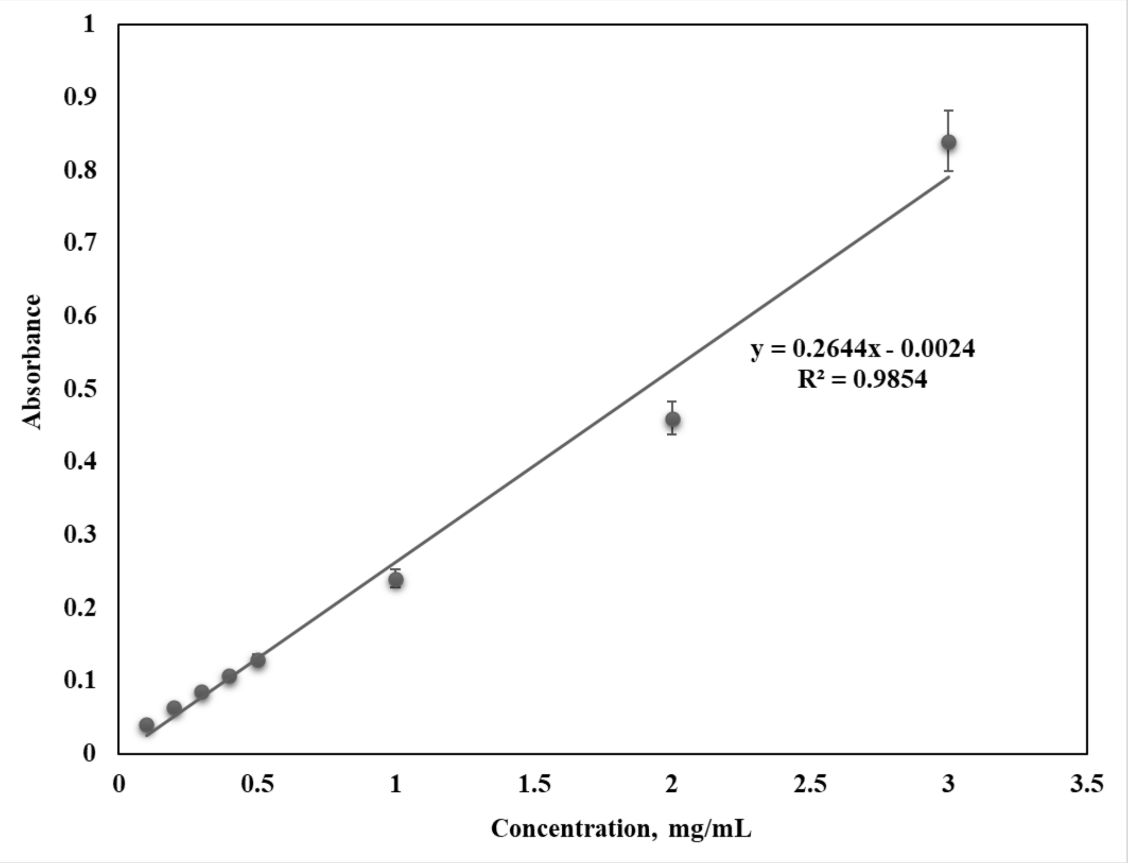

Figure 4.35. Calibration graph of carboxyl-activated CTX in Phosphate buffered saline (PBS) pH 7.4.

4.5. In Vitro Drug Release

4.5.1. Effect of pH on The Drug Release Rate

To determine the effect of pH on carboxyl-activated CTX release, release studies were performed for MIPs and NIP at 5 different pH (5.5, 6, 7, 7.4, 8) with shaking at a rate of 120 rpm; 3 mg/mL; 37°C. (pH 5.5: acetic acid + sodium hydroxide), (pH 6,7,8: KH2PO4 + K2HPO4), and (pH 7.4: Phosphate Buffered Saline (PBS)).

As shown in (Figure 4.36), the release of carboxyl-activated CTX from MIP1 was greatly affected by the environmental pH value of 7.4. Approximately 82.09% within 36 hours. Similarly, about 65.29%, 47.85%, 42.68% and 24.05% of carboxyl-activated CTX were released from MIP1 within 36 h in pH 8, 7, 6, and 5.5, respectively.

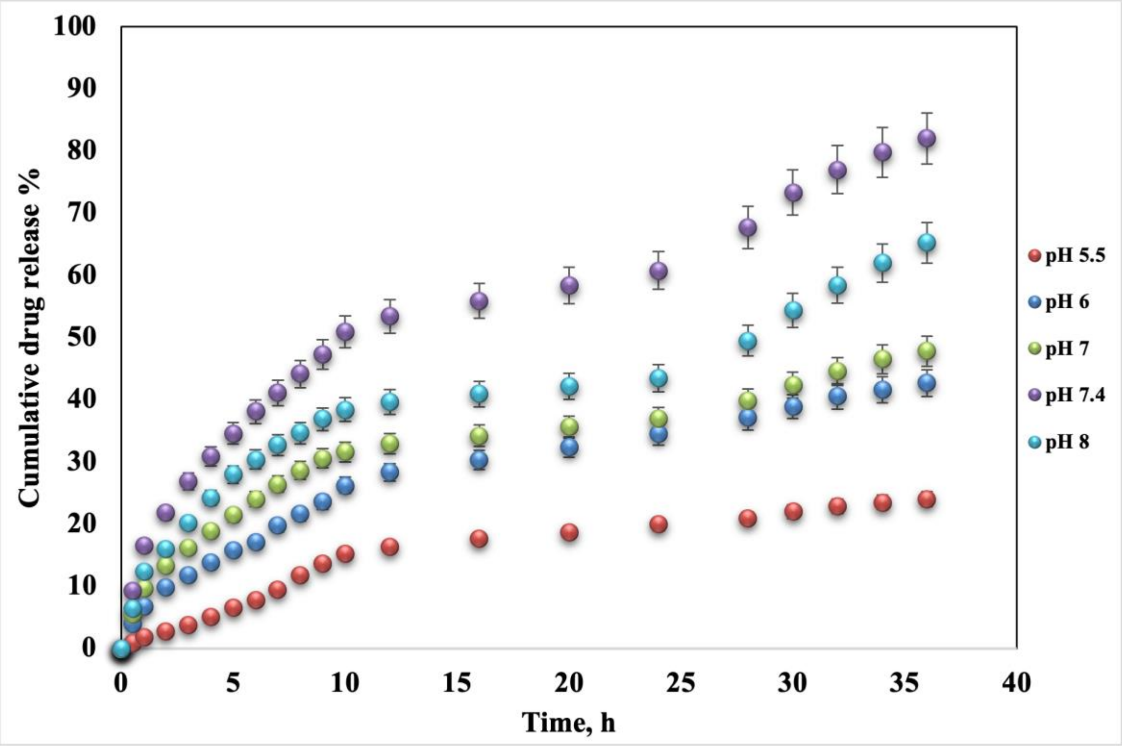

Figure 4.36. Carboxyl-activated CTX release from MIP1 was studied at pH: 5.5,6,7,7.4 and 8; 37°C.

(Figure 4.37) demonstrates that under pH 5.5, a negligible amount of carboxyl-activated CTX is released from MIP2 in a very slow manner, and less than 18.95 % of carboxyl-activated CTX was released after 36 hours of immersion, which is a meagre amount of carboxyl-activated CTX released over such a long release period. The highest amount of release occurred at pH: 7.4. about 93.43%, simulating normal physiological conditions. The total amount of drug released at pH 6, 7, and 8 was observed to be 54.66% and 55.71, 51.91%, respectively, under the same conditions.

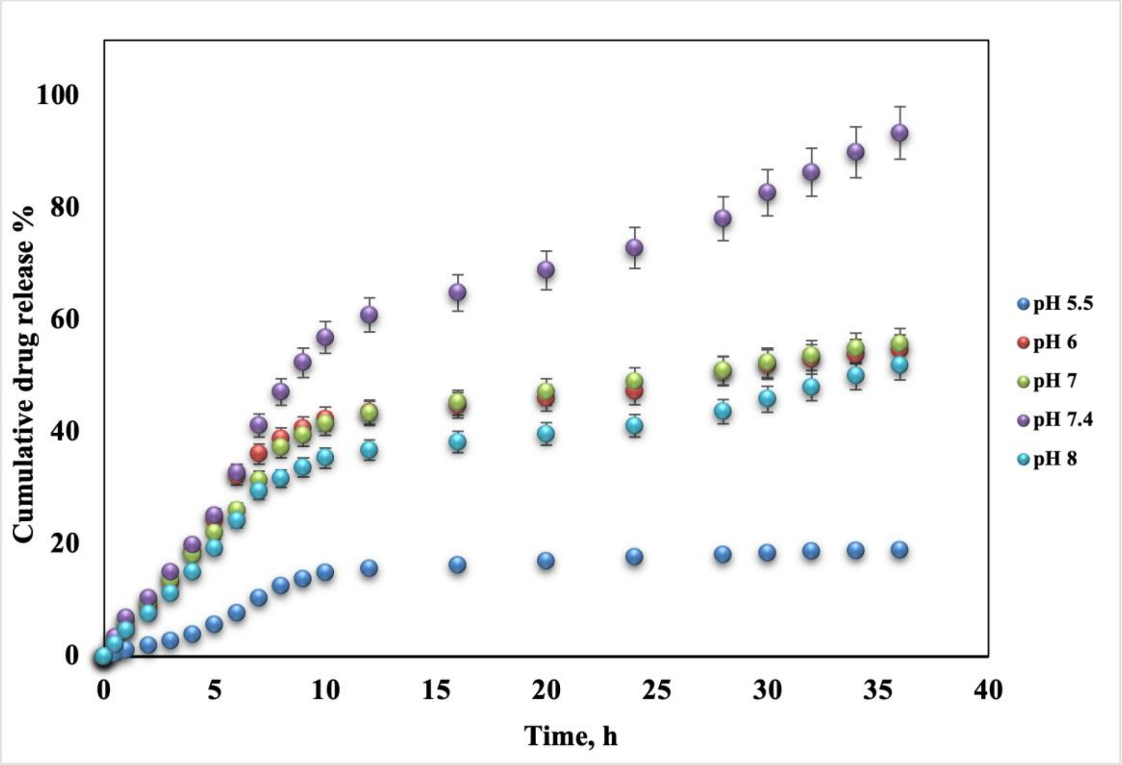

Figure 4.37. Carboxyl-activated CTX release from MIP2 was studied at pH: 5.5,6,7,7.4 and 8; 37°C.

No significant difference in the cumulative carboxyl-activated CTX release of NIP was found in the pH values: 5.5, 6,7, and 8: 13.22%, 14.00%, 13.47%, and 12.93%, with a slight height at pH: 7.4 approximately 19.54% (Figure 4.38).

In conclusion, the carboxyl-activated CTX release profiles showed a pH dependency, with a higher release rate at pH 7.4 than at pH 5.5 in all the MIPs and NIP. However, the carboxyl-activated CTX release profiles at pH 5.5 were gradual and so slow that we think it needs more than 36 hours to release carboxyl-activated CTX. The difference in carboxyl-activated CTX release in these two media could be assigned to the difference in swelling index of the MIPs and NIP in these two media that, show the swelling ratios in pH7.4 was higher than 5.5.

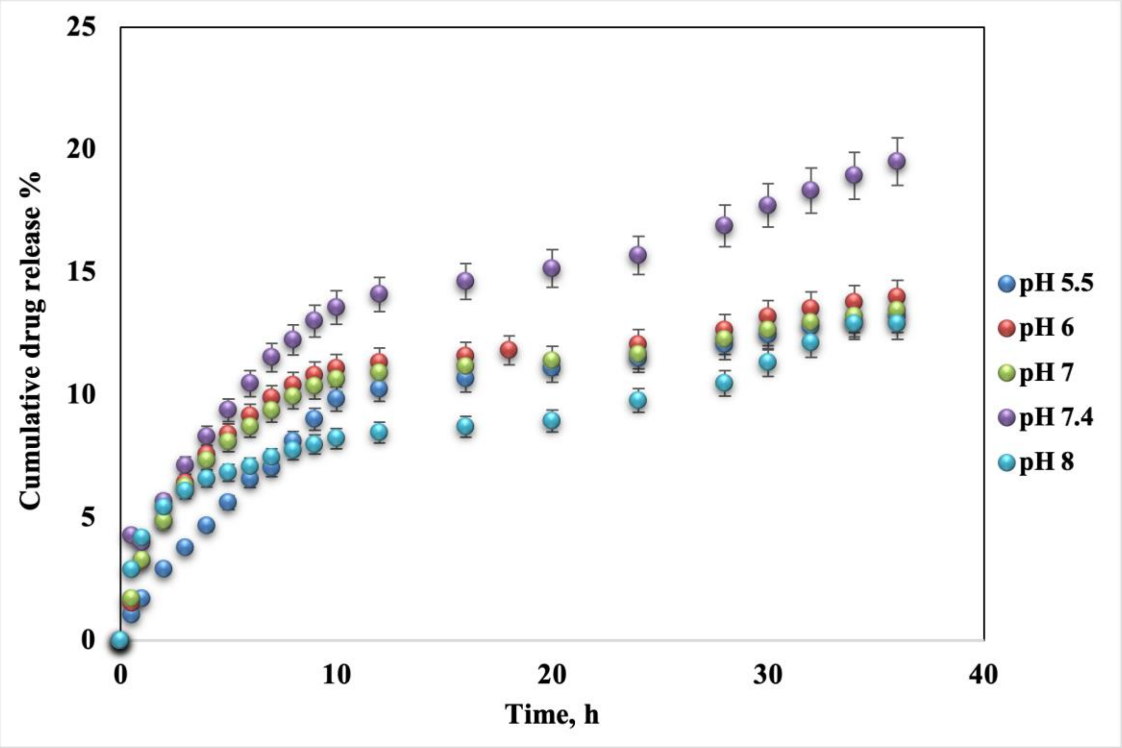

Figure 4.38. Carboxyl-activated CTX release from NIP was studied at pH: 5.5, 6, 7, 7.4, and 8; 37°C.

4.5.2. Effect of Concentration on The Drug Release Rate

To determine the effect of concentration on carboxyl-activated CTX release, release studies were performed for MIPs and NIP at five different concentrations (0.5, 1, 2, 3, 4 mg/ mL); pH: 7.4; 37°C.

In a study involving 0.5 mg/mL of the carboxyl-activated CTX, 94.56% carboxyl-activated CTX was released from MIP1 within 24 hours. Similarly, more than 91.84% of carboxyl-activated CTX was released from MIP2 during the same time frame. During the first 16 hours, MIP1 and MIP2 had the same rate (approximately 52%), but MIP1 slightly increased over the next 8 hours. At 22.55%, the carboxyl-activated CTX release rate was the lowest for NIP.

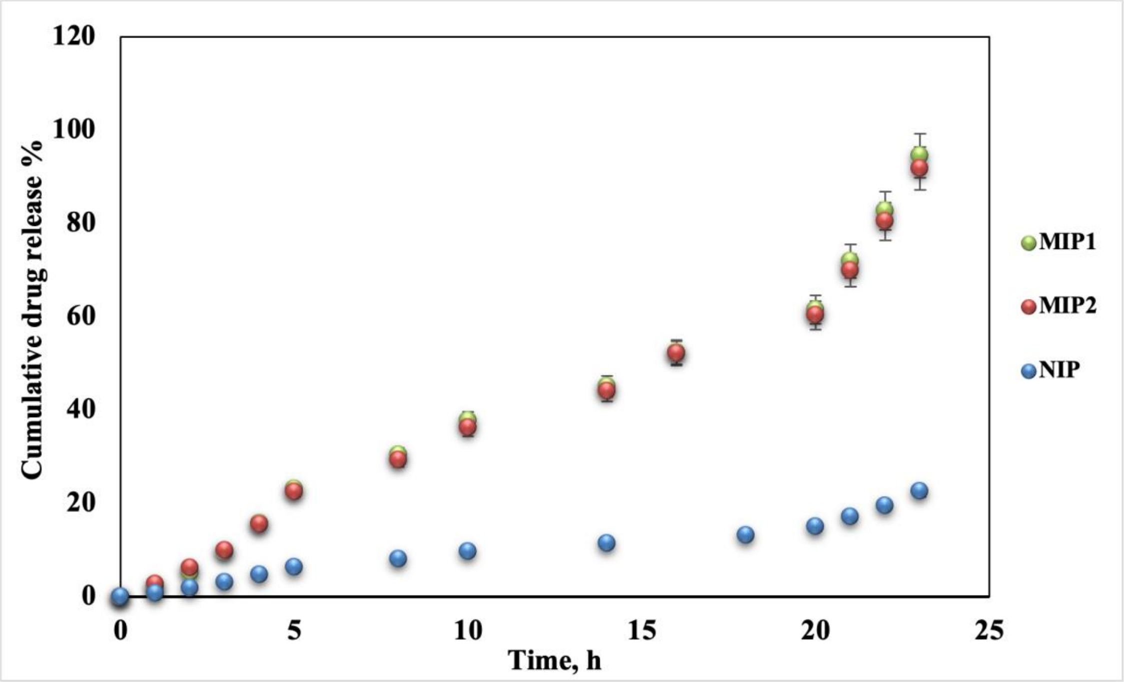

Figure 4.39. Investigation of Carboxyl-activated CTX releases profile in MIPs and NIP at 0.5 mg/mL concentrations. pH: 7.4, Temperature: 37.0°C.

In a study involving 1 mg/mL of the carboxyl-activated CTX, the rate of carboxyl-activated CTX release after 24 hours was determined for MIPs and NIP. MIP2 had the highest release profile with a rate of 64.74 %, followed by MIP1 with 53.67 % and NIP with the lowest rate of 15.85%.

In a study involving 2 mg/mL of the carboxyl-activated CTX, the rate of carboxyl-activated CTX release after 24 hours was determined, and more than 86.76% of carboxyl-activated CTX was released from MIP2. Likewise, over 83.89% of carboxyl-activated CTX was released from MIP1 during the same period. During the first 8 hours, MIP1 and MIP2 had the same rate (approximately 24%), but MIP2's rate increased slightly over the following 16 hours. MIP3 possessed the lowest rate among the MIPs, at 31.75%. NIP was found to have the lowest rate of carboxyl-activated CTX release, 11.62%.

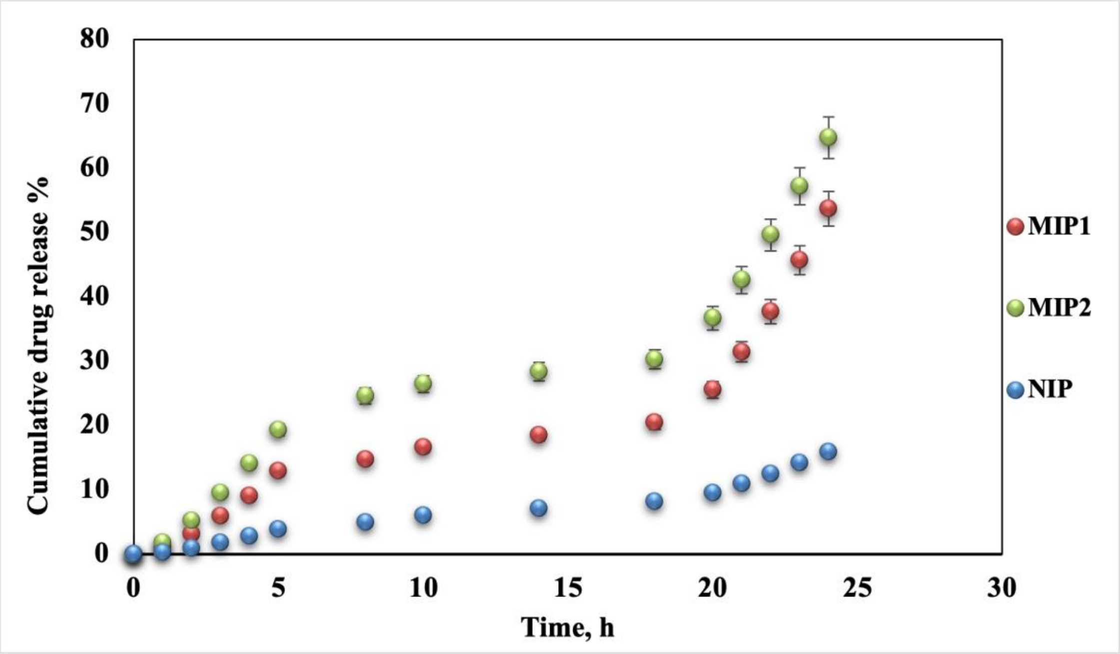

Figure 4.40. Investigation of Carboxyl-activated CTX releases profile in MIPs and NIP at 1 mg/mL concentrations. pH: 7.4, Temperature: 37.0°C.

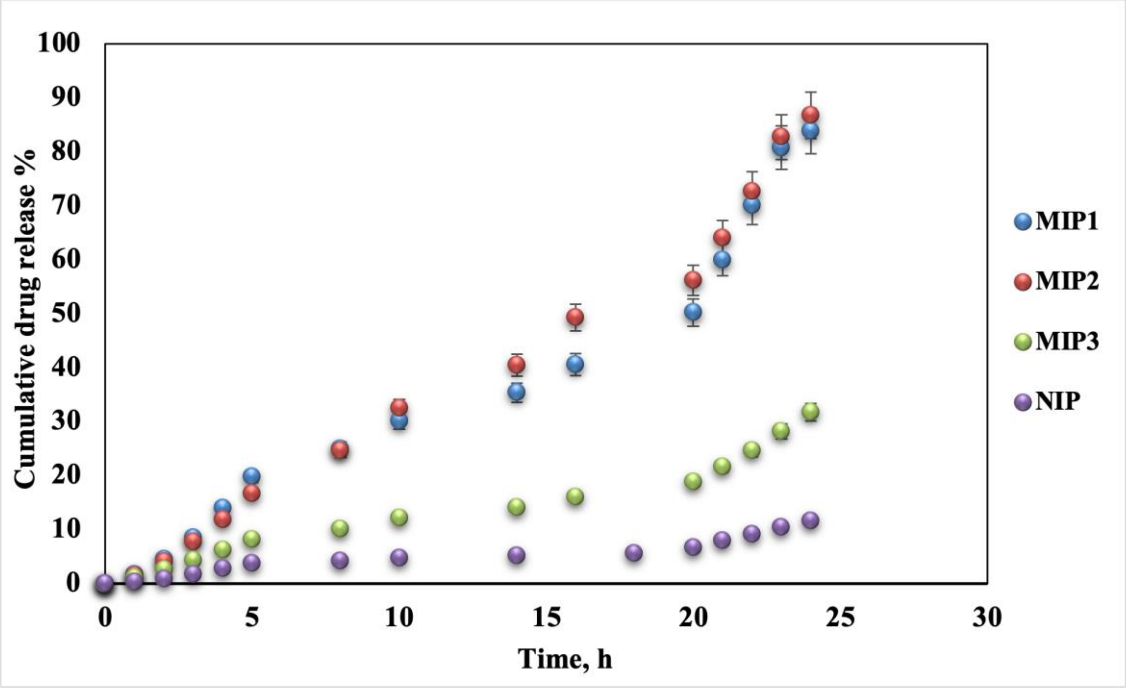

Figure 4.41. Investigation of Carboxyl-activated CTX releases profile in MIPs and NIP at 2 mg/mL concentrations. pH: 7.4, Temperature: 37.0°C.

In a study involving 3 mg/mL of the carboxyl-activated CTX, the rate of carboxyl-activated CTX release after 36 hours was determined, and more than 93.43% of carboxyl-activated CTX was released from MIP2. Likewise, over 82.09% of carboxyl-activated CTX was released from MIP1 during the same period. During the first 9 hours, MIP1 and MIP2 had the same rate (approximately 47.34%), but MIP2's rate increased slightly over the following 27 hours. MIP3 possessed the lowest rate among the MIPs, at 43.7%. NIP was found to have the lowest rate of carboxyl-activated CTX release, 19.53%.

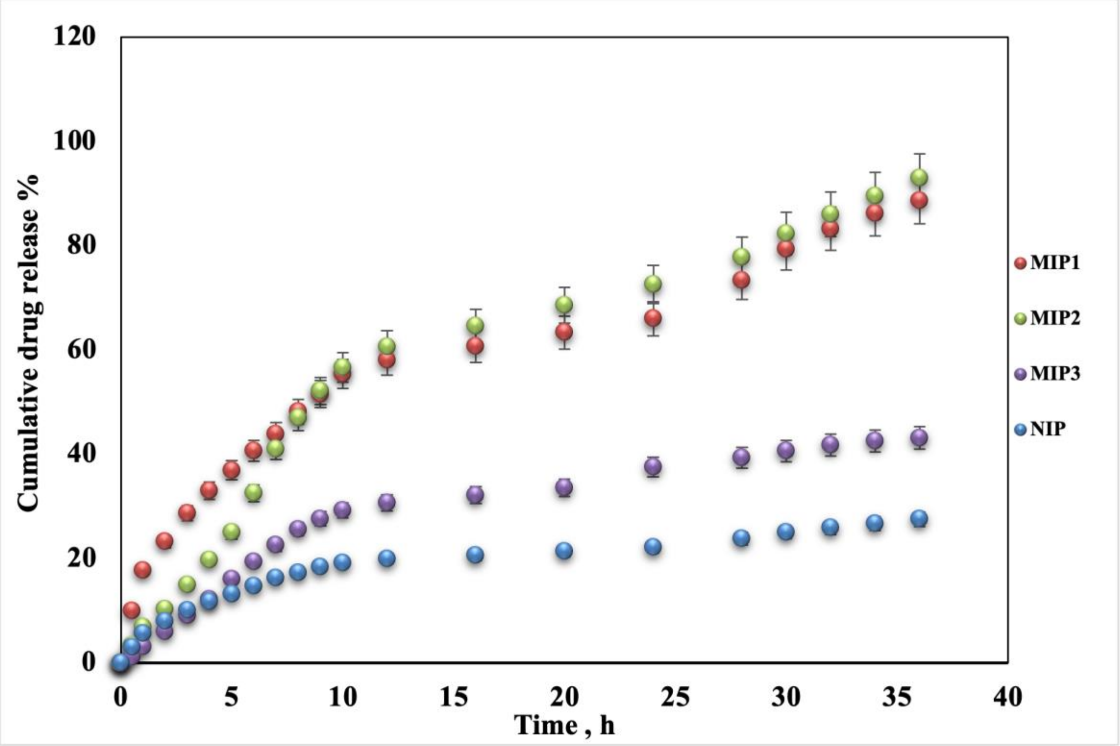

Figure 4.42. Investigation of Carboxyl-activated CTX releases profile in MIPs and NIP at 3 mg/mL concentrations. pH: 7.4, Temperature: 37.0°C.

In a study involving 4mg/mL of the carboxyl-activated CTX, the rate of carboxyl-activated CTX release after 24 hours was determined for MIPs and NIP. MIP2 had the highest release profile with a rate of 92.53%, followed by MIP1 with 91.31%, almost the same, and NIP with the lowest rate of 11.19%.

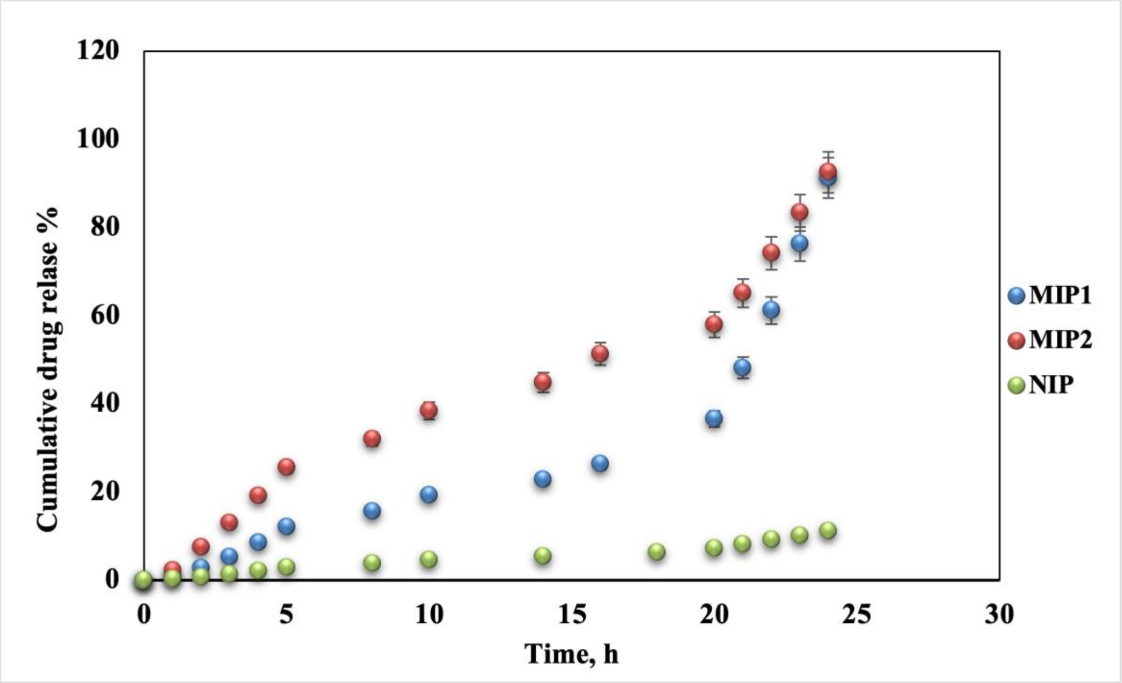

Figure 4.43. Investigation of Carboxyl-activated CTX releases profile in MIPs and NIP at 4 mg/mL concentrations. pH: 7.4, Temperature: 37°C.

4.5.3. Effect of Temperature on The Drug Release Rate

To determine the effect of temperature on carboxyl-activated CTX release, release studies were performed for MIPs and NIP at 3 temperatures (25, 37, 40°C); pH: 7.4; 3mg/mL. The cumulative drug releases at 25°C were 33.63%, 75.06%, and 16.64% for MIP1, MIP2, and NIP, respectively.

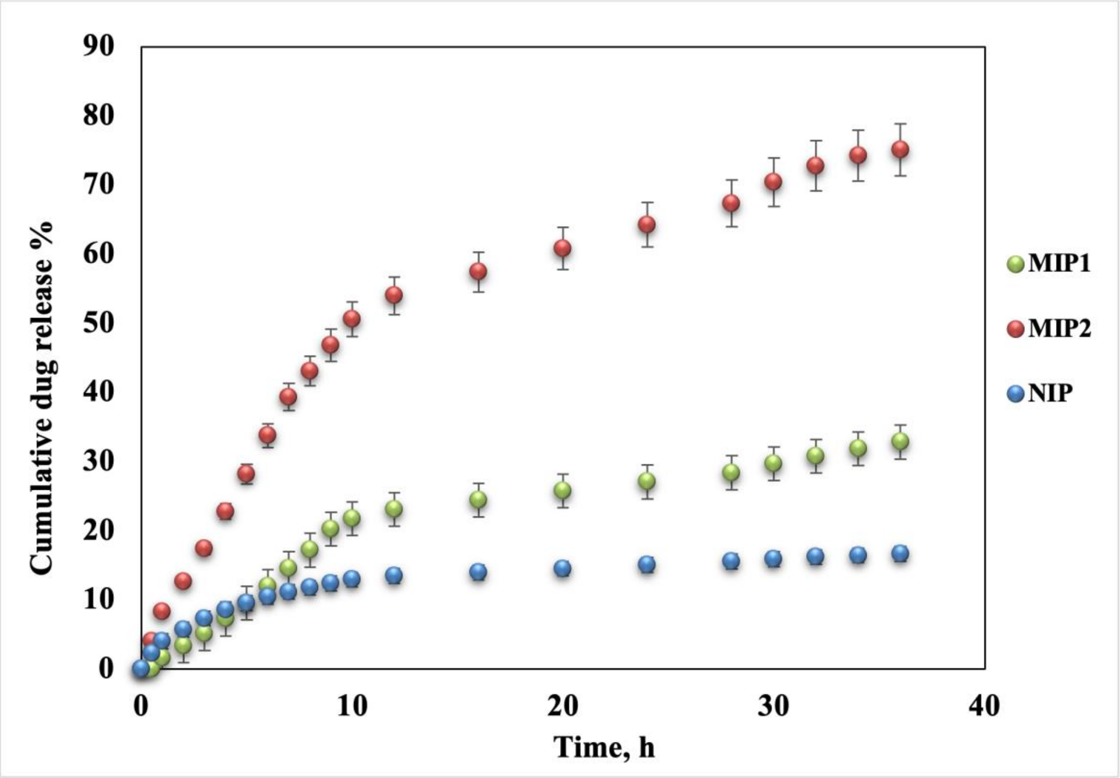

Figure 4.44. Investigation of Carboxyl-activated CTX releases profile in MIPs and NIP at 25°C. pH: 7.4, 3 mg/mL.

According to (Figure 4.45), cumulative drug releases at 37°C for MIP1, MIP2, MIP3, and NIP were 88.65%, 93.02%, 43.17%, and 27.57%, respectively, under identical conditions. During the first 12 hours, MIP1 and MIP2 had the same rate (approximately 60%), but MIP2 slightly increased over the next 24 hours. As the temperature rises from 25 to 37°C, the cumulative drug release rate increases in both MIPs and NIP. At both temperatures, MIP2 was more significant than the other samples.

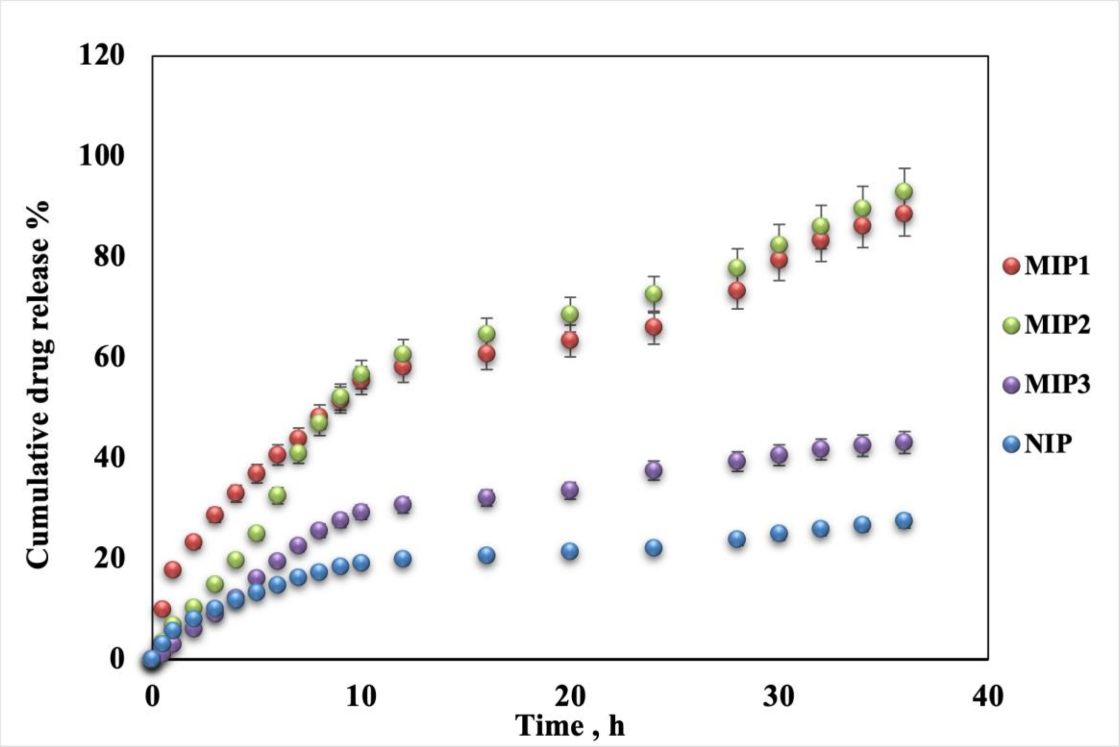

Figure 4.45. Investigation of Carboxyl-activated CTX releases profile in MIPs and NIP at 37°C. pH: 7.4, 3 mg/mL.

In comparison between 25, 37, and 40°C, the highest cumulative drug releases were at 40°C (Figure 4.46) for all the samples. MIP2 had the maximum cumulative drug release rate of 96.55% for 36 hours, followed by 92.49% and 28.60% for MIP1 and NIP, respectively.

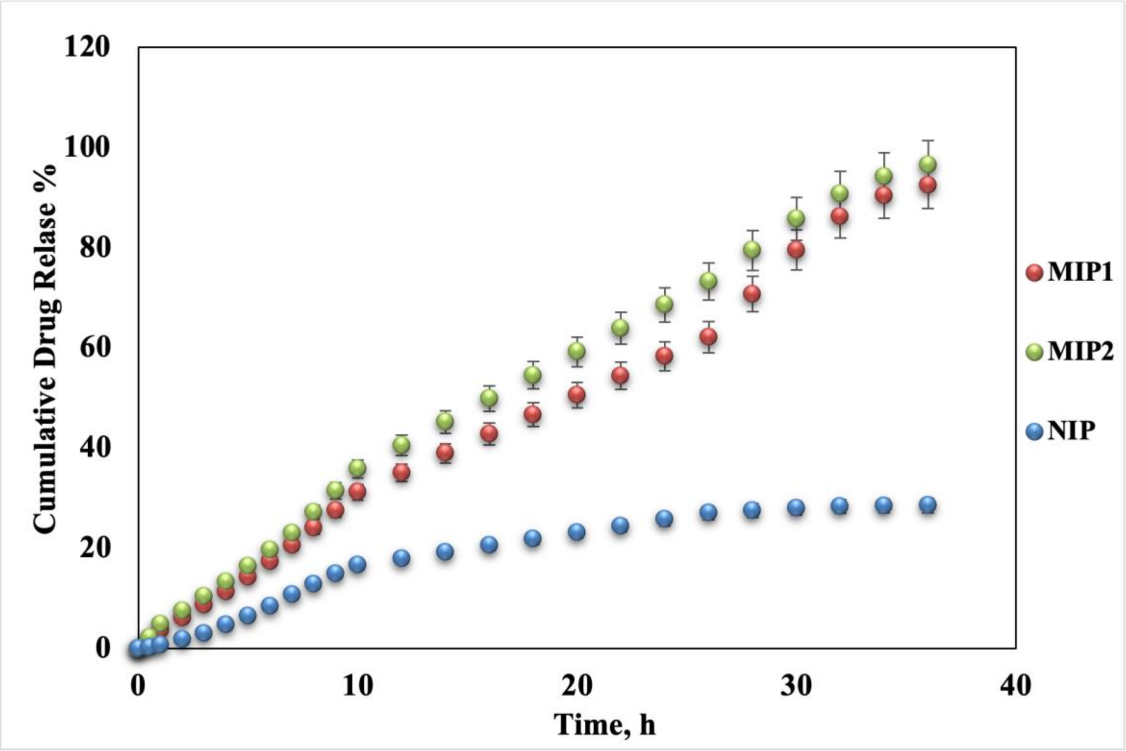

Figure 4.46. Investigation of Carboxyl-activated CTX releases profile in MIPs and NIP at 40°C. pH: 7.4, 3 mg/mL.

In conclusion, the results indicate that the drug release rates of the MIPs and NIP were significantly accelerated at 40°C. MIP2 had the highest release rate at 96.55%, followed by MIP1 at 92.49%, and NIP at 28.60%. It was anticipated that temperature variations would significantly affect the drug release performance. Higher temperatures may result in a greater cumulative release than lower temperatures. When the temperature is 40°C, the polymer chains will entangle and polymerize, causing the MIPs and NIP structures to shrink and accelerating the drug release from the centers of the MIPs and NIP.

4.5.4. Drug Release in Plasma

(Figure 4.47) showed maximum carboxyl-activated CTX release in 72 hours as 86.67%, 95.31%, 76.45%, and 25.26% of the cumulative release from MIP1, MIP2, MIP3, and NIP, respectively. MIPs maintained their stability in plasma throughout prodrug release. MIP2 had the highest cumulative release, while the lowest rate was for MIP3. The releasing amounts of MIPs were higher than those of NIP even though the cumulative release was approximately 4.4% for NIP in the first 1 h of the carboxyl-activated CTX release analysis. In comparison, it was approximately less than 1% for MIPs.

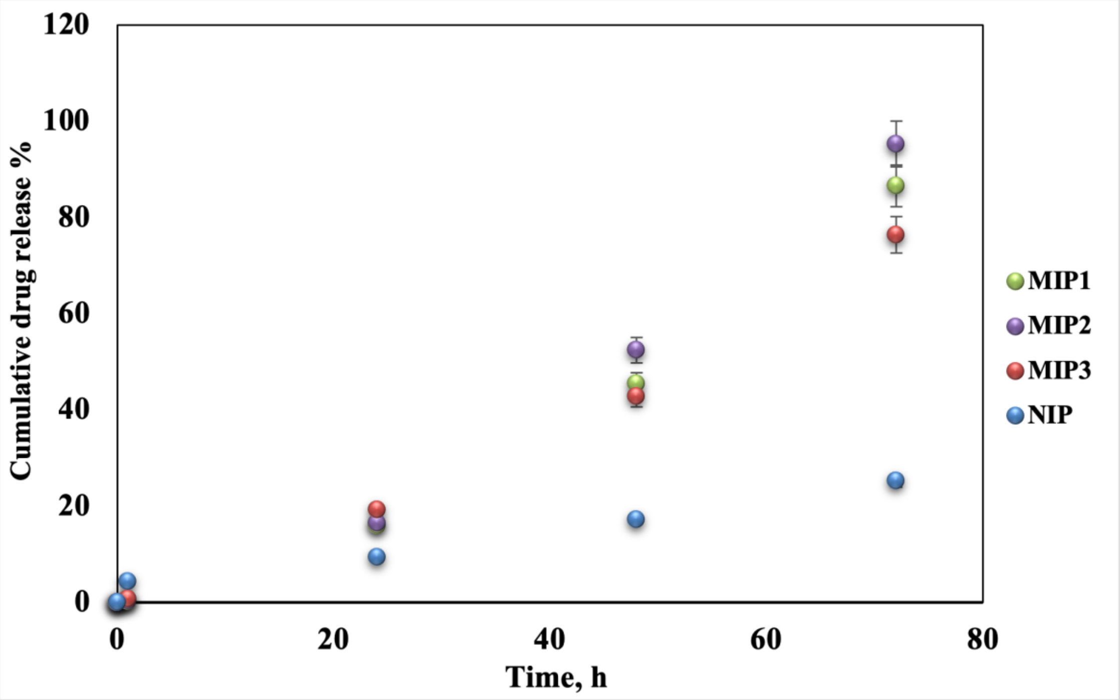

Figure 4.47. Cumulative release of Carboxyl-activated CTX from MIPs and NIP in plasma at 37°C.

5. CONCLUSIONS

- This study aims to develop polymeric systems (composite bacterial cellulose nanofibers) for Cabazitaxel (CTX) release using the molecular imprinting technique.
- Utilizing CTX prodrugs is a promising strategy for overcoming its high toxicity and poor water solubility. The more reactive 2′-(OH) group of CTX was successfully converted to a (COOH) group via treatment with succinic anhydride.
- According to the UV-VIS spectrum of carboxyl-activated CTX (Figure 4.1), which showed absorption at (λmax (nm)) = 296, It's don't show absorption like absorption of CTX that shows absorption usually at UV (λmax (nm)) = 231 and it's shown formation a new product
- Esterification was confirmed by the (C=O) and (C-O) stretching vibrations observed at 1720.84 and 1231 cm^{-1}, respectively (Figure 4.2).
- ^1H-NMR was used to characterize the spectra of succinic anhydride-CTX conjugate (CDCl3). The peak at 5.37 ppm indicated that succinic anhydride was successfully conjugated to CTX via an ester bond. The $-CH_2-CH_2-$ bonds in the carboxyl-activated CTX were represented by a second peak between 2.71 and 2.61 ppm.
- Carboxyl-activated CTX-MAA pre-complex was synthesized and characterized by UV-visible spectroscopy. According to the graph in (Figure 4.6-8), the carboxyl-activated CTX-MAA pre-complex ratio was chosen as in (Table 3.1.).
- MIPs and NIP were prepared on the surface of M-BC nanofibers via in-situ polymerization and characterized by various methods such as FTIR, FIB-SEM, TGA/DTG, DLS (Hydrodynamic particle size(diameter), poly dispersive index (PDI), and zeta potential) and it was concluded that MIPs and NIP were successfully synthesized.
- FTIR results (Figure 4.9-15) confirmed the synthesis of MIPs and NIP.
- The resulting MIP1, MIP2, MIP3, and NIP had diameters of 42-59 nm, 31–38 nm, 45–49 nm, and 143–166 nm, respectively. These results are close to the previous studies' SEM results that demonstrated that BC nanofiber produced from the Komagataeibacter intermedius strain is similar to cellulose in morphology. Bacterial cellulose membranes (nanofibrils) were randomly organized in all samples and displayed a typical nanofibril structure.

- Thermal gravimetric analysis (TGA) and derivative thermograms (DTG) for BC, M-BC, MIPs, and NIP are shown in (Figure 4.20). The thermogravimetric curves of BC exhibited three main thermal events. The first event occurred at approximately 30–240°C (6.49% weight loss) due to a small amount of moisture. The second event started at 240-340°C and was related to cellulose degradation. Maximum weight loss is observed at 320°C. The surface-modified BC showed about 6.71% weight loss due to evaporation of adsorbed water,, followed by a continuing loss of dry matter at 220-350°C and 55.62% of the total weight loss after acetylation. (Figure 4.21. c,d,e,f) demonstrates that the first slight weight loss up to 275, 220, 200, and 100°C to MIP1, MIP2, MIP3, and NIP, respectively, is attributed to the physical desorption of surface-adsorbed water. The second event of rapid weight loss occurs at the temperature between 275-400°C, 220-355°C, 200-340°C, and 100-345°C because of the loss of the polymer layer. Together, the third event of weight loss occurs in the depolymerization of cellulose and the decomposition of glucose units.
- The BC nanofibers displayed a size distribution with an average hydrodynamic diameter of 79.08±10.70 nm. The size of membranes increased when adding the drug carboxyl-activated CTX (Table 4.1).
- Zeta potential measurement enables the prediction of the storage stability of colloidal particles, as charged particles will exhibit less particle aggregation. The value of zeta potential of BC nanofibers, M-BC nanofiber, MIPs1,2,3, and NIP were -22.7±2.12, -14.2±1.80, -23.00±0.52, -18.76±1.88, -17.40±0.96, -22.83±3.06 mV respectively.
- The swelling index of BC, MIPs, and NIP in media with different pH values of 5.5 and 7.4 were investigated in 12 and 24 hours (Figure 4.34). The highest swelling appeared at 24 hours, with indexes of 1100%, 700%, 816.66%, 572.72%, and 360% for BC, MIP1, MIP2, MIP3, and NIP, respectively. The difference in swelling behaviour under different pH values results from the cellulose's properties.
- The drug loading capacity was calculated by determining the carboxyl-activated CTX added at 3 mg/ml beginning and after incubation. The fact that the loading amounts of MIPs were more significant than those of NIP suggests that the imprinting process successfully prepared selective recognition sites complementary to CTX molecules throughout MIP1, MIP3, and NIP. In MIP1, the template amount utilized during polymerization went from 12.5 mg to 50 mg, and the loading capacity increased from 80.93% to 93.92%.

- The carboxyl-activated CTX release profiles exhibited a pH dependency, with a higher release rate at pH 7.4 than at pH 5.5 in all the MIPs and NIP. The difference could be assigned to the difference in swelling index of the MIPs and NIP in these two media, showing that the swelling ratios in pH 7.4 were higher than 5.5.
- The carboxyl-activated CTX release profiles exhibited a concentration dependency, 0.5, 3, 4 mg/mL were the best. MIP2 shows a higher release rate at all the concentrations than other MIPs and NIP. However, MIP1 at 0.5 mg/mL has the highest rate, with 94.56%.
- MIP2 had the highest release rate at 96.55%, followed by MIP1 at 92.49%, and NIP at 28.60%. It was anticipated that temperature variations would signify the drug release performance. Higher temperatures may result in a greater cumulative release than lower temperatures. When the temperature is 40°C, the polymer chains will entangle and polymerize, causing the MIPs and NIP structures to shrink and accelerating the drug release from the centers of it.
- MIPs retained their stability in plasma during the release period. MIP2 had the highest cumulative release, while the lowest rate was for MIP3. The releasing amounts of MIPs were higher than those of NIP even though the cumulative release was approximately 4.4% for NIP in the first 1 h of the carboxyl-activated CTX release analysis.

6. REFERENCE

[1] F. Bray, J. Ferlay, I. Soerjomataram, R.L. Siegel, L.A. Torre and A. Jemal, *Global cancer statistics 2018: GLOBOCAN estimates of incidence and mortality worldwide for 36 cancers in 185 countries*, CA. Cancer J. Clin. 68 (2018), pp. 394–424.

[2] M. Rosellini, M. Santoni, V. Mollica, A. Rizzo, A. Cimadamore, M. Scarpelli et al., *Treating Prostate Cancer by Antibody – Drug Conjugates*, (2021), pp. 1–15.

[3] Y. Chen, Y. Deng, C. Zhu and C. Xiang, *Biomedicine & Pharmacotherapy Anti prostate cancer therapy : Aptamer-functionalized , curcumin and cabazitaxel co-delivered , tumor targeted lipid-polymer hybrid nanoparticles*, Biomed. Pharmacother. 127 (2020), pp. 110181.

[4] N. Brighi, V. Conteduca, C. Lolli, G. Gurioli, G. Schepisi, M. Palleschi et al., *The cyclin-dependent kinases pathway as a target for prostate cancer treatment: rationale and future perspectives*, Crit. Rev. Oncol. Hematol. 157 (2021), pp. 103199.

[5] G. Gurioli, V. Conteduca, N. Brighi, E. Scarpi, U. Basso, G. Fornarini et al., *Circulating tumor cell gene expression and plasma AR gene copy number as biomarkers for castration-resistant prostate cancer patients treated with cabazitaxel*, (2022), pp. 1–13.

[6] H. Hongo, T. Kosaka and M. Oya, *Analysis of cabazitaxel-resistant mechanism in human castration-resistant prostate cancer*, Cancer Sci. 109 (2018), pp. 2937–2945.

[7] B. Mellado, N. Jimenez, M. Marin-Aguilera and O. Reig, *Diving into cabazitaxel's mode of action: more than a taxane for the treatment of castration-resistant prostate cancer patients*, Clin. Genitourin. Cancer 14 (2016), pp. 265–270.

[8] A. Deveci, O. Gamze, G. Eskiler, S. Kaleli and E. Sahin, *Immunotherapeutic role of cabazitaxel treatment in the activation of TLR3 signalling in metastatic castration - resistant prostate cancer in vitro*, Mol. Biol. Rep. 49 (2022), pp. 1261–1271.

[9] R.J. Lee, G. Cai, J. Wang, M. Wang, J. Lu, L. Teng et al., *Cabazitaxel-loaded human serum albumin nanoparticles as a therapeutic agent against prostate cancer*, (2016), pp. 3451–3459.

[10] C. Kocherlakota, N. Banda, T. Singh, P. Vure, M. Biswas, H.P. Bhagwatwar et al., *Pharmaceutical formulations of cabazitaxel*, Google Patents (2013), .

[11] O. Aydin, I. Youssef, Y.Y. Durmaz, G. Tiruchinapally and M.E.H. Elsayed, *Formulation of Acid-Sensitive Micelles for Delivery of Cabazitaxel into Prostate Cancer Cells*, (2016), .

[12] J.A. Yared and K.H.R. Tkaczuk, *Update on taxane development: new analogs and new formulations*, Drug Des. Devel. Ther. 6 (2012), pp. 371.

[13] R.I. Ema, *O ncologist Medicinal Products for Human Use*, 44 (2012), pp. 543–549.

[14] B. Sun, H. Jing, M.T. Mabrouk, Y. Zhang, H. Jin and J.F. Lovell, *A surfactant-stripped cabazitaxel micelle formulation optimized with accelerated storage stability,* Pharm. Dev. Technol. 25 (2020), pp. 1281–1288.

[15] Y. Sun, Y. Zhao, S. Teng, F. Hao, H. Zhang, F. Meng et al., *Folic acid receptor-targeted human serum albumin nanoparticle formulation of cabazitaxel for tumor therapy,* Int. J. Nanomedicine 14 (2019), pp. 135.

[16] O.C. Nano-system and H. Wang, *Combination Therapy of Metastatic Castration-Recurrent Prostate Cancer : Hyaluronic Acid Decorated , Cabazitaxel-Prodrug*, (2021), pp. 3605–3616.

[17] T. Liu, H. Zou, J. Mu, N. Yu, Y. Xu, G. Liu et al., *Acid-sensitive PEGylated cabazitaxel prodrugs for antitumor therapy*, 32 (2021), pp. 1751–1754.

[18] A.E. Mathew, M.R. Mejillano, J.P. Nath, R.H. Himes and V.J. Stella, *Synthesis and evaluation of some water-soluble prodrugs and derivatives of taxol with antitumor activity*, J. Med. Chem. 35 (1992), pp. 145–151.

[19] Z. Wan, F. Xie, L. Wang, G. Zhang and H. Zhang, *Preparation and evaluation of cabazitaxel-loaded bovine serum albumin nanoparticles for prostate cancer*, Int. J. Nanomedicine 15 (2020), pp. 5333.

[20] Y. Yang, J. Bteich and S.-D. Li, *Current update of a carboxymethylcellulose-PEG conjugate platform for delivery of insoluble cytotoxic agents to tumors*, AAPS J. 19 (2017), pp. 386–396.

[21] A.K. Saleh, H. El-Gendi, N.A. Soliman, W.K. El-Zawawy and Y.R. Abdel-Fattah, *Bioprocess development for bacterial cellulose biosynthesis by novel Lactiplantibacillus plantarum isolate along with characterization and antimicrobial assessment of fabricated membrane*, Sci. Rep. 12 (2022), pp. 1–17.

[22] N.H. Avcioglu, M. Birben and I. Seyis Bilkay, *Optimization and physicochemical characterization of enhanced microbial cellulose production with a new Kombucha consortium,* Process Biochem. 108 (2021), pp. 60–68.

[23] H.S.E.O.H. Honarkar, J. Jin, L.C.G.R.G. Bacabac and J. Klein-Nulend, *Cellulose and its derivatives: towards biomedical applications,* Cellulose 28 (2021), pp. 1893–1931.

[24] S. Swingler, A. Gupta, H. Gibson, M. Kowalczuk, W. Heaselgrave and I. Radecka, *Recent advances and applications of bacterial cellulose in biomedicine,* Polymers (Basel). 13 (2021), pp. 412.

[25] E. Baldikova, K. Pospiskova, D. Ladakis, I.K. Kookos, A.A. Koutinas, M. Safarikova et al., *Magnetically modified bacterial cellulose: A promising carrier for immobilization of affinity ligands, enzymes, and cells,* Mater. Sci. Eng. C 71 (2017), pp. 214–221.

[26] L. Popa, M.V. Ghica, E.E. Tudoroiu, D.G. Ionescu and C.E. Dinu-Pîrvu, *Bacterial Cellulose—A Remarkable Polymer as a Source for Biomaterials Tailoring*, Materials (Basel). 15 (2022), .

[27] U. Beekmann, P. Zahel, B. Karl, L. Schmölz, F. Börner, J. Gerstmeier et al., *Modified bacterial cellulose dressings to treat inflammatory wounds*, Nanomaterials 10 (2020), pp. 2508.

[28] B. Bayón, I.R. Berti, A.M. Gagneten and G.R. Castro, *Waste to wealth*, Energy, Environ. Sustain. Springer (2018), pp. 1–44.

[29] P. Shrivastav, S. Pramanik, G. Vaidya, M.A. Abdelgawad, M.M. Ghoneim, A. Singh et al., *Bacterial cellulose as a potential biopolymer in biomedical applications: a state-of-the-art review*, J. Mater. Chem. B (2022), .

[30] M.H. Deinema and L. Zevenhuizen, *Formation of cellulose fibrils by gram-negative bacteria and their role in bacterial flocculation*, Arch. Mikrobiol. 78 (1971), pp. 42–57.

[31] J.L.W. Morgan, J. Strumillo and J. Zimmer, *Crystallographic snapshot of cellulose synthesis and membrane translocation*, Nature 493 (2013), pp. 181–186.

[32] W. Tang, S. Jia, Y. Jia and H. Yang, *The influence of fermentation conditions and post-treatment methods on porosity of bacterial cellulose membrane*, World J. Microbiol. Biotechnol. 26 (2010), pp. 125–131.

[33] F. Mohammadkazemi, M. Azin and A. Ashori, *Production of bacterial cellulose using different carbon sources and culture media*, Carbohydr. Polym. 117 (2015), pp. 518–523.

[34] S.S.A. Rahman, T. Vaishnavi, G.S. Vidyasri, K. Sathya, P. Priyanka, P. Venkatachalam et al., *Production of bacterial cellulose using Gluconacetobacter kombuchae immobilized on Luffa aegyptiaca support*, Sci. Rep. 11 (2021), pp. 1–15.

[35] I. de A.A. Fernandes, A.C. Pedro, V.R. Ribeiro, D.G. Bortolini, M.S.C. Ozaki, G.M. Maciel et al., *Bacterial cellulose: From production optimization to new applications*, Int. J. Biol. Macromol. 164 (2020), pp. 2598–2611.

[36] T. Lu, H. Gao, B. Liao, J. Wu, W. Zhang, J. Huang et al., *Characterization and optimization of production of bacterial cellulose from strain CGMCC 17276 based on whole-genome analysis*, Carbohydr. Polym. 232 (2020), pp. 115788.

[37] H. Ullah, H.A. Santos and T. Khan, *Applications of bacterial cellulose in food, cosmetics and drug delivery*, Cellulose 23 (2016), pp. 2291–2314.

[38] S. Ul, M. Ul-islam, H. Ahsan, M. Bilal, A. Shehzad, A. Fatima et al., *International Journal of Biological Macromolecules Potential applications of bacterial cellulose and its composites for cancer treatment*, Int. J. Biol. Macromol. 168 (2021), pp. 301–309.

[39] S. Akagi, H. Ando, K. Fujita, T. Shimizu, Y. Ishima, K. Tajima et al., *Therapeutic efficacy of a paclitaxel-loaded nanofibrillated bacterial cellulose (PTX/NFBC) formulation in a peritoneally disseminated gastric cancer xenograft model*, Int. J. Biol. Macromol. 174 (2021), pp. 494–501.

[40] L. Huang, X. Chen, T.X. Nguyen, H. Tang, L. Zhang and G. Yang, *Nano-cellulose 3D-networks as controlled-release drug carriers*, J. Mater. Chem. B 1 (2013), pp. 2976–2984.

[41] Q. Zhou, E. Malm, H. Nilsson, P.T. Larsson, T. Iversen, L.A. Berglund et al., *Nanostructured biocomposites based on bacterial cellulosic nanofibers compartmentalized by a soft hydroxyethylcellulose matrix coating*, Soft Matter 5 (2009), pp. 4124–4130.

[42] M. Amin, A.G. Abadi, N. Ahmad, H. Katas and J.A. Jamal, *Bacterial cellulose film coating as drug delivery system: physicochemical, thermal and drug release properties*, Sains Malaysiana 41 (2012), pp. 561–568.

[43] Z. Iskierko, P.S. Sharma, K. Bartold, A. Pietrzyk-Le, K. Noworyta and W. Kutner, *Molecularly imprinted polymers for separating and sensing of macromolecular compounds and microorganisms,* Biotechnol. Adv. 34 (2016), pp. 30–46.

[44] A. Derazshamshir, I. Göktürk, E. Tamahkar, F. Yılmaz, N. Sağlam and A. Denizli, *Phenol removal from wastewater by surface imprinted bacterial cellulose nanofibres,* Environ. Technol. (United Kingdom) 41 (2020), pp. 3134–3145.

[45] Y. Saylan, E. Tamahkar and A. Denizli, *Recognition of lysozyme using surface imprinted bacterial cellulose nanofibers*, J. Biomater. Sci. Polym. Ed. 28 (2017), pp. 1950–1965.

[46] Y. Saylan, S. Akgönüllü, H. Yavuz, S. Ünal and A. Denizli, *Molecularly imprinted polymer based sensors for medical applications,* Sensors (Switzerland) 19 (2019), .

[47] M. Arabi, A. Ostovan, J. Li, X. Wang, Z. Zhang, J. Choo et al., *Molecular Imprinting: Green Perspectives and Strategies,* Adv. Mater. 33 (2021), pp. 1–33.

[48] L. Donato, I.I. Nasser, M. Majdoub and E. Drioli, *Green Chemistry and Molecularly Imprinted Membranes*, Membranes (Basel). 12 (2022), pp. 472.

[49] S. Akgönüllü, H. Yavuz and A. Denizli, *Molecularly Imprinted Based Sensors for Detection of Allergens*, in *Molecular Imprinting for Nanosensors and Other Sensing Applications,* A. Denizli, ed., Elsevier, 2021, pp. 309–334.

[50] R. Arshad, A. Rhouati, A. Hayat, M.H. Nawaz, M.A. Yameen, A. Mujahid et al., *MIP-based impedimetric sensor for detecting dengue fever biomarker,* Appl. Biochem. Biotechnol. 191 (2020), pp. 1384–1394.

[51] M.C. Norell, H.S. Andersson and I.A. Nicholls, *Theophylline molecularly imprinted polymer dissociation kinetics: a novel sustained release drug dosage mechanism,* J. Mol. Recognit. An Interdiscip. J. 11 (1998), pp. 98–102.

[52] C. Villanueva, A. Awada, M. Campone, J.P. Machiels, T. Besse, E. Magherini et al., *A multicentre dose-escalating study of cabazitaxel (XRP6258) in combination with capecitabine in patients with metastatic breast cancer progressing after anthracycline and taxane treatment: a phase I/II study,* Eur. J. Cancer 47 (2011), pp. 1037–1045.

[53] J. Fischer and C.R. Ganellin, *Analogue-based drug discovery*, Chem. Int. IUPAC 32 (2010), pp. 12–15.

[54] E. Parhizkar, S. Mohammadi and A. Sakhteman, *Colloids and Surfaces B : Biointerfaces Synthesis , cytotoxicity assay , pharmacokinetics , biodistribution and modeling study of cabazitaxel-dextran nanoconjugates : targeted vs non targeted delivery*, Colloids Surfaces B Biointerfaces 209 (2022), pp. 112187.

[55] E. Pean, P. Demolis, A. Moreau, R.J. Hemmings, D. O’Connor, D. Brown et al., *The European Medicines Agency review of cabazitaxel (Jevtana®) for the treatment of hormone-refractory metastatic prostate cancer: summary of the scientific assessment of the committee for medicinal products for human use,*

Oncologist 17 (2012), pp. 543.

[56] S. Erdogan, R. Serttas, K. Turkekul and I. Dibirdik, *The synergistic anticancer effect of salinomycin combined with cabazitaxel in CD44 + prostate cancer cells by downregulating wnt , NF- κB and AKT signaling*, (2022), .

[57] M.M. Annapurna and B. Venkatesh, *Development and Validation of a Stability-Indicating Liquid Chromatographic Method for the Assay of Cabazitaxel*, 3 (2014), pp. 854–860.

[58] R. Chen, Q. Cheng, K.G. Owusu-Ansah, J. Chen, G. Song, H. Xie et al., *Cabazitaxel, a novel chemotherapeutic alternative for drug-resistant hepatocellular carcinoma*, Am. J. Cancer Res. 8 (2018), pp. 1297.

[59] Y.-Y. Zeng, Y.-J. Zeng, N.-N. Zhang, C.-X. Li, T. Xie and Z.-W. Zeng, *The preparation, determination of a flexible complex liposome co-loaded with cabazitaxel and β-elemene, and animal pharmacodynamics on paclitaxel-resistant lung adenocarcinoma*, Molecules 24 (2019), pp. 1697.

[60] T. Li, X. Chen, J. Wan, X. Hu, W. Chen and H. Wang, *Akt inhibition improves the efficacy of cabazitaxel nanomedicine in preclinical taxane-resistant cancer models*, Int. J. Pharm. 607 (2021), pp. 121017.

[61] J. Jin, J. Wan, X. Hu, T. Fang, Z. Ye and H. Wang, *Supramolecular nanoparticles self-assembled from reduction-responsive cabazitaxel prodrugs for effective cancer therapy*, Chem. Commun. 57 (2021), pp. 2261–2264.

[62] S. Oudard, K. Fizazi, L. Sengeløv, G. Daugaard, F. Saad, S. Hansen et al., *Cabazitaxel versus docetaxel as first-line therapy for patients with metastatic castration-resistant prostate cancer: a randomized phase III trial—FIRSTANA*, J. Clin. Oncol. 35 (2017), pp. 3189–3197.

[63] K. Kreis, D. Horenkamp-sonntag, U. Schneider, J. Zeidler, G. Glaeske and L. Weissbach, *Safety and survival of docetaxel and cabazitaxel in metastatic castration-resistant prostate cancer*, (2022), pp. 470–479.

[64] Q. Shuai, G. Zhao, X. Lian, J. Wan, B. Cen, W. Zhang et al., *Self-assembling poly (ethylene glycol)-block-polylactide-cabazitaxel conjugate nanoparticles for anticancer therapy with high efficacy and low in vivo toxicity*, Int. J. Pharm. 574 (2020), pp. 118879.

[65] X. Han, D. Chen, J. Sun, J. Zhou, D. Li and F. Gong, *A novel cabazitaxel-loaded polymeric micelle system with superior in vitro stability and long blood circulation time*, 5063 (2016), .

[66] X. Xie, Y. Zhang, F. Li, T. Lv, Z. Li, H. Chen et al., *Challenges and opportunities from basic cancer biology for nanomedicine for targeted drug delivery*, Curr. Cancer Drug Targets 19 (2019), pp. 257–276.

[67] S.K. Golombek, J.-N. May, B. Theek, L. Appold, N. Drude, F. Kiessling et al., *Tumor targeting via EPR: Strategies to enhance patient responses*, Adv. Drug Deliv. Rev. 130 (2018), pp. 17–38.

[68] N. Hasan, L. Rahman, S.H. Kim, J. Cao, A. Arjuna, S. Lallo et al., *Recent advances of nanocellulose in drug delivery systems*, J. Pharm. Investig. 50 (2020), pp. 553–572.

[69] L.R. Lynd, P.J. Weimer, W.H. Van Zyl and I.S. Pretorius, *Microbial cellulose utilization: fundamentals and biotechnology*, Microbiol. Mol. Biol. Rev. 66 (2002), pp. 506–577.

[70] R.A.C. Dos Santos, A.A. Berretta, H. da S. Barud, S.J.L. Ribeiro, L.N. González-García, T.D. Zucchi et al., *Draft genome sequence of Komagataeibacter rhaeticus strain AF1, a high producer of cellulose, isolated from Kombucha tea*, Genome Announc. 2 (2014), pp. e00731-14.

[71] A.J. Brown, *XLIII.—On an acetic ferment which forms cellulose*, J. Chem. Soc. Trans. 49 (1886), pp. 432–439.

[72] M. Ul-Islam, *Comparative synthesis and characterization of bio-cellulose from local waste and cheap resources*, Curr. Pharm. Des. 25 (2019), pp. 3664–3671.

[73] M. Ul-Islam, S. Khan, M.W. Ullah and J.K. Park, *Comparative study of plant and bacterial cellulose pellicles regenerated from dissolved states*, Int. J. Biol. Macromol. 137 (2019), pp. 247–252.

[74] D. Klemm, F. Kramer, S. Moritz, T. Lindström, M. Ankerfors, D. Gray et al., *Nanocelluloses: a new family of nature-based materials*, Angew. Chemie Int. Ed. 50 (2011), pp. 5438–5466.

[75] F. Barja, *Bacterial nanocellulose production and biomedical applications*, J. Biomed. Res. 35 (2021), pp. 310.

[76] A.A.B. Omran, A.A.B.A. Mohammed, S.M. Sapuan, R.A. Ilyas, M.R.M. Asyraf, S.S. Rahimian Koloor et al., *Micro-and nanocellulose in polymer composite materials: A review*, Polymers (Basel). 13 (2021), pp. 231.

[77] H. Abral, M.K. Chairani, M.D. Rizki, M. Mahardika, D. Handayani, E. Sugiarti et al., *Characterization of compressed bacterial cellulose nanopaper film after exposure to dry and humid conditions*, J. Mater. Res. Technol. 11 (2021), pp. 896–904.

[78] J. Wang, J. Tavakoli and Y. Tang, *Bacterial cellulose production, properties and applications with different culture methods–A review*, Carbohydr. Polym. 219 (2019), pp. 63–76.

[79] M.U. Islam, M.W. Ullah, S. Khan, N. Shah and J.K. Park, *Strategies for cost-effective and enhanced production of bacterial cellulose*, Int. J. Biol. Macromol. 102 (2017), pp. 1166–1173.

[80] A. Colburn, R.J. Vogler, A. Patel, M. Bezold, J. Craven, C. Liu et al., *Composite membranes derived from cellulose and lignin sulfonate for selective separations and antifouling aspects*, Nanomaterials 9 (2019), pp. 867.

[81] S. Iftekhar, V. Srivastava and M. Sillanpää, *Synthesis and application of LDH intercalated cellulose nanocomposite for separation of rare earth elements (REEs)*, Chem. Eng. J. 309 (2017), pp. 130–139.

[82] M. de Lima Fontes, A.B. Meneguin, A. Tercjak, J. Gutierrez, B.S.F. Cury, A.M. Dos Santos et al., *Effect of in situ modification of bacterial cellulose with carboxymethylcellulose on its nano/microstructure and methotrexate release properties*, Carbohydr. Polym. 179 (2018), pp. 126–134.

[83] S. Gorgieva, *Bacterial cellulose as a versatile platform for research and development of biomedical materials*, Processes 8 (2020), pp. 624.

[84] G. Xiong, H. Luo, Y. Zhu, S. Raman and Y. Wan, *Creation of macropores in three-dimensional bacterial cellulose scaffold for potential cancer cell culture*, Carbohydr. Polym. 114 (2014), pp. 553–557.

[85] A.-M. Gavrilă, E.-B. Stoica, T.-V. Iordache and A. Sârbu, *Modern and Dedicated Methods for Producing Molecularly Imprinted Polymer Layers in Sensing Applications*, Appl. Sci. 12 (2022), pp. 3080.

[86] R. Kubota, Y. Sasaki, T. Minamiki and T. Minami, *Chemical sensing platforms based on organic thin-film transistors functionalized with artificial receptors*, ACS sensors 4 (2019), pp. 2571–2587.

[87] F. Cui, Z. Zhou and H.S. Zhou, *Molecularly imprinted polymers and surface imprinted polymers based electrochemical biosensor for infectious diseases*, Sensors (Switzerland) 20 (2020), .

[88] S. Akgönüllü, H. Yavuz and A. Denizli, *SPR nanosensor based on molecularly imprinted polymer film with gold nanoparticles for sensitive detection of aflatoxin B1*, Talanta 219 (2020), pp. 121219.

[89] S. Akgönüllü, E. Özgür and A. Denizli, *Recent Advances in Quartz Crystal Microbalance Biosensors Based on the Molecular Imprinting Technique for Disease-Related Biomarkers*, Chemosensors 10 (2022), .

[90] M. V Polyakov, *Adsorption properties and structure of silica gel*, Zhur Fiz Khim 2 (1931), pp. 799–805.

[91] G. Wulff, *The use of polymers with enzyme-analogous structures for the resolution of racemates*, Angrew. Chem. Internat. Ed. 11 (1972), pp. 341.

[92] R. Arshady and K. Mosbach, *Synthesis of substrate-selective polymers by host-guest polymerization*, Die Makromol. Chemie Macromol. Chem. Phys. 182 (1981), pp. 687–692.

[93] *Molecularly imprinted polymers: Present and future prospective*. 2011.

[94] L. Uzun and A.P.F. Turner, *Molecularly-imprinted polymer sensors: Realising their potential*, Biosens. Bioelectron. 76 (2016), pp. 131–144.

[95] S.A. Zaidi, *Latest trends in molecular imprinted polymer based drug delivery systems*, RSC Adv. 6 (2016), pp. 88807–88819.

[96] J.R. Choi, K.W. Yong, J.Y. Choi and A.C. Cowie, *Progress in Molecularly Imprinted Polymers for Biomedical Applications*, Comb. Chem. High Throughput Screen. 22 (2019), pp. 78–88.

[97] F. Puoci, F. Iemma and N. Picci, *Stimuli-Responsive Molecularly Imprinted Polymers for Drug Delivery: A Review*, Curr. Drug Deliv. 5 (2008), pp. 85–96.

[98] J. Kupai, M. Razali, S. Buyuktiryaki, R. Kecili and G. Szekely, *Long-term stability and reusability of molecularly imprinted polymers*, Polym. Chem. 8 (2017), pp. 666–673.

[99] J. Svenson and I.A. Nicholls, *On the thermal and chemical stability of molecularly*

imprinted polymers, Anal. Chim. Acta 435 (2001), pp. 19–24.

[100] E.N. Ndunda, *Molecularly imprinted polymers—A closer look at the control polymer used in determining the imprinting effect: A mini review*, J. Mol. Recognit. 33 (2020), pp. e2855.

[101] G. Wulff, *Molecular Imprinting in Cross-Linked Materials with the Aid of Molecular Templates— A Way towards Artificial Antibodies*, Angew. Chemie Int. Ed. English 34 (1995), pp. 1812–1832.

[102] S. Wang, J. Ye, Z. Bie and Z. Liu, *Affinity-tunable specific recognition of glycoproteins via boronate affinity-based controllable oriented surface imprinting*, Chem. Sci. 5 (2014), pp. 1135–1140.

[103] F. Shen and X. Ren, *Covalent molecular imprinting made easy: a case study of mannose imprinted polymer*, RSC Adv. 4 (2014), pp. 13123–13125.

[104] L. Andersson, B. Sellergren and K. Mosbach, *Imprinting of amino acid derivatives in macroporous polymers*, Tetrahedron Lett. 25 (1984), pp. 5211–5214.

[105] A.N. Barclay, Membrane proteins with immunoglobulin-like domains—a master superfamily of interaction molecules, in Seminars in immunology, 15 (2003), pp. 215–223.

[106] L. Chen, S. Xu and J. Li, *Recent advances in molecular imprinting technology: Current status, challenges and highlighted applications*, Chem. Soc. Rev. 40 (2011), pp. 2922–2942.

[107] M.S. da Silva, R. Viveiros, A. Aguiar-Ricardo, V.D.B. Bonifácio and T. Casimiro, *Supercritical fluid technology as a new strategy for the development of semi-covalent molecularly imprinted materials*, Rsc Adv. 2 (2012), pp. 5075–5079.

[108] M.J. Whitcombe, M.E. Rodriguez, P. Villar and E.N. Vulfson, *A new method for the introduction of recognition site functionality into polymers prepared by molecular imprinting: synthesis and characterization of polymeric receptors for cholesterol*, J. Am. Chem. Soc. 117 (1995), pp. 7105–7111.

[109] P. Curcio, C. Zandanel, A. Wagner, C. Mioskowski and R. Baati, *Semi-Covalent Surface Molecular Imprinting of Polymers by One-Stage Mini-emulsion Polymerization: Glucopyranoside as a Model Analyte*, Macromol. Biosci. 9 (2009), pp. 596–604.

[110] J. Ashley, M.-A. Shahbazi, K. Kant, V.A. Chidambara, A. Wolff, D.D. Bang et al., *Molecularly imprinted polymers for sample preparation and biosensing in food analysis: Progress and perspectives*, Biosens. Bioelectron. 91 (2017), pp. 606–615.

[111] S. Ansari, *Combination of molecularly imprinted polymers and carbon nanomaterials as a versatile biosensing tool in sample analysis: Recent applications and challenges*, TrAC - Trends Anal. Chem. 93 (2017), pp. 134–151.

[112] L. Xu, Y.-A. Huang, Q.-J. Zhu and C. Ye, *Chitosan in molecularly-imprinted polymers: Current and future prospects*, Int. J. Mol. Sci. 16 (2015), pp. 18328–18347.

[113] H. Nishide and E. Tsuchida, *Selective adsorption of metal ions on poly (4-*

vinylpyridine) resins in which the ligand chain is immobilized by crosslinking, Die Makromol. Chemie Macromol. Chem. Phys. 177 (1976), pp. 2295–2310.

[114] C. Alexander, H.S. Andersson, L.I. Andersson, R.J. Ansell, N. Kirsch, I.A. Nicholls et al., *Molecular imprinting science and technology: a survey of the literature for the years up to and including 2003,* J. Mol. Recognit. An Interdiscip. J. 19 (2006), pp. 106–180.

[115] Z. Li, H. Tian, Y. Yuan, X. Yin, X. Wei, L. Tang et al., *Metal-ion-imprinted thermo-responsive materials obtained from bacterial cellulose: synthesis, characterization, and adsorption evaluation*, J. Mater. Chem. A 7 (2019), pp. 11742–11755.

[116] G. Sharma and B. Kandasubramanian, *Molecularly imprinted polymers for selective recognition and extraction of heavy metal ions and toxic dyes*, J. Chem. Eng. Data 65 (2020), pp. 396–418.

[117] O.I. Parisi and F. Puoci, *Stimuli-responsive Molecularly Imprinted Polymers*, in *Chemoresponsive Materials*, 2015, pp. 364–383.

[118] L. Chen, X. Wang, W. Lu, X. Wua and J. Lia, *Molecular imprinting: perspectives and applications*, Chem. Soc. Rev. 45 (2016), pp. 2137–2211.

[119] N. Yuksel and S. Tektas, *Molecularly imprinted polymers: preparation, characterisation, and application in drug delivery systems*, J. Microencapsul. 0 (2022), pp. 1–21.

[120] A. Lusina and M. Cegłowski, *Molecularly Imprinted Polymers as State-of-the-Art Drug Carriers in Hydrogel Transdermal Drug Delivery Applications*, Polymers (Basel). 14 (2022), .

[121] P.K. Paul, A. Treetong and R. Suedee, *Biomimetic insulin-imprinted polymer nanoparticles as a potential oral drug delivery system*, Acta Pharm. 67 (2017), pp. 149–168.

[122] E. Asadi, M. Abdouss, R.M. Leblanc, N. Ezzati, J.N. Wilson and S. Azodi-Deilami, *In vitro / in vivo study of novel anti-cancer, biodegradable cross-linked tannic acid for fabrication of 5-fluorouracil-targeting drug delivery nano-device based on a molecular imprinted polymer*, RSC Adv. 6 (2016), pp. 37308–37318.

[123] S. He, L. Zhang, S. Bai, H. Yang, Z. Cui, X. Zhang et al., *Advances of molecularly imprinted polymers (MIP) and the application in drug delivery*, Eur. Polym. J. 143 (2021), pp. 110179.

[124] N.M. Bergmann and N.A. Peppas, *Molecularly imprinted polymers with specific recognition for macromolecules and proteins*, Prog. Polym. Sci. 33 (2008), pp. 271–288.

[125] M. Moreno-Bondi, F. Navarro-Villoslada, E. Benito-Pena and J. Urraca, *Molecularly Imprinted Polymers as Selective Recognition Elements in Optical Sensing*, Curr. Anal. Chem. 4 (2008), pp. 316–340.

[126] H. Kempe and M. Kempe, *Molecularly Imprinted Polymers*, Wiley-VCH: Weinheim, 2009.

[127] R. Schirhagl, *Bioapplications for molecularly imprinted polymers*, Anal. Chem. 86

(2014), pp. 250–261.

[128] A. Adumitrăchioaie, M. Tertiș, A. Cernat, R. Săndulescu and C. Cristea, *Electrochemical methods based on molecularly imprinted polymers for drug detection. A review*, Int. J. Electrochem. Sci 13 (2018), pp. 2556–2576.

[129] M. Guć and G. Schroeder, *The Molecularly Imprinted Polymers. Influence of Monomers on The Properties of Polymers*, World J. Res. Rev. 5 (2017), pp. 36–47.

[130] M.P. Pešić, M.D. Todorov, G. Becskereki, G. Horvai, T. Verbić and B. Tóth, *A novel method of molecular imprinting applied to the template cholesterol*, Talanta 217 (2020), pp. 121075.

[131] K.K. Markose, R. Anjana and M.K. Jayaraj, *Upconversion Nanophosphors: An Overview*, Nanostructured Met. Oxides Devices (2020), pp. 47–102.

[132] Y. Zhang, S. Li, X.-T. Ma, X.-W. He, W.-Y. Li and Y.-K. Zhang, *Carbon dots-embedded epitope imprinted polymer for targeted fluorescence imaging of cervical cancer via recognition of epidermal growth factor receptor*, Microchim. Acta 187 (2020), pp. 1–11.

[133] K. Haupt, P.X. Medina Rangel and B.T.S. Bui, *Molecularly imprinted polymers: Antibody mimics for bioimaging and therapy*, Chem. Rev. 120 (2020), pp. 9554–9582.

[134] I. Veloz Martínez, J.I. Ek, E.C. Ahn and A.O. Sustaita, *Molecularly imprinted polymers via reversible addition–fragmentation chain-transfer synthesis in sensing and environmental applications* , RSC Adv. 12 (2022), pp. 9186–9201.

[135] G. Ertürk and B. Mattiasson, *Molecular imprinting techniques used for the preparation of biosensors*, Sensors (Switzerland) 17 (2017), pp. 1–17.

[136] M.G. Metwally, A.H. Benhawy, R.M. Khalifa, R.M. El Nashar and M. Trojanowicz, *Application of molecularly imprinted polymers in the analysis of waters and wastewaters*, Molecules 26 (2021), .

[137] A. Martín-Esteban, *Green molecularly imprinted polymers for sustainable sample preparation*, J. Sep. Sci. 45 (2022), pp. 233–245.

[138] V. Ratautaite, U. Samukaite-Bubniene, D. Plausinaitis, R. Boguzaite, D. Balciunas, A. Ramanaviciene et al., *Molecular imprinting technology for determination of uric acid*, Int. J. Mol. Sci. 22 (2021), pp. 1–18.

[139] S. Boulanouar, S. Mezzache, A. Combès and V. Pichon, *Molecularly imprinted polymers for the determination of organophosphorus pesticides in complex samples*, Talanta 176 (2018), pp. 465–478.

[140] S. K and B. P, *Formulation and In-Vitro Evaluation of Liposomal Drug Delivery System of Cabazitaxel*, J. Pharm. Drug Deliv. Res. 04 (2015), .

[141] N.H. Avcioglu, C. Sevim, E.N. Alver, S. Donmez and I.S. Bilkay, *Comparison of Bacterial Cellulose Production By K[1] N.H. Avcioglu, C. Sevim, E.N. Alver, S. Donmez, I.S. Bilkay, Comparison of Bacterial Cellulose Production By Komagataeibacter Intermedius Strain Using Lavandula Angustifolia, Rosa Canina and Tilia Corda*, Cellul. Chem. Technol. 55 (2021), pp. 1029–1041.

[142] E.P. Çoban and H. Biyik, *Effect of various carbon and nitrogen sources on cellulose synthesis by Acetobacter lovaniensis HBB5*, African J. Biotechnol. 10 (2011), pp. 5346–5354.

[143] C. Bodhibukkana, T. Srichana, S. Kaewnopparat, N. Tangthong, P. Bouking, G.P. Martin et al., *Composite membrane of bacterially-derived cellulose and molecularly imprinted polymer for use as a transdermal enantioselective controlled-release system of racemic propranolol*, J. Control. release 113 (2006), pp. 43–56.

[144] Z.X. Meng, X.X. Xu, W. Zheng, H.M. Zhou, L. Li, Y.F. Zheng et al., *Preparation and characterization of electrospun PLGA/gelatin nanofibers as a potential drug delivery system*, Colloids Surfaces B Biointerfaces 84 (2011), pp. 97–102.

[145] S. Pirsa and S. Chavoshizadeh, *Design of an optical sensor for ethylene based on nanofiber bacterial cellulose film and its application for determination of banana storage time*, Polym. Adv. Technol. 29 (2018), pp. 1385–1393.

[146] N. Phruksaphithak, C. Kaewnun and O. Sompong, *Bacterial cellulose production and applications*, Sci. Eng. Heal. Stud. (2019), pp. 1–7.

[147] S.A. Villarreal-Soto, S. Beaufort, J. Bouajila, J.-P. Souchard, T. Renard, S. Rollan et al., *Impact of fermentation conditions on the production of bioactive compounds with anticancer, anti-inflammatory and antioxidant properties in kombucha tea extracts*, Process Biochem. 83 (2019), pp. 44–54.

[148] E.A. Hassan, H.M. Abdelhady, S.S.A. El-Salam and S.M. Abdullah, *The characterization of bacterial cellulose produced by Acetobacter xylinum and Komgataeibacter saccharovorans under optimized fermentation conditions*, Br. Microbiol. Res. J. 9 (2015), pp. 1–13.

[149] S.-P. Lin, Y.-H. Huang, K.-D. Hsu, Y.-J. Lai, Y.-K. Chen and K.-C. Cheng, *Isolation and identification of cellulose-producing strain Komagataeibacter intermedius from fermented fruit juice*, Carbohydr. Polym. 151 (2016), pp. 827–833.

[150] H. Khan, V. Saroha, S. Raghuvanshi, A.K. Bharti and D. Dutt, *Valorization of fruit processing waste to produce high value-added bacterial nanocellulose by a novel strain Komagataeibacter xylinus IITR DKH20*, Carbohydr. Polym. 260 (2021), pp. 117807.

[151] Z. Yan, S. Chen, H. Wang, B. Wang and J. Jiang, *Biosynthesis of bacterial cellulose/multi-walled carbon nanotubes in agitated culture*, Carbohydr. Polym. 74 (2008), pp. 659–665.

[152] H.G. de Oliveira Barud, R.R. da Silva, H. da Silva Barud, A. Tercjak, J. Gutierrez, W.R. Lustri et al., *A multipurpose natural and renewable polymer in medical applications: Bacterial cellulose*, Carbohydr. Polym. 153 (2016), pp. 406–420.

[153] R. Du, F. Zhao, Q. Peng, Z. Zhou and Y. Han, *Production and characterization of bacterial cellulose produced by Gluconacetobacter xylinus isolated from Chinese persimmon vinegar*, Carbohydr. Polym. 194 (2018), pp. 200–207.

[154] G. Pacheco, C.R. Nogueira, A.B. Meneguin, E. Trovatti, M.C.C. Silva, R.T.A. Machado et al., *Development and characterization of bacterial cellulose produced*

by cashew tree residues as alternative carbon source, Ind. Crops Prod. 107 (2017), pp. 13–19.

[155] F.K. Andrade, J.P.S. Morais, C.R. Muniz, J.H.O. Nascimento, R.S. Vieira, F.M.P. Gama et al., *Stable microfluidized bacterial cellulose suspension*, Cellulose 26 (2019), pp. 5851–5864.

[156] N. Tyagi and S. Suresh, *Production of cellulose from sugarcane molasses using Gluconacetobacter intermedius SNT-1: optimization & characterization*, J. Clean. Prod. 112 (2016), pp. 71–80.

[157] J. Ye, S. Zheng, Z. Zhang, F. Yang, K. Ma, Y. Feng et al., *Bacterial cellulose production by Acetobacter xylinum ATCC 23767 using tobacco waste extract as culture medium*, Bioresour. Technol. 274 (2019), pp. 518–524.

[158] X. Wang, H. Mao, W. Huang, W. Guan, X. Zou, J. Pan et al., *Preparation of magnetic imprinted polymer particles via microwave heating initiated polymerization for selective enrichment of 2-amino-4-nitrophenol from aqueous solution*, Chem. Eng. J. 178 (2011), pp. 85–92.

[159] Y.H. Tsai, Y.N. Yang, Y.C. Ho, M.L. Tsai and F.L. Mi, *Drug release and antioxidant/antibacterial activities of silymarin-zein nanoparticle/bacterial cellulose nanofiber composite films*, Carbohydr. Polym. 180 (2018), pp. 286–296.

[160] S.-O. Dima, D.-M. Panaitescu, C. Orban, M. Ghiurea, S.-M. Doncea, R.C. Fierascu et al., *Bacterial nanocellulose from side-streams of kombucha beverages production: Preparation and physical-chemical properties*, Polymers (Basel). 9 (2017), pp. 374.

[161] T. Musumeci, C.A. Ventura, I. Giannone, B. Ruozi, L. Montenegro, R. Pignatello et al., *PLA/PLGA nanoparticles for sustained release of docetaxel*, Int. J. Pharm. 325 (2006), pp. 172–179.

[162] J.D. Clogston and A.K. Patri, *Zeta potential measurement*, in *Characterization of nanoparticles intended for drug delivery*, Springer, 2011, pp. 63–70.

[163] J. Yan, Y. Wang, Y. Jia, S. Liu, C. Tian, W. Pan et al., *Co-delivery of docetaxel and curcumin prodrug via dual-targeted nanoparticles with synergistic antitumor activity against prostate cancer*, Biomed. Pharmacother. 88 (2017), pp. 374–383.

[164] M. Li, S. Feng, H. Xing and Y. Sun, *Dexmedetomidine and levobupivacaine co-loaded, transcriptional transactivator peptide modified nanostructured lipid carriers or lipid–polymer hybrid nanoparticles, which performed better for local anesthetic therapy?*, Drug Deliv. 27 (2020), pp. 1452–1460.

[165] W. Shao, H. Liu, X. Liu, S. Wang and R. Zhang, *Anti-bacterial performances and biocompatibility of bacterial cellulose/graphene oxide composites*, RSC Adv. 5 (2015), pp. 4795–4803.

[166] A.J.D. Silvestre, C.S.R. Freire and C.P. Neto, *Do bacterial cellulose membranes have potential in drug-delivery systems?*, Expert Opin. Drug Deliv. 11 (2014), pp. 1113–1124.